SURFACE MODIFICATION OF
ADDITIVELY MANUFACTURED METALLIC COMPONENTS

Surface Modification of Additively Manufactured Metallic Components

By

Sameh Mekhiel, B.Sc., M.Sc.

A Thesis

Submitted to the School of Graduate Studies in Partial Fulfillment of the Requirements

for the Degree Doctor of Philosophy

McMaster University

DOCTOR OF PHILOSOPHY (2021) McMaster University

(Mechanical Engineering) Hamilton, Ontario

TITLE: Surface Modification of

Additively Manufactured Metallic Components

AUTHOR: Sameh Mekhiel

B.Sc. in Aircraft Mechanical Engineering

(Military Technical College in Cairo)

M.Sc. in Mechanical Engineering

(Military Technical College in Cairo)

SUPERVISORS: Dr. M. A. Elbestawi

Dr. Philip Koshy

NUMBER OF PAGES: 143

Preface

This manuscript is an integrated article thesis of **Sameh Mekhiel**, the sole author, known as a sandwich thesis. The author uses **Sameh Mekhiel** as his formal name in publications. The manuscript consists of five chapters and presents the experimental and analytical work performed by the author at McMaster University from 2018 to 2021. The author received his B.Sc. in Aircraft Mechanical Engineering from the Military Technical College, Cairo, Egypt, in 2009. He obtained his M.Sc. from the same college in 2017.

The thesis contributes to the surface modification of additively manufactured metallic components to improve their functionality and expand their application envelope. It is a compilation of three academic papers` manuscripts written following the School of Graduate Studies regulation at McMaster University. The sole author has done all experimental procedures and analyses. Advice, guidance, and revisions have been provided by the academic supervisors, **Dr Philip Koshy** and **Dr M. A. Elbestawi**.

Chapter 1 provides an introduction, motivation, and research objectives; Chapters 2 is reprinted from a published journal paper, 3-4 are papers` manuscripts ready for submission, and Chapter 5 presents conclusions and closing remarks.

I *declare* that this thesis has been composed solely by myself and that no part of this thesis has been submitted for a higher degree at any other institution.

Sameh Mekhiel

September 2021

Abstract

Additive Manufacturing (AM) has revolutionized manufacturing processes by enabling the realization of custom products with intricate geometric features that were either too complex or even intractable for subtractive manufacturing processes. Yet, functional surfaces generated in AM have to be often finish machined because of their relatively inferior roughness. The first phase of this research worked around this limitation by tailoring the topography of an AM surface in-process to entail textures that further enhance certain functionalities in a process called Additive Texturing (AT).

In this context, the Selective Laser Melting (SLM) process ability to realize intricate surface microfeatures was explored experimentally, evaluating its geometrical limitations. Utilizing such limitations, various patterns comprising pillars, channels, and re-entrant structures were printed to control the wetting behaviour of SLM stainless steel. AT's efficacy is demonstrated in its capability to generate hydrophobic AM surfaces with water contact angles exceeding 140°. Similarly, other texturing patterns comprising dimples, linear, V-shaped, and X-shaped grooves were investigated to tailor the tribological response of textured surfaces under dry sliding conditions. Evidently, a specific wear rate and coefficient of friction reduction of 80% and 60%, respectively, demonstrated another potential for AT.

The undesirable tensile Residual Stresses (RS) that inevitably accumulate during the SLM process's rapid heating and cooling cycles were investigated in the second phase of this research. Laser Peening (LP) was utilized to post-process the printed samples to eliminate the initial tensile RS and induce near 500 Mpa compressive RS. Moreover, the LP parameters were explored and optimized to enhance RS, surface roughness, hardness, and wear resistance.

Acknowledgements

No words can express the amount of gratitude and respect that I have for both of my exceptional academic supervisors, **Dr Elbestawi** and **Dr Koshy**, for their continuous support and guidance. I would like to thank them for being always available to answer, guide, encourage, and inspire throughout this critical time. It is a great honour and privilege to get to know and look up to such extraordinary personalities like yours. Also, I would like to thank all of my **colleagues** and **friends,** especially **Ashmawy**, **Balbaa**, **Philip**, and **Kamel,** for their encouragement and support along the journey.

To my parents, **Mamdouh** and **Fayza**, thank you for shaping me into the person that I am today. Your calls, prayers, patience, and blessed wishes motivated me and gave me purpose and hope even in the darkest times. To my wife **Simona**, thank you for being responsible, patient, independent, and supportive. Without you by my side, it is impossible to achieve anything in life. Lastly, thanks to my children **Daniella** and **Daniel** for bringing all that joy and happiness to my life.

Above all, I praise and thank **God almighty** for his grace and blessings every step of the way.

Table of Contents

List of Figures

List of Tables

List of Abbreviations

ADSA	Axisymmetric Drop Shape Analysis
AISI	American Iron and Steel Institute
AM	Additive Manufacturing
ANOVA	Analysis of Variance
ASTM	American Society for Testing and Material
AT	Additive Texturing
CA	Contact Angle
CoF	Coefficient of Friction
CP	Conventionally Processed
DED	Directed Energy Deposition
DOE	Design of experiment
EB	Electron Beam
EB-PBF	Electron Beam- Powder Bed Fusion
EDM	Electrical Discharge Machining
GPS	Geometrical Product Specifications
HDM	Hole Drilling Method
HIP	Hot Isostatic Pressing
HV	Vickers Pyramid Number
LP	Laser Peening
L-PBF	Laser- Powder Bed Fusion
PBF	Powder Bed Fusion
PSD	Particle Size Distribution

RS	Residual Stresses
SBF	Simulated Body Fluid
SLM	Selective Laser Melting
SP	Shot Peening
SS	Stainless Steel
UNSM	Ultrasonic Nanocrystal Surface Modification
WC	Tungsten Carbide
WEDM	Wire-cut Electrical Discharge Machining
XRD	X-Ray Diffraction

List of Nomenclature

Θ	contact angle [°]
Θ_{CB}	static contact angle [°]
Θ_{W}	rough surface [°]
ρ_{bulk}	bulk density [kg/m^3]
ρ_{fl}	fluid density [kg/m^3]
σ	standard deviation
c	pillar spacing [µm]
E_{L}	linear energy densities [J/mm]
E_{v}	volumetric energy density [J/mm^3]
h	hatch spacing [mm]
$\mathrm{m}_{\mathrm{air}}$	air mass [kg]
$\mathrm{m}_{\mathrm{fluid}}$	fluid mass [kg]
P	laser power [W]
p	pillar side length [µm]
R	water drop radius [mm]
R^2	root mean square
R_a	Arithmatic Surface Roughness [µm]
r	roughness factor
t	layer thickness [µm]
v	scanning speed [mm/s]

w	track width [mm]

Chapter 1

Introduction and background

1.1 Introduction

Additive Manufacturing (AM) technologies have emerged to occupy a valuable role in the modern realm of advanced manufacturing. AM's unprecedented freedom of design has revolutionized the design concept from design for manufacturability to functionality-targeted design. Also, AM technologies have proven to be even more cost-efficient in many cases associated with complex geometries or highly customizable products. The process–structure–property paradigm has been the focus of most AM research and development literature. Such intensified research improved AM rapidly yet, some challenges are not yet appropriately explored. The present work will focus on two challenges: low surface quality and tensile Residual Stresses (RS).

The first phase of this research has worked around the surface roughness problem by introducing the novel concept of Additive Texturing (AT). Instead of improving the surface quality of the printed components, AT has created, in-process, patterns of tailored micro-features to enhance targeted functionalities.

Initially, the Selective Laser Melting (SLM) process limitation to realizing fine features has been investigated. Then, utilizing these limitations, various patterns have been designed and printed to decrease the textured surface wetting and enhance its tribological response.

Due to the thermal nature of the SLM process of repetitive cycles of rapid heating and cooling, SLMed metallic parts have gravitated to have undesirable tensile RS. The second phase of this research has explored Laser Peening (LP) as a solution for the tensile RS challenge. The efficacy of LP has gone beyond addressing such challenges to induce higher values of desirable compressive RS, implying higher fatigue resistance and part service life. In this section, a brief background has been presented on the different topics discussed going forward.

1.2 Additive manufacturing

The process in which the components are built bottom-up by compiling predefined progressive thin layers of the material is known as rapid prototyping or three dimensional (3D) printing, and the formalized term for it is AM [1]. AM is considered a revolutionary supplement to conventional subtractive manufacturing techniques. It evolves the design concept from design for machinability to design for functionality, as it eliminates tooling geometry and path constraints. This unique ability to create complicated products also results in minimizing the number of parts. Consequently, the time and cost associated with the machine set up, tooling, and assembly are diminished [1].

Additionally, the necessity of AM escalates with customizable, high-value components manufacturing. Customized components are widely used in the general engineering sector in the medical, aerospace, and tooling industries. One example of such components is the biomedical orthopaedic implant that requires customization for each patient.

Among the various AM techniques developed for metallic materials, two main groups: Directed Energy Deposition (DED) and Powder Bed Fusion (PBF), are the most commonly investigated [2]. The DED's main advantage is the high relative speed of the process and the ability to fabricate larger components. While the PBF suffers from volume limitations, it offers superior quality and more capacity to manufacture intricate features. The heat source significantly impacts such abilities; the PBF uses different heat sources like Laser (L) and Electron Beam (EB). This research focuses only on PBF-L, also known as selective laser melting (SLM) because it offers the best resolution for AM metallic materials.

In the SLM process, a thin layer of powder, in order of tens of microns in thickness, is spread on a levelled metallic base plate by a ceramic or brush recoater. Then, the laser beam scans a predefined geometry, selectively consolidating the powder layer. The predefined geometry of each layer is obtained from slicing the 3D model of the desired part geometry. Next, a new powder layer is spread, and the process is repeated layer after layer until the entire part is printed. A simplified schematic of the SLM is demonstrated in Fig. 1.1.

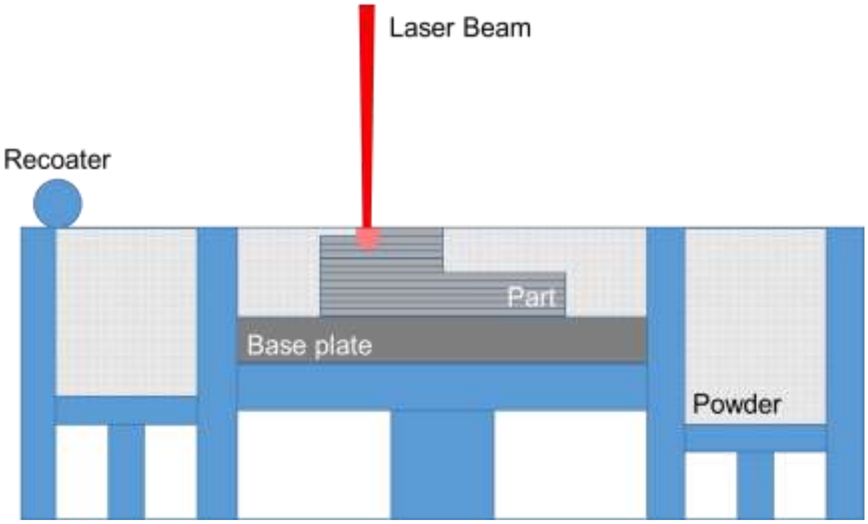

Fig. 1.1. Schematic of the SLM process.

AM components characterization is the foremost objective for most AM research studies. Relative density and microstructure of parts are the most commonly studied structure-property. Numerous efforts relate these structures with mechanical properties of tested parts such as strength, microhardness, residual stresses, etc. Moreover, structures and mechanical properties are assessed to select process parameters. The process–structure–property paradigm is considered the core of AM studies [3]. This approach of product evaluation is constructive, yet it highlighted some challenges such as low surface quality and undesirable tensile RS compromising the functionality of the AM components. In the next section, the two challenges above will be discussed briefly.

1.2.1 Surface quality

Despite the noticeable progress in material flexibility and mechanical properties in SLMed parts, relatively poor surface quality presents a major unsolved challenge. Many factors attribute to inferior surface quality, such as powder rheological properties, particle size, and morphology. Also, SLM process parameters like laser power, scanning speed, hatch spacing, and layer thickness contribute to the resulting surface quality. Moreover, parameters including part and process design conditions, feature geometry, part orientation within the build volume, support structures, overhang angles, and scan strategy impact the surface condition [2].

Surface defects such as porosity, lack of fusion, cracking or delamination are other forms of substandard surface quality. Therefore, post-processing conditions include support removal, machining polishing, peening, tumbling, and chemical treatments are imperative to acquire functional AM surfaces. However, two main mechanisms are resulting in high surface roughness; staircase effect merely due to layer thickness [4], build orientation [5], and the second mechanism for forming rough surfaces is improper melting of powder particles and balling phenomenon [6-8]. In addition, at high laser scanning speeds, the molten pool becomes elongated, which can break into small islands due to the Raleigh instability [9, 10].

1.2.1.1 Parameters affecting AM surface quality

- *Powder*

Different parameters are reported to impact the surface quality on both the top and side surfaces of AM parts. For instance, various Particle Size Distribution (PSD) has exhibited a noticeable impact on top and side surface roughness for AM AISI 316L stainless steel [11]. In addition, other powder properties like flowability, morphology, and reusability have proven crucial for controlling the output roughness.

- *Process parameters*

SLM process parameters such as power, scan speed, and hatch spacing directly impact output surface roughness. Also, the variation of output surface roughness can be correlated to a more general term like the volumetric energy density (E_v), which can be calculated as follows:

$$E_v = \frac{P}{v \times h \times t}$$

P, v, h, and t are laser power, scanning speed, hatch spacing, and layer thickness, respectively. For Al alloys, the impact of these parameters on surface roughness and dimensional tolerance was explored [12]. The results are shown individually then combined, producing a process map for optimum processing parameters regarding surface roughness (Fig. 1.2).

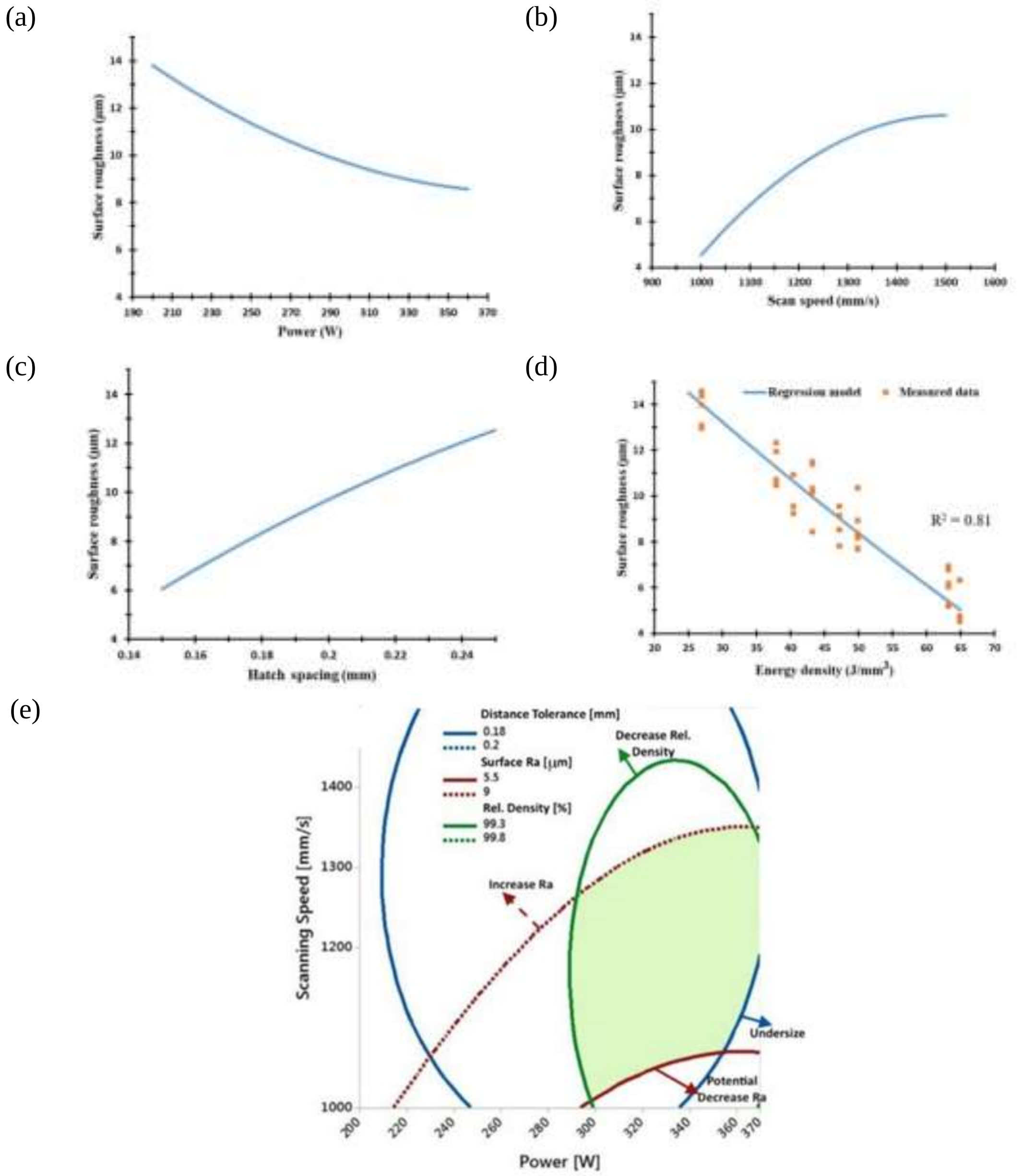

Fig. 1.2. Relation between surface roughness and (a) laser power (b) scanning speed (c) hatch spacing (d) volumetric energy density, and (e) optimum process window [12].

- *Layer thickness*

The layer thickness directly affects the effective laser beam energy absorbed by the powder during exposure. Fig. 1.3 shows the deterioration of the surface quality of SLMed Ti64 with increasing layer thickness from 20 to 100 µm [4].

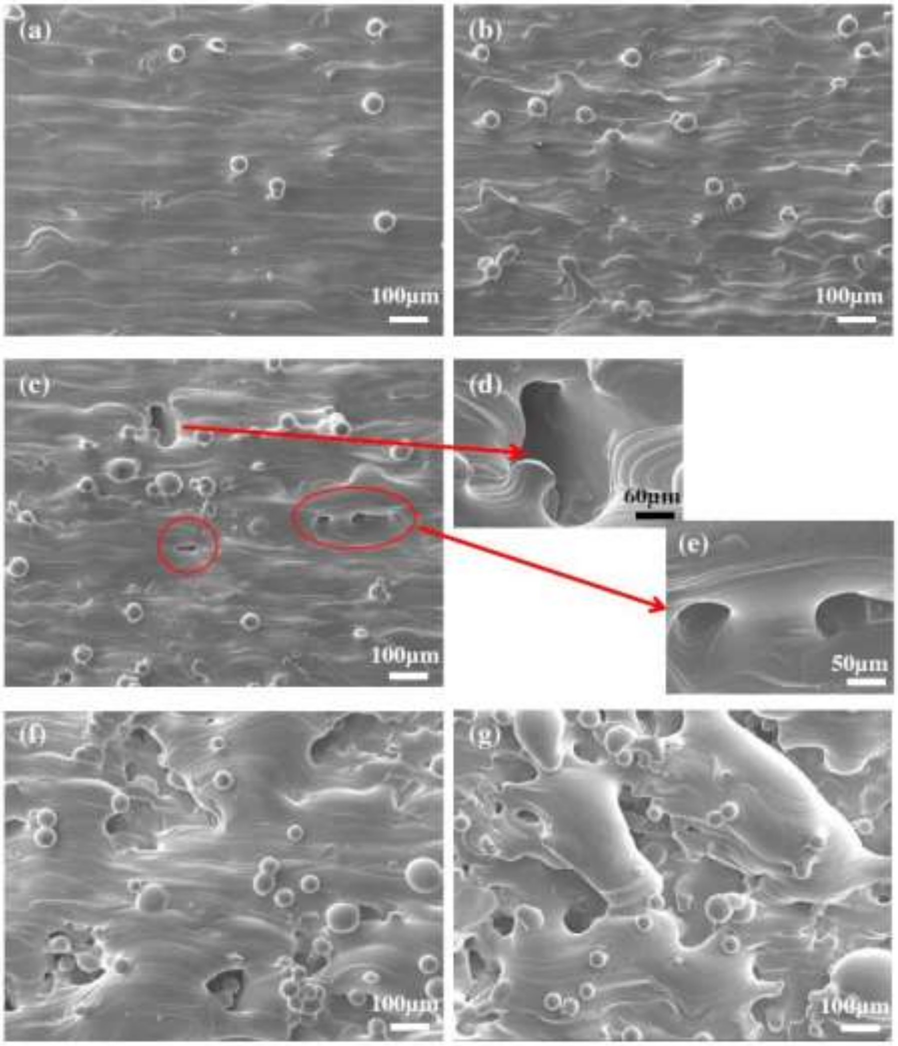

Fig. 1.3. SEM images of top as-built Ti64 surfaces with a layer thickness of (a) 20 μm; (b) 40 μm; (c,d,e) 60 μm; (f) 80 μm; (g) 100 μm adopted from [4].

- *Staircase effect*

The SLMed parts are an accumulation of consecutive layers on top of each other. Even in the case of building without any inclination angles, this discretized nature affects the side surface quality. On the other hand, when printing with specific angles, a staircase effect starts to occur. Fig. 1.4 shows a simplified scheme for the staircase effect and its relation with the layer thickness and build angle [13].

The same schematic illustrates the basic definition of down-skin and up-skin, which are used heavily to assess the quality of the built surfaces. Expectedly, part orientation has shown a remarkable impact on both the up-skin and the down-skin of the printed part for L-PBF and EB-PBF [14]. Fig. 1.5 demonstrates one of the best artifacts proposed to fully assess the building orientation impact on the resulted surface quality [15].

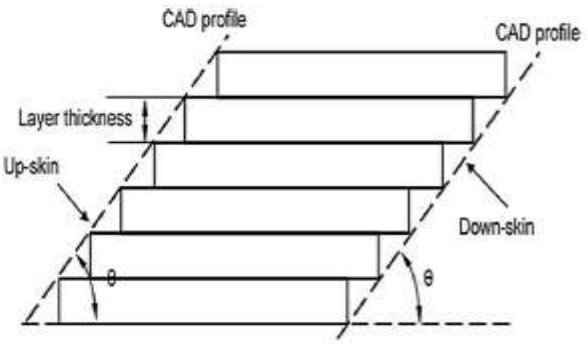

Fig. 1.4. Schematic drawings of staircase effect in Layered Manufacturing [13].

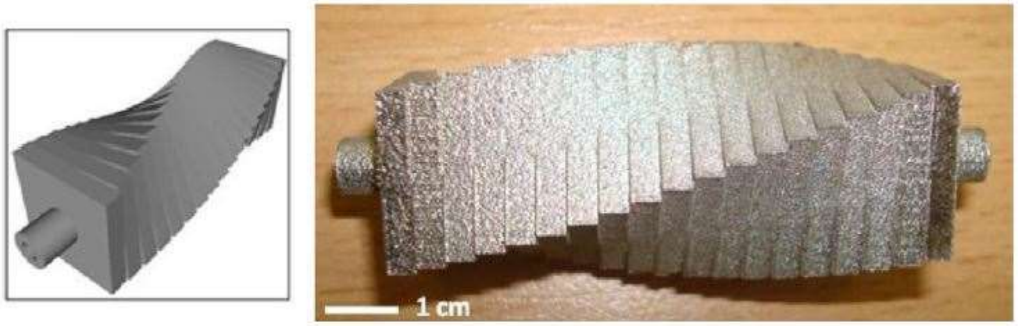

Fig. 1.5 An artifact with truncheon geometry to study roughness at various orientations [15].

In another finding, the down-skin exhibited higher sensitivity to the process parameters variation than the up-skin [16]. Fig. 1.6a shows a schematic demonstrating the powder size and layer thickness effect on the resulted surface quality. A cross-section of the printed down-skin is demonstrated in Fig. 1.6b. Red contour lines illustrate the melt pools on the down-skin surface, determining its roughness. Although decreasing layer thickness is favourable to reduce the staircase effect, at a certain threshold, the heat can be excessively producing higher thermal stresses, non-uniform solidification rate and total process instability [11, 17, 18].

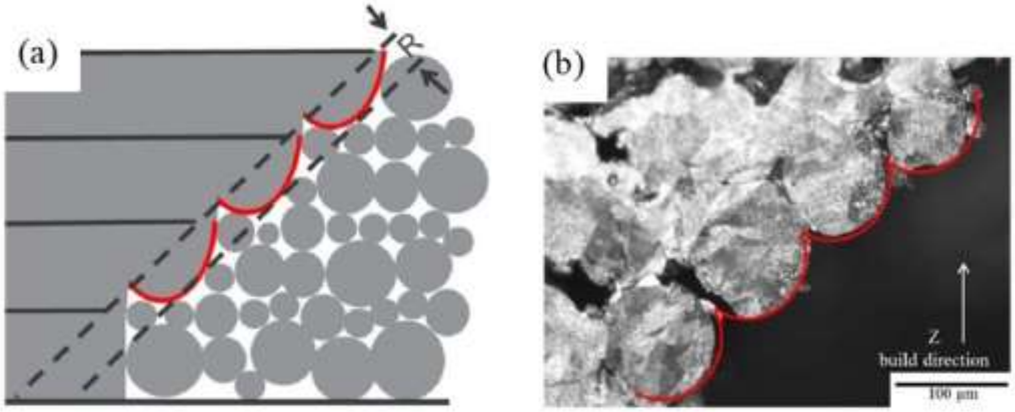

Fig. 1.6. (a) Resulted roughness schematic (b) cross-section image of a down-skin [16].

- *Balling phenomenon*

Balling phenomenon has been discussed in [8] through the single tracks process map (Fig. 1.7) for AISI 316L stainless steel indicating four different regions;

I Tracks without consolidation. At a low laser power, energy was insufficient to sinter powder particles.

II Tracks with significantly coarsened balls. The energy level is insufficient to cause a stable melting resulting in the formation of considerably coarsened balls.

III Tracks with small-sized balls and/or cracks. A reduction in surface energy and high melt instability produced rough tracks consisting of several small-sized balls and/or microscopic cracks on their surfaces.

IV Continuous and smooth tracks. Delivered energy forms a sufficient amount of liquid with reasonable stability, yielding continuous and smooth sintered tracks.

Balling phenomenon in SLM was further investigated for Inconel and stainless steel by [19] and tungsten by [20]; in this particular study, an argument was established to discuss the characterization of balling as illustrated in Fig. 1.8. The solidification rate for different materials was proven to be one of the critical issues, as stated by [20]. The solidification times for various materials used in SLM with respect to different temperatures considering initial Temperature 288 K is shown in Fig. 1.9.

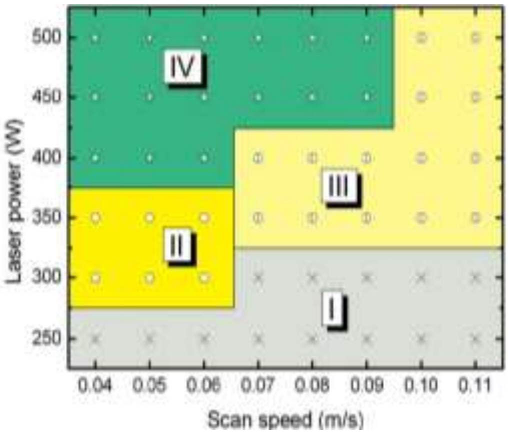

Fig. 1.7. Process map for DMLS of AISI 316L stainless steel [8].

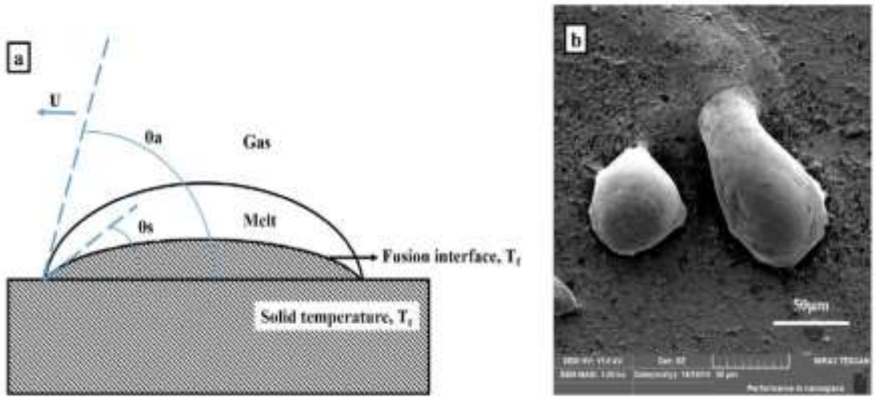

Fig. 1.8. (a) Schematic of the competitive relationship of the spreading and arresting of the melt line (b) SEM images of the morphology of one arrested droplet [20]

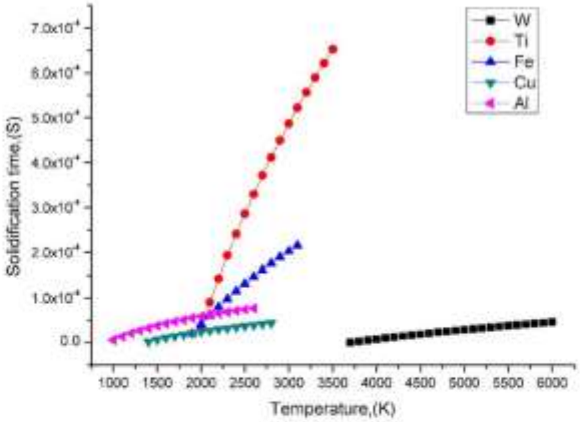

Fig. 1.9. Calculated solidification time plotted versus the temperature adopted from [20]

1.2.1.2 Surface characterization

Surface characterization can be done according to the following standards:

- **ISO 4287-1998** Geometrical Product Specifications (GPS)-Surface Texture: Profile Method - Terms, Definitions and Surface Texture Parameters [21].
- **ISO 4288-1998** Geometrical Product Specifications (GPS)-Surface Texture: Profile Method - Rules and Procedures for the Assessment of Surface Texture [22].

- **ISO 25178-2-2012** Geometrical Product Specifications (GPS) – Surface Texture: Area - Part 2: Terms, Definitions and Surface Texture Parameters [23].
- **ISO 25178-600-2015** Geometrical Product Specifications (GPS) – Surface Texture: Area - part 600: metrological characteristics for areal-topography measuring methods [24].
- **ASME B46.1-2009** Surface texture: (surface roughness, waviness, and lay) [25].
- **EUR 15178N-1993** Development of methods for the characterisation of roughness in three dimensions [26].

Out of these standards, specific parameters could be used for surface characterization. The most critical parameters between these parameters are amplitude parameters concerning heights of surface peaks and valleys, or spatial parameters concerned with spacing between corrugated features on the surface, parameters that combine both spatial and amplitude are called hybrid parameters. These concerning bearing areas are functional parameters, etc. Table 1.1. Indicate most of the parameters used to describe three-dimensional surface roughness; these parameters are sufficient to describe two-dimensional surface roughness except for volume functional parameters, functional indices and feature parameters. As mentioned before single parameter cannot be a good measure for accurate surface evaluation; using multiple parameters is always preferable to describe the surface. Yet, most of the literature on the surface quality of AM technologies explored only the simplistic stylus *R*a measurements.

Table 1.1 Three dimensional roughness parameters adopted from [27]

Symbol	Name of parameter	Standard
Amplitude parameters		
S_q (μm)	Root mean square height	ISO 25178
S_{sk}	Skewness	
S_{ku}	Kurtosis	
S_p (μm)	Maximum peak height	
S_v (μm)	Maximum pit height	
S_z (μm)	Maximum height	
S_a (μm)	Arithmetic mean height	
S_t (μm)	Total height	EUR 15178N
Spatial parameters		
S_{al} (mm)	Auto-correlation length	ISO 25178
S_{tr}	Texture-aspect ratio	
S_{td} (°)	Texture direction	
S_{al} (μm)	Fastest decay autocorrelation length	
Hybrid parameters		
S_{dq}	Root mean square gradient	ISO 25178
S_{dr} (%)	Developed interfacial area ratio	
S_{ds} (1/mm^2)	Density of summits	EUR 15178N
S_{sc} (1/mm)	Arithmetic mean summit curvature	
S_{fd}	Fractal dimension of the surface	
Functional parameters		
S_k (μm)	Core roughness depth	EUR 15178N
S_{pk} (μm)	Reduced summit height	
S_{vk} (μm)	Reduced valley depth	
S_{r1} (%)	Upper bearing area	
S_{r2} (%)	Lower bearing area	
S_{pq}	Plateau root mean square roughness	
S_{vq}	Valley root mean square roughness	
S_{mq}	Material ratio at plateau-to-valley transition	
S_{mr} (%)	Areal material ratio	ISO 25178
S_{mc} (μm)	Inverse areal material ratio	
S_{xp} (μm)	Extreme peak height	
S_{dc} (μm)	Areal height difference	
Volume functional parameters		
V_m (mm^3/mm^2) Material volume		ISO 25178
V_v (mm^3/mm^2) Void volume ISO 25178		
V_{mp} (mm^3/mm^2) Peak material volume		
V_{mc} (mm^3/mm^2) Core material volume		
V_{vc} Core void volume		
V_{vv} (mm^3/mm^2) Pit void volume		
Functional indices		
S_{bi}	Surface bearing index	EUR 15178N
S_{ci}	Core fluid retention index	
S_{vi}	Valley fluid retention index	
Feature parameters		
S_{pd} (1/mm^2)	Density of peaks	ISO 25178
S_{pc} (1/mm)	Arithmetic mean peak curvature	
S_{10z} (μm)	Ten-point height	
S_{5p} (μm)	Five-point peak height	
S_{5v} (μm)	Five-point pit height	
S_{da} (mm^2)	Mean dale area	
S_{ha} (mm^2)	Mean hill area	
S_{dv} (mm^3)	Mean dale volume	
S_{hv} (mm^3)	Mean hill volume	

1.2.2 Residual stresses

The RS can be classified according to the scale on which they occur [28]:

1. Type I: macro residual stresses that vary over large distances (mm scale).
2. Type II: micro residual stresses that vary over small distances (μm scale).
3. Type III: atomic-scale residual stresses that occur due to atomic dislocations.

Also, the RS, in General, can be attributed to the following [29]:

1. Spatial temperature gradient.
2. Thermal expansion variation, including the phase transformation effect.
3. Plasticity and flow stress.

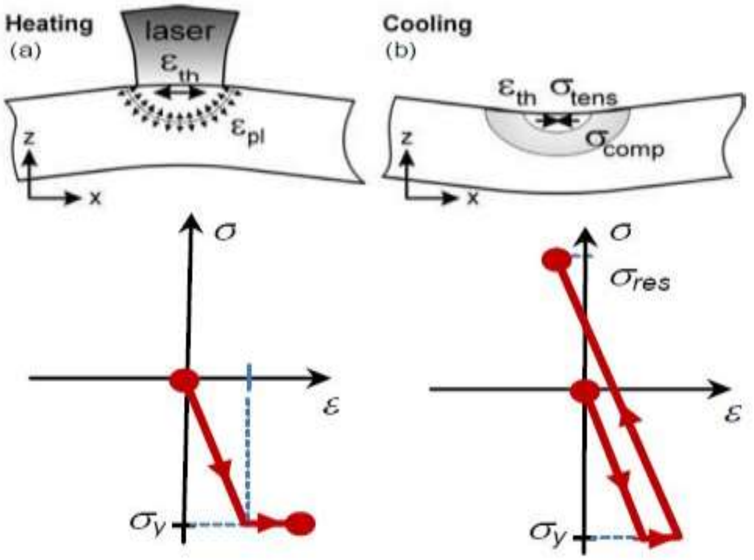

Fig. 1.10. Residual stresses formation model (a) Heating (b) cooling [30].

A steep temperature gradient is an inherent consequence of the deposition of liquid alloy powder on a relatively cooler substrate or prior deposited layers [31]

(Fig. 1.10). RS in AM parts is mainly attributed to such gradient, accompanied by phase transformation occasionally, leading to part distortion, delamination, the deterioration of the geometric tolerance, the fatigue performance, and the fracture resistance of the fabricated part [31, 32]. Fig. 1.11a and 3b show short and long cracks due to tensile residual stresses, and Fig. 1.11c shows an example of the delamination. A better understanding of the evolution of thermal stresses during AM is essential to control and mitigate the issues above.

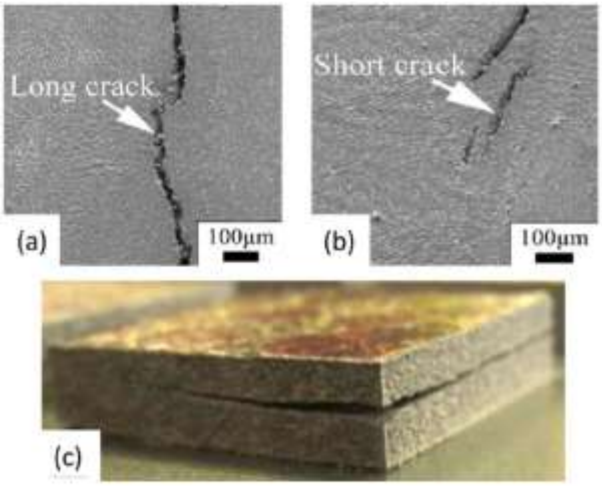

Fig. 1.11. Defects due to residual stresses (a) Long crack (b) Short crack [33] and (c) Delamination [34].

To provide such understanding, various RS measurement techniques are discussed in [28]. Fig. 1.12 demonstrates spatial resolution, measurement depth, and estimated cost for different measurement methods, determining the optimum strategy for each case. Moreover, for the AM processes, the resulted deformation is utilized to quantify the RS with several artifacts, for instance, bridge curvature (Fig. 5a) [35], cantilever structure (Fig. 5b) [36].

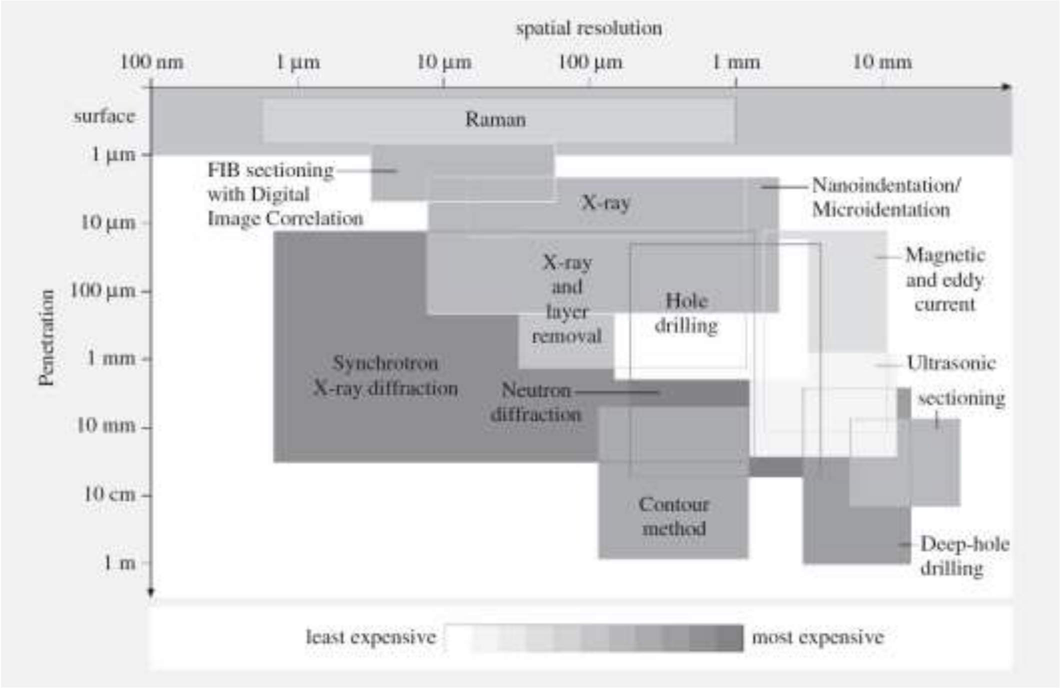

Fig. 1.12. Different RS measurement methods resolution, penetration, and cost [28].

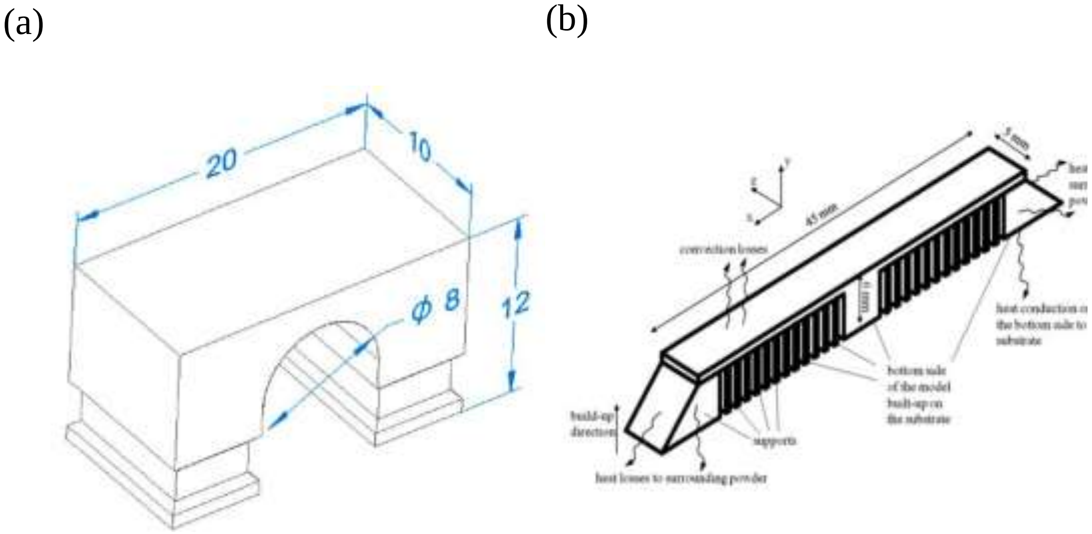

Fig. 1.13. Artifacts for RS quantification

(a) bridge curvature [35]. (b) cantilever structure [36].

The correlation between the resulting RS and different process control parameters was the target of several studies. Therefore, only some noticeable remarks are pointed out briefly:

1. The surface RS data for IN718 are scattered and cannot be related directly to power, scanning speed, and hatch spacing. Tensile RS are measured within range (300-600 MPa). But other research on 316L claims the significance of the power compared to the other process parameters [35].
2. Parts removal off the base plate usually leads to deformation accompanied by a drastic reduction of the RS [31].
3. Higher base plate thickness reduces the resulting RS for same-height parts [31], while increased part height increases the resulting RS [31, 37].
4. Materials with higher yield strength gain higher RS [31].
5. Dwell time between layers is tested and found disadvantageous for RS and consequently distortion [38, 39].
6. The sector scanning with a shorter scanning track length induces lower RS [35, 37].
7. Preheating the base plates reduces the resulting RS due to the lower temperature gradient [30], while other research [35] claim less impact of preheating the baseplate on the RS.

1.3 Surface texturing

The concept of surface texturing is widely used in our lives daily (Fig. 1.14), as it had been used for centuries. Take shoes` tread patterns, for example, used during the Tang Dynasty in China to allow workers to work on muddy grounds. Such texture evolves into thousands of patterns suitable for diverse users such as athletes, labours, medical workers, etc. The automotive industry adopted the same concept, as automobile tires are equipped with sophisticated surface textures to control friction, maintaining safe driving under various road conditions. With several patents and extensive studies, golf balls are another application comprising surface texturing to improve their aerodynamic characteristics.

Fig. 1.14. Examples of textured surfaces commonly used in daily life.

Recently, texturing is widely investigated for manufacturing various bio-inspired designs with a wide range of properties [40]. Thoroughly, texturing affects surface wettability [41-46], tribological behaviour [43, 44, 47-50], heat transfer [51, 52], corrosion resistance [42], and even residual stresses [53, 54]. The first stage of the current study will investigate surface texturing aiming at tailoring the first two properties, wettability and tribological response.

1.3.1 Wettability

Wettability refers to the interaction between the fluid and solid phases. Water repellent surfaces are called hydrophobic surfaces, and surfaces with a higher tendency to adhere to water are called hydrophilic. The static Contact Angle (CA) or Young`s angle can be quantified from the water droplet profile on any surface as the tangential angle at the liquid-solid-air interface [55]. Therefore, static CA is considered an excellent measure to characterize surface wetting. Surfaces showing lower contact angles are called hydrophilic surfaces, while surfaces showing higher contact angles are called hydrophobic surfaces (Fig. 1.15). On rough surfaces, surface wetting occurs in two main states; stable Wenzel state and metastable Cassie-Baxter state (Fig. 1.16).

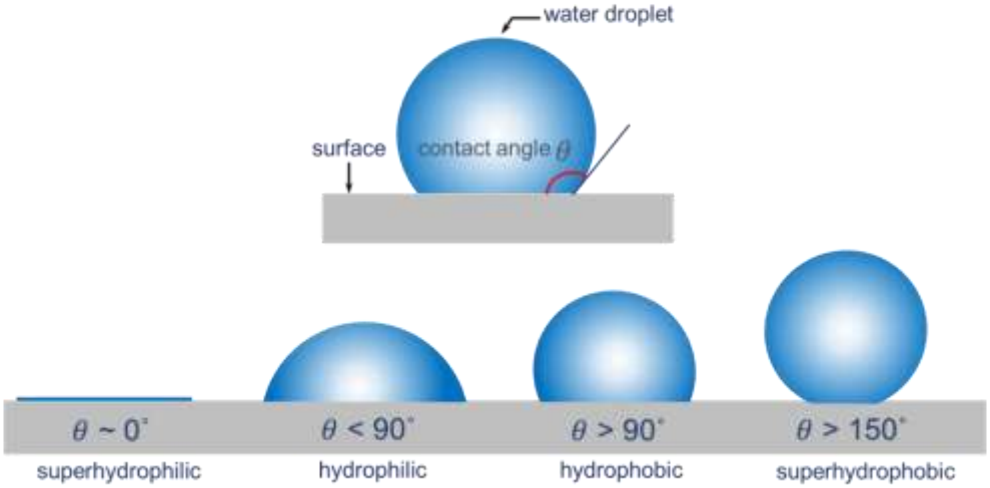

Fig. 1.15. Schematic of the static CA presenting various surface wetting conditions.

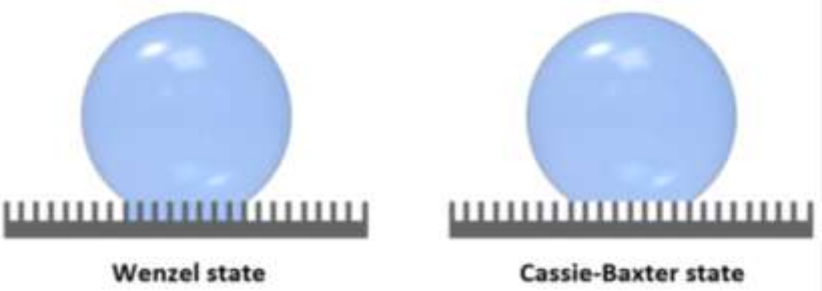

Fig. 1.16. Schematic of Wenzel and Cassie-Baxter wetting.

The wetting phenomenon depends on fluid and solid surface energies as well as surface topography. A famous example of superhydrophobic surfaces is the lotus leaf presented in Fig. 1.17, showing its 160° CA. Higher magnification images demonstrate lotus leaf surface topography and its hierarchical structure of micro-pillars and nano-pillars. Hydrophobic surfaces can be used for multiple applications like self-cleaning, anti-biofouling, and anti-icing. Techniques like laser surface texturing (LST) [42] (Fig. 1.18a), Wire-cut Electrical Discharge

Machining (WEDM) [46] (Fig. 1.18b), and sink EDM [45] were successfully used to produce robust metallic superhydrophobic surfaces.

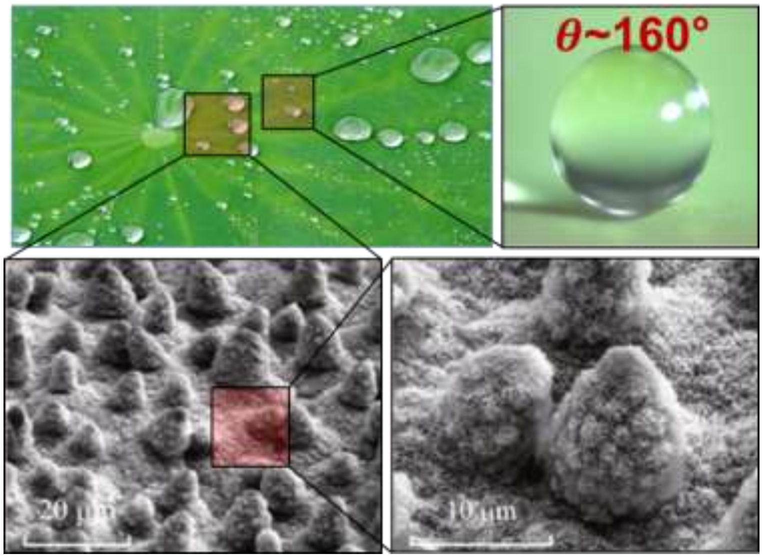

Fig. 1.17. Superhydrophobicity of the Lotus leaf showing its topography and CA.

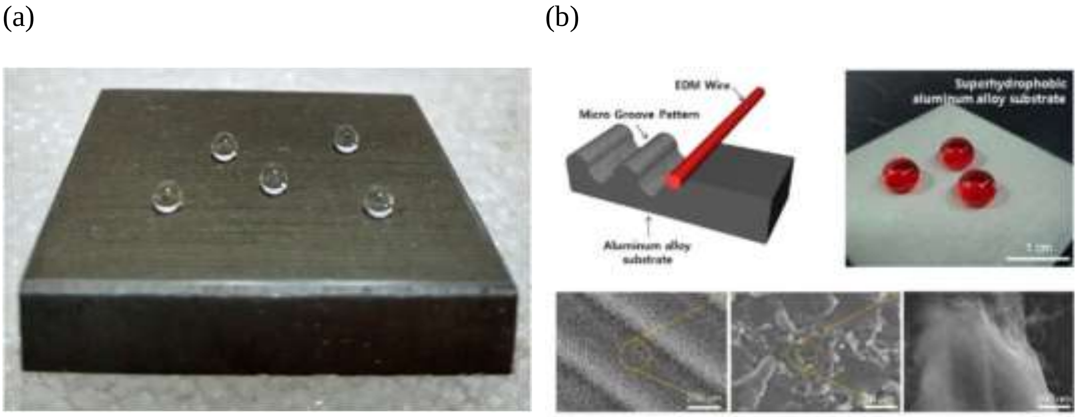

Fig. 1.18. (a) Hydrophobic surface produced by (a) LST [42]. (b) WEDM [46].

1.3.2 Tribological response

A substantial body of tribology-related research has highlighted the significance of surface texturing for controlling the coefficient of friction and wear rate [56]. Fig. 1.19 shows two potential applications in automotive and biomedical fields for textured surfaces with a tailored tribological response. Noticeably, even under various lubrication regimes, such engineered surfaces have exhibited enhanced tribological performance [57]. Table 1.2 summarizes the main effects of texturing on surface tribological response under different lubrication regimes. Surface texturing has been successfully used for multiple mechanical applications such as cylinder liners, cutting tools, journal bearing and mechanical seals [58]. Moreover, by introducing the appropriate surface texture, a great potential to increase the longevity of a prosthetic hip implant was achieved [59].

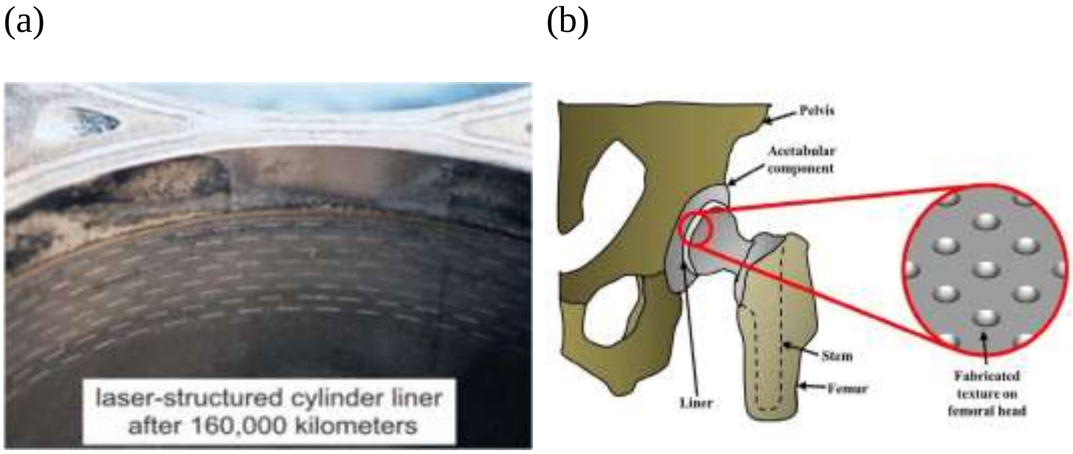

Fig. 1.19. Textured surfaces with enhanced tribological-behaviour for (a) automotive [58] (b) biomedical [59] applications.

Table 1.2 Summary of surface texturing impact on various lubrication regimes [60]

Lubrication regime		Main effects
Dry sliding		-Entrapment of wear debris -Reduction of contact area -Formation of tribolayers -Effect on stress distribution -Reduction in stiction
Boundary lubrication		-Friction increase -Edge of dimple wear by tensile cracking -dimple worn off -if texture can generate hydrostatic reaction force, wear disappears and friction reduction
Mixed lubrication		-Entrapment of wear debris -secondary oil effect -friction reduction(strong effect) -increase of film thickness -Shift in Stribeck curves
Full film lubrication	**HD**	-friction reduction -increase of load support -occasionally friction increase
	EHL	-film thickness varies (increased or decreased -friction varies (increased or decreased)

1.3.3 Other properties

Thermal properties of the textured surfaces like critical heat flux and heat transfer coefficient can be dramatically enhanced, as shown for the micro-structured AlSi10Mg surface fabricated by SLM [51]. Also, various texturing patterns can control the corrosion resistance of the textured surfaces [61]. In addition, Texturing can affect other properties such as the golf balls' aerodynamic characteristics, for instance, as mentioned in sec. 1.3.

1.4 Additive texturing

Surface texturing approaches can be categorized as bottom-up (additive) and bottom down (subtractive) surface modifications. To the moment, the additive approaches are frequently associated with soft materials that cannot withstand higher loading conditions. On the other hand, for hard metallic materials, numerous techniques are used, most of which are subtractive. Fig. 1.20 shows a list of such texturing techniques adopted from [62]. All the mentioned techniques can be considered post-processing techniques in which the surface undergoes two or more steps to realize the desired texture. Thus, AT concept holds the exceptional potential to fabricate, in-process, robust textured metallic surfaces to acquire the functional surface in a single step.

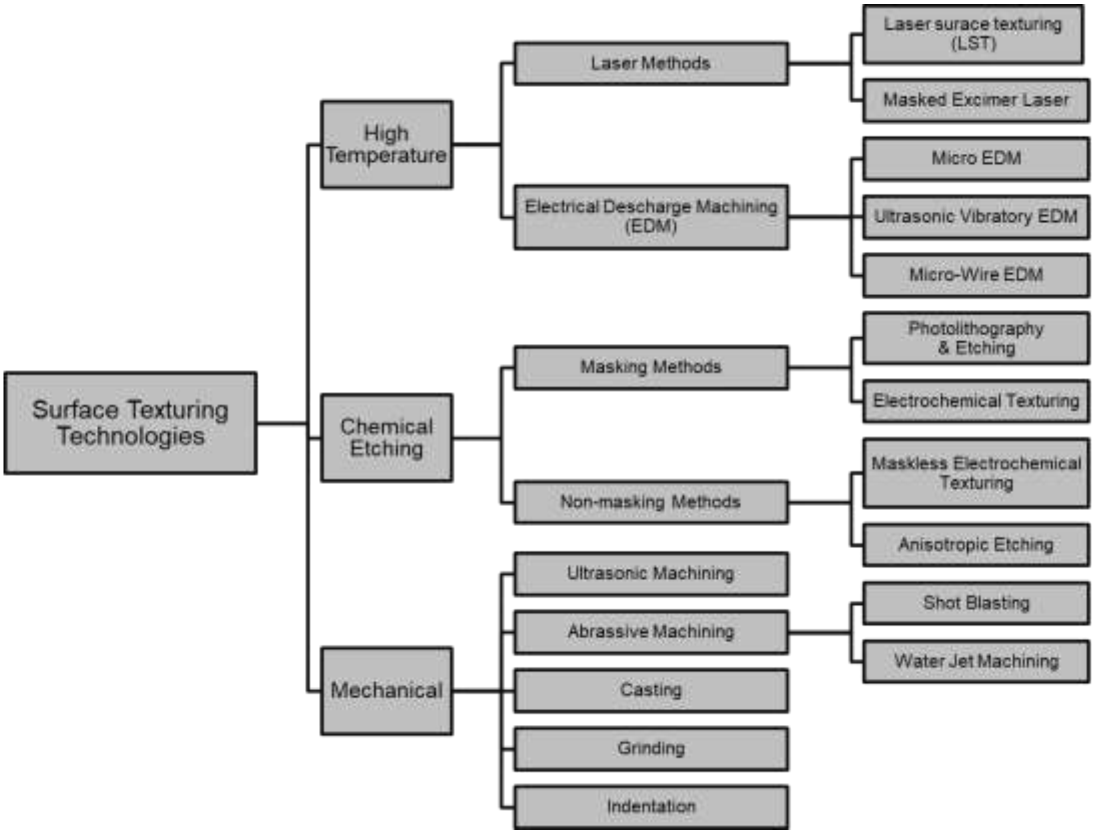

Fig. 1.20. Subtractive surface texturing techniques adopted from [62]

1.4.1 Minimum feature limits

Considering the microscale of the standard texture features, a knowledge of the minimum feature size and spacing possible in SLM is a precursor to the texturing investigations. Several designs to benchmark the performance of AM processes and machines in terms of geometrical and dimensional accuracy, repeatability, and minimum feature size are available in the literature, a comprehensive review of which can be found in [63]. Fig. 1.21 demonstrates the solid model of standardized artifact proposed to assess the investigated process capabilities.

Feature sizes considered in these works are on the order of mm, which does not entirely fall into the domain of texturing. A minimum feature size of 0.25 mm has been considered in an artifact intended for standardization [64]. A test part of characterizing micro AM is reported in [65]; however, this relates to digital light processing using polymer resins. Fine features obtainable in SLM are material dependent and are limited by the extent of the heat-affected zone, the positioning accuracy of the laser system, and the beam width compensation [64]. Accordingly, based on the guidelines offered in [63], custom artifacts are imperative to identify limiting feature geometry and dimensions that are specific to the material, machine, and processing parameters adopted.

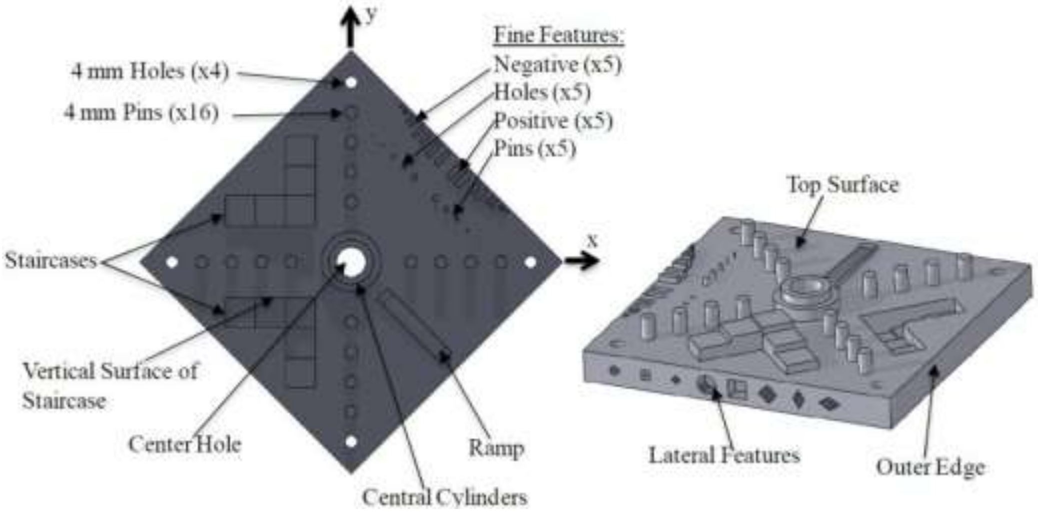

Fig. 1.21. Solid model of the proposed test artifact by NEST [66]

1.5 Laser peening

The majority of functional components in biomedical, aerospace and automotive industries are subjected to a severe cyclic loading causing structural damage and gradual or sudden failure. Thus, the service life of any component depends mainly on its fatigue resistance, as fatigue can be considered the most common type of structural damage. Fatigue is a progressive failure mechanism consisting of crack initiation and growth stages. Usually, crack nucleation occurs at stress concentration sites caused by pores, lower surface roughness, and dislocation pile-up, then the growth is mainly attributed to RS [67]. Therefore, prohibiting the propagation of cracks and sudden failures can be achieved by applying compressive RS to the components. LP is one of the most effective techniques to induce such compressive RS. LP utilizes high-intensity laser and short pulse duration in the order of nanoseconds to create high-pressure plasma at extremely high temperatures. Such high pressure introduce compressive shock wave into the material [68, 69].

The plasma has mainly two effects; thermal and mechanical. The target surface is coated with an opaque material (black paint or tape, Al foil or tape) to laser light. Such opaque material acts as an ablative layer that suppresses most of the thermal effect and transmits a pure mechanical pressure to the peened surface. Also, the treated surface can be covered with a tamping layer of dielectric material transparent to irradiating laser light (water or glass) to confine the pressure wave and direct it inside the targeted surface. Using both ablative and tamping layers is called “confined ablation mode” (Fig. 1.22), but LP can be performed without such layers in “direct ablation mode”. In direct ablation, a thin recast layer forms due to the thermal effect then it is removed after peening.

In confined mode, laser light passes through the transparent material; opaque material absorbs the laser energy and gets evaporated to form the plasma. This evaporation of opaque material reduces the thermal effects on the metallic material, increasing the mechanical impact on it. The confining medium also retards the free expansion of plasma, leading to higher pressures as compared to direct ablation mode. As a result, pressure in confined mode can be developed with 2-3 times longer pressure pulse duration than direct ablation mode [69, 70].

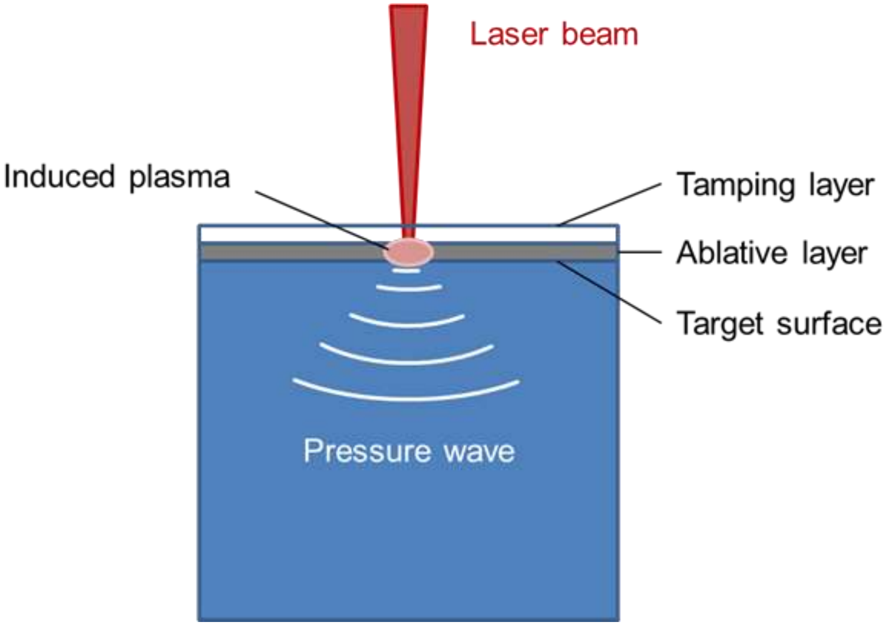

Fig. 1.22. Schematic of the confined mode LP.

1.5.1 Laser peening in additive manufacturing

Table 1.3 manifests the current research progress in utilizing the LP as a post-processing solution for the AM components. Compared to the large number of RS studies that highlighted the challenge of the acquired tensile RS for various materials, the presented literature is considered scarce. The LP process parameters were not investigated nor appropriately optimised to adapt to the AM parts microstructure as opposed to the conventionally processed parts. The literature demonstrated a considerable gap in exploring LP process parameters such as spot size, overlap, pattern, and power density. It’s worth mentioning that varying the laser irradiance or power density was never investigated for AM parts. Besides, properties such as hardness and wear resistance were largely overlooked.

Table 1.3. Current LP research associated with AM technologies.

Ref	Year	Material	AM	LP		Investigated properties
			process	NC	C	(measurement method)
[71]	2017	316L PH1 Steel	SLM	√	√	RS (HDM)
[72]	2017	316L	SLM		√	RS (HDM)
[73]	2019	316L	SLM	√	√	Micro-hardness Crystallography (EBSD)
[74]	2019	Ti6Al4V	SLM		√	RS (HDM) Distortion
[75]	2019	AlSi10Mg	SLM	√		Porosity (Micro-CT)
[76]	2018	316L	SLM	√		Distortion (Bar arc height) Fatigue
[77]	2020	Ti6Al4V	SLM			RS (XRD) Microstructure Micro-hardness Tensile stress
[78]	2019	IN 718	DMLS		√	RS (XRD) Microstructure Micro-hardness Surface roughness
[79]	2019	IN 718	DMLS		√	RS (XRD) Micro-hardness Wear rate (pin-on-disk)
[80]	2018	Ti-TC17	DED	√		RS (XRD) Microstructure Fatigue
[81]	2018	Ti6Al4V	DED		√	RS (HDM) Microstructure Micro-hardness Tensile stress
[82]	2018	Al-2319	Wire-arc		√	RS (HDM) Microstructure Micro-hardness Tensile stress

1.6 Motivation

Based on the presented literature, the functionality of the as-built AM components is negatively impacted by the inferior surface quality and the formation of tensile RS. The concept of AT presents an excellent approach to work around the lower surface quality challenge and realize functional AM surfaces. Motivated by the same strive to manufacture functional surfaces, LP offers an attractive candidate to post-process AM surfaces eliminating the tensile RS and inducing high compressive RS. With a view of employing the proposed resolutions, some challenges can be identified as follows:

- The literature lacks research on the SLM process limitations and its capabilities to realize intricate micro-features.
- The effect of process parameters on the minimum features size or geometry is untapped in the previous studies.
- The surveyed average texturing dimensions are lower than the SLM limiting feature size for functional textured hydrophobic surfaces.
- The efficacy of the relatively large scale texturing features on the surface functionality, especially with the inferior surface functionality, is unpredictable.
- The literature regarding the tribological response of the AM surfaces is scarce, especially for dry sliding conditions.
- The influence of texturing on the AM parts tribological response is entirely unexplored.

- The effectiveness of LP as a tool to induce compressive RS in AM metallic parts is not assessed.
- The impact of LP parameters to tailor RS, surface roughness, hardness, and wear resistance is not evaluated.

Such challenges exhibit the primary motivation for this study to explore, investigate, and fill these research gaps and lack of knowledge.

1.7 Research Objectives

The main objective of the present work is to expand the application envelope of the AM components by realizing functional surfaces either by in-process AT or by LP post-processing. This objective can be achieved by:

- Assessment of the minimum geometrical limits of a micro-feature fabricated via the SLM process.
- Introducing the novel concept of AT utilizing the investigated minimum features and valuate the acquired topography.
- Validating the effectiveness of AT to enhance the functionality of the textured surfaces by evaluating their surface wetting and tribological response.
- Defining the ideal texturing pattern geometry and dimension improving the desired functionalities.
- Optimizing the LP parameters to enhance the resulted RS, surface roughness, hardness, and wear resistance.

1.8 Thesis Outline

The main results of the presented thesis are introduced in three journal articles, one of which is already published and the other two are submitted for publication.

- The first chapter presents an introduction and a brief background on AM processes and the utilized L-PBF technique, referring to the surface roughness and tensile RS challenges. Also, it offers some insights on the surface texturing concept and its targeted functionalities; wetting and tribological response. Then, the LP treatment is explained, and the previous efforts to use it for AM are mentioned.
- The second chapter shows an assessment of the SLM process capabilities to produce fine features. Then, the novel concept of AT is introduced and validated by the fabrication of hydrophobic surfaces with CA exceeds 140°.
- The third chapter highlights the increased hardness and enhanced tribological response of AM parts compared to the conventionally processed. Also, the AT concept is utilized under dry sliding conditions to achieve up to 80% and 60% reduction of specific wear rate and CoF, respectively.
- The fourth chapter explores the impact of each LP parameter on the resulted RS. Moreover, the efficacy of the LP process to eliminate the AM inherited tensile RS challenge is validated by inducing nearly 500 MPa of compressive RS.

- The fifth chapter summarizes the scientific finding and conclusion of the thesis and mentions the potential future work.

References

[1] I. Gibson, D. Rosen, B. Stucker, and M. Khorasani, "Introduction and Basic Principles," in *Additive Manufacturing Technologies*, I. Gibson, D. Rosen, B. Stucker, and M. Khorasani, Eds., ed Cham: Springer International Publishing, 2021, pp. 1-21.

[2] T. DebRoy, H. Wei, J. Zuback, T. Mukherjee, J. Elmer, J. Milewski, *et al.*, "Additive manufacturing of metallic components–process, structure and properties," *Progress in Materials Science,* vol. 92, pp. 112-224, 2018.

[3] M. Yakout, M. Elbestawi, and S. C. Veldhuis, "Process-structure-property relationship for selective laser melting of aerospace alloys," 2018.

[4] C. Qiu, C. Panwisawas, M. Ward, H. C. Basoalto, J. W. Brooks, and M. M. Attallah, "On the role of melt flow into the surface structure and porosity development during selective laser melting," *Acta Materialia,* vol. 96, pp. 72-79, 2015.

[5] S. Rahmati and E. Vahabli, "Evaluation of analytical modeling for improvement of surface roughness of FDM test part using measurement results," *The International Journal of Advanced Manufacturing Technology,* vol. 79, pp. 823-829, July 01 2015.

[6] J.-P. Kruth, L. Froyen, J. Van Vaerenbergh, P. Mercelis, M. Rombouts, and B. Lauwers, "Selective laser melting of iron-based powder," *Journal of materials processing technology,* vol. 149, pp. 616-622, 2004.

[7] H. Niu and I. Chang, "Instability of scan tracks of selective laser sintering of high speed steel powder," *Scripta Materialia,* vol. 41, pp. 1229-1234, 1999.

[8] D. Gu and Y. Shen, "Balling phenomena in direct laser sintering of stainless steel powder: Metallurgical mechanisms and control methods," *Materials & Design,* vol. 30, pp. 2903-2910, 2009.

[9] Y. Lee and W. Zhang, "Mesoscopic simulation of heat transfer and fluid flow in laser powder bed additive manufacturing," in *Proceedings of the Annual International Solid Freeform Fabrication Symposium, Austin, TX, USA*, 2015, pp. 10-12.

[10] J.-P. Kruth, G. Levy, F. Klocke, and T. Childs, "Consolidation phenomena in laser and powder-bed based layered manufacturing," *CIRP annals*, vol. 56, pp. 730-759, 2007.

[11] B. Liu, R. Wildman, C. Tuck, I. Ashcroft, and R. Hague, "Investigation the effect of particle size distribution on processing parameters optimisation in selective laser melting process," *Additive Manufacturing Research Group, Loughborough University*, pp. 227-238, 2011.

[12] A. Maamoun, Y. Xue, M. Elbestawi, and S. Veldhuis, "Effect of selective laser melting process parameters on the quality of Al alloy parts: Powder characterization, density, surface roughness, and dimensional accuracy," *Materials,* vol. 11, p. 2343, 2018.

[13] Z. Chen, X. Wu, D. Tomus, and C. H. Davies, "Surface roughness of selective laser melted Ti-6Al-4V alloy components," *Additive Manufacturing,* vol. 21, pp. 91-103, 2018.

[14] A. Triantaphyllou, C. L. Giusca, G. D. Macaulay, F. Roerig, M. Hoebel, R. K. Leach, *et al.*, "Surface texture measurement for additive manufacturing," *Surface Topography: Metrology and Properties,* vol. 3, p. 024002, 2015.

[15] G. Strano, L. Hao, R. M. Everson, and K. E. Evans, "Surface roughness analysis, modelling and prediction in selective laser melting," *Journal of Materials Processing Technology,* vol. 213, pp. 589-597, 2013/04/01/ 2013.

[16] Y. Tian, D. Tomus, P. Rometsch, and X. Wu, "Influences of processing parameters on surface roughness of Hastelloy X produced by selective laser melting," *Additive Manufacturing,* vol. 13, pp. 103-112, 2017.

[17] E. Yasa, J. Deckers, and J. P. Kruth, "The investigation of the influence of laser re-melting on density, surface quality and microstructure of selective laser melting parts," *Rapid Prototyping Journal,* vol. 17, pp. 312-327, 2011.

[18] F. Calignano, D. Manfredi, E. P. Ambrosio, L. Iuliano, and P. Fino, "Influence of process parameters on surface roughness of aluminum parts produced by DMLS," *The International Journal of Advanced Manufacturing Technology,* vol. 67, pp. 2743-2751, August 01 2013.

[19] R. Li, J. Liu, Y. Shi, L. Wang, and W. Jiang, "Balling behavior of stainless steel and nickel powder during selective laser melting process," *The International Journal of Advanced Manufacturing Technology,* vol. 59, pp. 1025-1035, April 01 2012.

[20] X. Zhou, X. Liu, D. Zhang, Z. Shen, and W. Liu, "Balling phenomena in selective laser melted tungsten," *Journal of Materials Processing Technology*, vol. 222, pp. 33-42, 2015.

[21] ISO-4287, "Geometrical Product Specifications (GPS)-Surface Texture: Profile Method " in *Terms, Definitions and Surface Texture Parameters*, ed. Geneva: International Organisation for Standardization, 1998.

[22] ISO-4288, "Geometric Product Specifications (GPS) – Surface Texture: Profile Method " in *Rules and Procedures for the Assessment of Surface Texture*, ed. Geneva: International Organisation for Standardization, 1998.

[23] ISO-25178-2, "Geometrical Product Specifications (GPS) – Surface Texture: Area," in *Part 2: Terms, Definitions and Surface Texture Parameters*, ed. British Standards Institute: International Organisation for Standardization, 2012.

[24] ISO-25178-600, "Geometrical Product Specifications (GPS) – Surface Texture: Areal," in *part 600: metrological characteristics for areal-topography measuring methods*, ed. Geneva: International Organisation for Standardization, 2015.

[25] ASME-B46.1, "Surface texture: surface roughness,waviness, and lay," ed. New York: American Society of Mechanical Engineers, 2009.

[26] K. Stout, P. Sullivan, W. Dong, E. Mainsah, N. Luo, T. Mathia, *et al.*, "Development of methods for the characterisation of roughness in three dimensions. Publication no. EUR 15178," *Commission of the European Communities, Bruxelles,* 1993.

[27] R. Deltombe, K. Kubiak, and M. Bigerelle, "How to select the most relevant 3D roughness parameters of a surface," *Scanning: The Journal of Scanning Microscopies,* vol. 36, pp. 150-160, 2014.

[28] G. S. Schajer and C. O. Ruud, "Overview of residual stresses and their measurement," *Practical residual stress measurement methods. 1st Edition. Hoboken: John Wiley & Sons,* pp. 1-27, 2013.

[29] T. DebRoy, H. L. Wei, J. S. Zuback, T. Mukherjee, J. W. Elmer, J. O. Milewski, *et al.*, "Additive manufacturing of metallic components – Process, structure and properties," *Progress in Materials Science,* vol. 92, pp. 112-224, 2018/03/01/ 2018.

[30] C. Li, Z. Liu, X. Fang, and Y. Guo, "Residual stress in metal additive manufacturing," *Procedia CIRP,* vol. 71, pp. 348-353, 2018.

[31] P. Mercelis and J.-P. Kruth, "Residual stresses in selective laser sintering and selective laser melting," *Rapid prototyping journal,* vol. 12, pp. 254-265, 2006.

[32] G. K. Lewis and E. Schlienger, "Practical considerations and capabilities for laser assisted direct metal deposition," *Materials & Design,* vol. 21, pp. 417-423, 2000.

[33] X. Zhao, X. Lin, J. Chen, L. Xue, and W. Huang, "The effect of hot isostatic pressing on crack healing, microstructure, mechanical properties of Rene88DT superalloy prepared by laser solid forming," *Materials Science and Engineering: A,* vol. 504, pp. 129-134, 2009.

[34] K. Kempen, L. Thijs, B. Vrancken, S. Buls, J. Van Humbeeck, and J. Kruth, "Producing crack-free, high density M2 Hss parts by selective laser melting: pre-heating the baseplate," in *Proc. 24th Int. Solid Free. Fabr. Symp,* 2013, pp. 131-139.

[35] J. Hajnys, M. Pagáč, J. Měsíček, J. Petru, and M. Król, "Influence of Scanning Strategy Parameters on Residual Stress in the SLM Process According to the Bridge Curvature Method for AISI 316L Stainless Steel," *Materials,* vol. 13, p. 1659, 2020.

[36] L. Papadakis, A. Loizou, J. Risse, S. Bremen, and J. Schrage, "A computational reduction model for appraising structural effects in selective laser melting manufacturing," *Virtual and Physical Prototyping,* vol. 9, pp. 17-25, 2014/01/02 2014.

[37] Y. Liu, Y. Yang, and D. Wang, "A study on the residual stress during selective laser melting (SLM) of metallic powder," *The International Journal of Advanced Manufacturing Technology,* vol. 87, pp. 647-656, 2016.

[38] E. R. Denlinger, J. C. Heigel, P. Michaleris, and T. Palmer, "Effect of inter-layer dwell time on distortion and residual stress in additive manufacturing of titanium and nickel alloys," *Journal of Materials Processing Technology,* vol. 215, pp. 123-131, 2015.

[39] S. Y. Ivanov, A. Vildanov, P. A. Golovin, A. Artinov, and I. Karpov, "Effect of Inter-Layer Dwell Time on Distortion and Residual Stresses of Laser Metal Deposited Wall," in *Key Engineering Materials*, 2019, pp. 445-451.

[40] B. Bhushan and Y. C. Jung, "Natural and biomimetic artificial surfaces for superhydrophobicity, self-cleaning, low adhesion, and drag reduction," *Progress in Materials Science*, vol. 56, pp. 1-108, 2011/01/01/ 2011.

[41] A. Cunha, A. P. Serro, V. Oliveira, A. Almeida, R. Vilar, and M.-C. Durrieu, "Wetting behaviour of femtosecond laser textured Ti–6Al–4V surfaces," *Applied Surface Science*, vol. 265, pp. 688-696, 2013/01/15/ 2013.

[42] Q. Ma, Z. Tong, W. Wang, and G. Dong, "Fabricating robust and repairable superhydrophobic surface on carbon steel by nanosecond laser texturing for corrosion protection," *Applied Surface Science*, vol. 455, pp. 748-757, 2018.

[43] T. Roy, D. Choudhury, S. Ghosh, A. B. Mamat, and B. Pingguan-Murphy, "Improved friction and wear performance of micro dimpled ceramic-on-ceramic interface for hip joint arthroplasty," *Ceramics International*, vol. 41, pp. 681-690, 2015.

[44] S. Ghosh, D. Choudhury, T. Roy, A. B. Mamat, H. Masjuki, and B. Pingguan-Murphy, "Tribological investigation of diamond-like carbon coated micro-dimpled surface under bovine serum and osteoarthritis oriented synovial fluid," *Science and technology of advanced materials*, vol. 16, p. 035002, 2015.

[45] C. Guo, P. Koshy, F. Coelho, and P. R. Selvaganapathy, "Sink electrical discharge machining of hydrophobic surfaces," *CIRP Annals*, 2019.

[46] W. G. Bae, K. Y. Song, Y. Rahmawan, C. N. Chu, D. Kim, D. K. Chung, *et al.*, "One-step process for superhydrophobic metallic surfaces by wire electrical discharge machining," *ACS applied materials & interfaces*, vol. 4, pp. 3685-3691, 2012.

[47] D. He, S. Zheng, J. Pu, G. Zhang, and L. Hu, "Improving tribological properties of titanium alloys by combining laser surface texturing and diamond-like carbon film," *Tribology international*, vol. 82, pp. 20-27, 2015.

[48] H. Yu, H. Deng, W. Huang, and X. Wang, "The effect of dimple shapes on friction of parallel surfaces," *Proceedings of the Institution of Mechanical Engineers, Part J: Journal of Engineering Tribology*, vol. 225, pp. 693-703, 2011.

[49] A. Dunn, J. V. Carstensen, K. L. Wlodarczyk, E. B. Hansen, J. Gabzdyl, P. M. Harrison, *et al.*, "Nanosecond laser texturing for high friction applications," *Optics and Lasers in Engineering*, vol. 62, pp. 9-16, 2014.

[50] A. Dunn, K. Wlodarczyk, J. Carstensen, E. Hansen, J. Gabzdyl, P. Harrison, *et al.*, "Laser surface texturing for high friction contacts," *Applied Surface Science,* vol. 357, pp. 2313-2319, 2015.

[51] J. Y. Ho, K. K. Wong, and K. C. Leong, "Saturated pool boiling of FC-72 from enhanced surfaces produced by selective laser melting," *International Journal of Heat and Mass Transfer,* vol. 99, pp. 107-121, 2016.

[52] C. K. Yu, D. C. Lu, and T. C. Cheng, "Pool boiling heat transfer on artificial micro-cavity surfaces in dielectric fluid FC-72," *Journal of Micromechanics and Microengineering,* vol. 16, p. 2092, 2006.

[53] R. Kumari, T. Scharnweber, W. Pfleging, H. Besser, and J. D. Majumdar, "Laser surface textured titanium alloy (Ti–6Al–4V)–Part II–Studies on bio-compatibility," *Applied Surface Science,* vol. 357, pp. 750-758, 2015.

[54] W. Pfleging, R. Kumari, H. Besser, T. Scharnweber, and J. D. Majumdar, "Laser surface textured titanium alloy (Ti–6Al–4V): Part 1–Surface characterization," *Applied Surface Science,* vol. 355, pp. 104-111, 2015.

[55] K.-Y. Law and H. Zhao, "Contact Angle Measurements and Surface Characterization Techniques," in *Surface Wetting,* ed: Springer, 2016, pp. 7-34.

[56] T. Ibatan, M. S. Uddin, and M. A. K. Chowdhury, "Recent development on surface texturing in enhancing tribological performance of bearing sliders," *Surface and Coatings Technology,* vol. 272, pp. 102-120, 2015/06/25/ 2015.

[57] C. Gachot, A. Rosenkranz, S. M. Hsu, and H. L. Costa, "A critical assessment of surface texturing for friction and wear improvement," *Wear,* vol. 372-373, pp. 21-41, 2017/02/15/ 2017.

[58] P. Lu and R. J. K. Wood, "Tribological performance of surface texturing in mechanical applications—a review," *Surface Topography: Metrology and Properties,* vol. 8, p. 043001, 2020/09/17 2020.

[59] A. Chyr, M. Qiu, J. W. Speltz, R. L. Jacobsen, A. P. Sanders, and B. Raeymaekers, "A patterned microtexture to reduce friction and increase longevity of prosthetic hip joints," *Wear,* vol. 315, pp. 51-57, 2014.

[60] C. Gachot, A. Rosenkranz, S. Hsu, and H. Costa, "A critical assessment of surface texturing for friction and wear improvement," *Wear,* vol. 372, pp. 21-41, 2017.

[61] J. I. Ahuir-Torres, M. A. Arenas, W. Perrie, G. Dearden, and J. de Damborenea, "Surface texturing of aluminium alloy AA2024-T3 by picosecond laser: Effect on wettability and corrosion properties," *Surface and Coatings Technology,* vol. 321, pp. 279-291, 2017/07/15/ 2017.

[62] D. Choudhury, T. Roy, and I. Krupka, "Surface Modifications and Tribological Effect in Orthopedics Implants," *Processing Techniques and Tribological Behavior of Composite Materials,* pp. 193-217, 2015.

[63] L. Rebaioli and I. Fassi, "A review on benchmark artifacts for evaluating the geometrical performance of additive manufacturing processes," *The International Journal of Advanced Manufacturing Technology,* vol. 93, pp. 2571-2598, 2017.

[64] S. Moylan, J. Slotwinski, A. Cooke, K. Jurrens, and M. A. Donmez, "An additive manufacturing test artifact," *Journal of research of the National Institute of Standards and Technology,* vol. 119, p. 429, 2014.

[65] M. K. Thompson and M. Mischkot, "Design of Test Parts to Characterize Micro Additive Manufacturing Processes," *Procedia CIRP,* vol. 34, pp. 223-228, 2015/01/01/ 2015.

[66] S. Moylan, J. Slotwinski, A. Cooke, K. Jurrens, and M. A. Donmez, "Proposal for a standardized test artifact for additive manufacturing machines and processes," in *Proceedings of the 2012 annual international solid freeform fabrication symposium*, 2012, pp. 6-8.

[67] M. J. Yadav, A. Jinoop, C. Danduk, and S. K. Subbu, "Laser Shock Processing: Process Physics, Parameters, and Applications," *Materials Today: Proceedings,* vol. 4, pp. 7921-7930, 2017.

[68] R. Fabbro, J. Fournier, P. Ballard, D. Devaux, and J. Virmont, "Physical study of laser-produced plasma in confined geometry," *Journal of applied physics,* vol. 68, pp. 775-784, 1990.

[69] P. Peyre and R. Fabbro, "Laser shock processing: a review of the physics and applications," *Optical and quantum electronics,* vol. 27, pp. 1213-1229, 1995.

[70] K. Ding and L. Ye, *Laser shock peening: performance and process simulation*: Woodhead Publishing, 2006.

[71] N. Kalentics, E. Boillat, P. Peyre, S. Ćirić-Kostić, N. Bogojević, and R. E. Logé, "Tailoring residual stress profile of Selective Laser Melted parts by Laser Shock Peening," *Additive Manufacturing,* vol. 16, pp. 90-97, 2017/08/01/ 2017.

[72] N. Kalentics, E. Boillat, P. Peyre, C. Gorny, C. Kenel, C. Leinenbach, *et al.*, "3D Laser Shock Peening – A new method for the 3D control of residual stresses in Selective Laser Melting," *Materials & Design,* vol. 130, pp. 350-356, 2017/09/15/ 2017.

[73] N. Kalentics, K. Huang, M. O. V. de Seijas, A. Burn, V. Romano, and R. E. Logé, "Laser shock peening: a promising tool for tailoring metallic microstructures in selective laser melting," *Journal of Materials Processing Technology,* vol. 266, pp. 612-618, 2019.

[74] N. Kalentics, A. Burn, M. Cloots, and R. E. Logé, "3D laser shock peening as a way to improve geometrical accuracy in selective laser melting," *The International Journal of Advanced Manufacturing Technology,* vol. 101, pp. 1247-1254, 2019/04/01 2019.

[75] A. Du Plessis, D. Glaser, H. Moller, N. Mathe, L. Tshabalala, B. Mfusi, *et al.*, "Pore closure effect of laser shock peening of additively manufactured AlSi10Mg," *3D Printing and Additive Manufacturing,* vol. 6, pp. 245-252, 2019.

[76] L. Hackel, J. R. Rankin, A. Rubenchik, W. E. King, and M. Matthews, "Laser peening: A tool for additive manufacturing post-processing," *Additive Manufacturing,* vol. 24, pp. 67-75, 2018.

[77] J. Lu, H. Lu, X. Xu, J. Yao, J. Cai, and K. Luo, "High-performance integrated additive manufacturing with laser shock peening–induced microstructural evolution and improvement in mechanical properties of Ti6Al4V alloy components," *International Journal of Machine Tools and Manufacture,* vol. 148, p. 103475, 2020.

[78] N. N. Kumar, A. C. Yadav, K. Raja, S. Prabhakaran, C. D. Naiju, and S. Kalainathan, "Study on Effect of Laser Peening on Inconel 718 Produced by DMLS Technique," SAE Technical Paper 0148-7191, 2019.

[79] A. N. Jinoop, S. K. Subbu, C. P. Paul, and I. A. Palani, "Post-processing of Laser Additive Manufactured Inconel 718 Using Laser Shock Peening," *International Journal of Precision Engineering and Manufacturing,* vol. 20, pp. 1621-1628, 2019/09/01 2019.

[80] S. Luo, W. He, K. Chen, X. Nie, L. Zhou, and Y. Li, "Regain the fatigue strength of laser additive manufactured Ti alloy via laser shock peening," *Journal of Alloys and Compounds,* vol. 750, pp. 626-635, 2018.

[81] W. Guo, R. Sun, B. Song, Y. Zhu, F. Li, Z. Che, *et al.*, "Laser shock peening of laser additive manufactured Ti6Al4V titanium alloy," *Surface and Coatings Technology*, vol. 349, pp. 503-510, 2018/09/15/ 2018.

[82] R. Sun, L. Li, Y. Zhu, W. Guo, P. Peng, B. Cong, *et al.*, "Microstructure, residual stress and tensile properties control of wire-arc additive manufactured 2319 aluminum alloy with laser shock peening," *Journal of Alloys and Compounds*, vol. 747, pp. 255-265, 2018.

Chapter 2

Additive Texturing of Metallic Surfaces for Wetting Control

Complete Citation:

S. Mekhiel, Philip Koshy, M.A. Elbestawi. (2021). Additive Texturing of Metallic Surfaces for Wetting Control, *Additive Manufacturing*.

Doi: 10.1016/j.addma.2020.101631.

Copyright:

Relative Contributions:

S. Mekhiel:	Conceptualization, Methodology, Experimental work, Investigation, Writing – original draft preparation, Writing – review & editing.
Philip Koshy:	Supervision, Conceptualization, Methodology, Investigation, Writing – review & editing.
M. A. Elbestawi:	Supervision, Conceptualization, Methodology, Writing – review & editing.

Abstract

Additive Manufacturing (AM) has enabled the realization of custom products with intricate geometric features that are either too complex or even intractable for subtractive manufacturing processes. On the other hand, owing to their relatively poor roughness, functional surfaces generated in AM have to be often finish machined. This research explored the prospect of turning this limitation around by pursuing a novel concept of Additive Texturing (AT) wherein the topography of an AM part is tailored in-process to entail textures that further enhance the functionality of an AM product. In this context, the limits of the selective laser melting process in printing metallic surface microfeatures were investigated as a precursor to realizing texture patterns comprising pillars, channels, and re-entrant structures. Following on from this, the efficacy of such textures in controlling the wetting behaviour of stainless steel AM surfaces was examined. The notion of AT is demonstrated in terms of its capability to generate hydrophobic AM surfaces with water contact angles exceeding 140°.

Keywords: Additive Manufacturing, Hydrophobicity, Selective Laser Melting, Surface Texturing, Wettability.

2.1 Introduction

Additive Manufacturing (AM) technologies have emerged to occupy a niche domain in the realm of manufacturing processes on account of the design freedom they offer to enhance component functionality. This is particularly true in terms of the capability of AM to realize features of a complex geometry that are either expensive or impossible to manufacture using conventional subtractive manufacturing processes, due to restrictions arising from tooling access. Additionally, attributes that render AM to be appealing are the significant decrease in the lead time from design to product realization, advantages accruing from a reduction in the number of parts, and the cost and time savings associated with machine set-up, tooling and assembly [1].

The work presented in this paper seeks to further expand the application envelope and process capability of AM processes by introducing the novel notion of “Additive Texturing” (AT). This refers to the adaptation of AM towards engineering the topography of a printed surface towards realizing functional attributes. This represents a significant value addition as it enables AM parts to comprise a surface functionality through in-place printing of textured surfaces with designed surface features, without having to invoke additional secondary processes. The present work will specifically refer to selective laser melting (SLM) of metallic components with a continuous laser, and demonstrate the concept by printing and testing surfaces that have been designed to possess controlled wettability. Currently, there appears to have been only one such SLM-related texturing work: the fabrication of microcavities and microfins, which by virtue of being active bubble nucleation sites have been shown to be effective in enhancing the heat transfer coefficient and critical heat flux in pool boiling [2].

A significant extent of AM research has focused on microstructure in the component bulk, and the characterization of material-specific mechanical properties of components such as relative density, strength, microhardness and residual stresses [1]. This has led to the process–structure–property paradigm that is considered the core of AM research and development. Investigations on surfaces generated in AM on the other hand have thus far not been as widely investigated. Although surface features are indeed signatures of complex multi-physical phenomena underlying the AM process, in several instances AM surfaces have been characterized only towards assessing the capability of the AM technology at hand [3]. Currently, metrology of AM surface textures is likewise somewhat rudimentary, with measurements largely limited to two-dimensional stylus measurements [3]. This is perhaps not entirely surprising given that in most applications the built surface would have to be post-processed using machining to obtain a surface quality consistent with functional requirements. The present work strives to flip the surface quality limitation of AM around into engineering the topography of a printed surface, so as to realize surfaces with defined features to impart controlled wettability.

Bio-inspired texturing of functional surfaces has of late garnered the attention of researchers resulting in intriguing applications [4]. Examples include dimpled features that can trap lubricants and wear debris to enhance tribological response, features that can facilitate osseointegration of biomedical implants, and generation of features that can manipulate attributes like coating adhesion, fluid drag, and surface traction. The present work focuses on surface wetting as alluded to previously, and specifically refers to water-repellant (hydrophobic) surfaces inspired by biological surfaces such as lotus leaves. Such surfaces may be generated using processes like sol-gel processing, lithography and electrospinning, however, they pertain to soft materials like polymers that lack mechanical durability. For fabricating robust metallic surfaces, laser micromachining [5] and electrical discharge machining [6] have been effective. Given the microscale of the textures generated in these processes, the substrate would need to be polished for such textural features to be functionally effective [7]. Considering that the high surface roughness inherent to additively manufactured surfaces would inevitably mask the microfeatures, the as-built surfaces would need to be finish machined and polished prior to texturing. This represents additional infrastructure and multiple process steps that significantly add to the processing time and cost. To this end, the objective of the present work has been to generate metallic hydrophobic surfaces in-process and in a single step directly using SLM with no requirements for post-processing.

Considering that standard texture features are typically on the microscale, a knowledge of the minimum feature size and spacing possible in SLM is a precursor to texturing investigations. A number of designs to benchmark the performance of AM processes and machines in terms of geometrical and dimensional accuracy, repeatability, and minimum feature size are available in the literature, a comprehensive review of which can be found in [8]. Feature sizes considered in these works are on the order of mm which does not quite fall into the domain of texturing. A minimum feature size of 0.25 mm has been considered in an artifact intended for standardization [9]. A test part to characterize micro AM is reported in [10], however, this relates to digital light processing using polymer resins. Fine features obtainable in SLM are material dependent and are limited by the extent of the heat-affected zone, the positioning accuracy of the laser system, and the beam width compensation [9]. Accordingly, in the first phase of the present work, test coupons were designed and printed based on the guidelines offered in [8] to identify limiting feature attributes that are specific to the material, machine and processing parameters adopted.

Following test artifact investigations, this work investigated the surface roughness of the as-built surfaces under various process parameters, and their wettability was assessed in terms of the static contact angle (CA) with water as the working fluid. Single tracks were printed thereafter to identify the minimum achievable line width. This was followed by investigations on top and side surfaces (normal and parallel to the build direction) printed with pillar, channel and re-entrant pattern arrays of various dimensions to characterize the corresponding wettability, which provided the proof-of-concept of generating hydrophobic surfaces with CA exceeding 140°.

2.2 Experimental

2.2.1 Material and process parameters

The feedstock was a gas atomized AISI 316L stainless steel powder of 15–45 µm particle size. Samples were built using an SLM machine (EOS M280) with a 400 W continuous ytterbium fiber laser, in a nitrogen atmosphere. The layer thickness and stripe width were maintained constant at 0.04 mm and 100 mm, respectively. Samples were positioned on the build plate within the stripe width to avoid stripe overlap. The effect of process parameters was interpreted in terms of the volumetric (E_V) and linear (E_L) energy densities, respectively obtained as (P/vht) and (P/vt), where P is the laser power, v is the scanning speed, t is the layer thickness and h is the hatch spacing.

2.2.2 Artifacts for limiting feature dimensions

Three custom coupon designs were used to assess the limiting dimensions in SLM. The first coupon comprised periodic protruding trapezoidal features wherein the parallel sides decreased linearly from 0.6 mm to 0.01 mm over a length of 45 mm, to continuously assess the minimum printable feature width. The space between the protruding features corresponds to sunk trapezoidal features (Fig. 2.1a). The coupon had twelve such trapezoids of depths ranging from one to twelve layer thickness, to detect any interaction between the limiting feature width and depth.

The second coupon referred to the minimum spacing between protruding and sunk features of 0.4 mm width and was of a geometry shown in Fig. 2.1b. The spacing was altered from 0.5 mm to 0.1 mm in increments of 0.1 mm, and from 0.1 and 0.01 mm in increments of 0.01 mm. The depth of all features was held constant at 0.4 mm. Both coupons were printed using two sets of process parameters (

Table 2.1), which were previously identified to correspond to the maximum density and strength for the same material and machine [11].

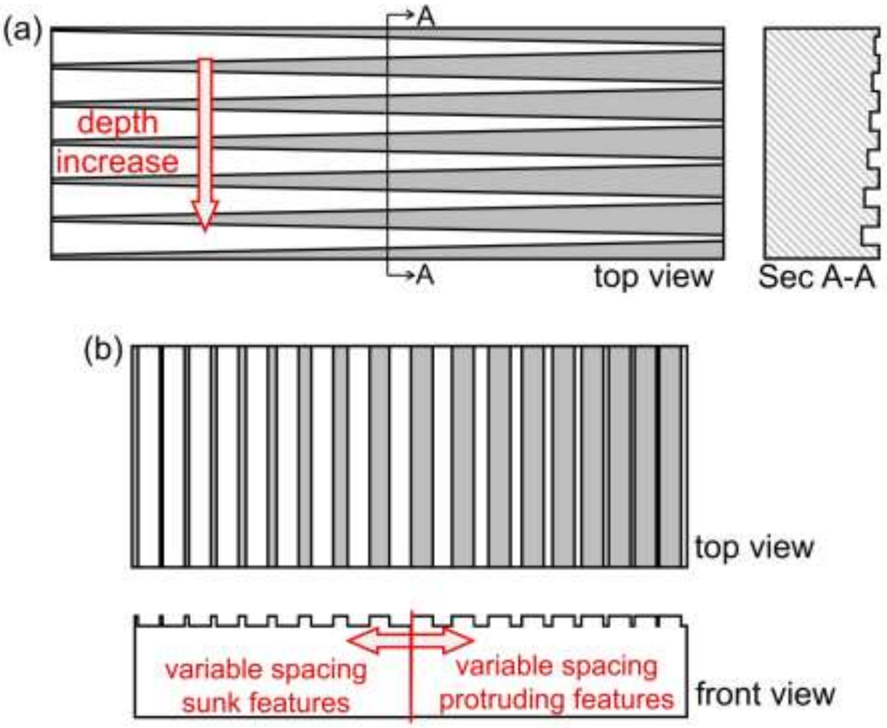

Fig. 2.1. Schematic of coupons to assess limiting feature geometry in terms of: (a) width, and (b) spacing.

Table 2.1. Process parameters for coupon builds.

Process parameter	P (W)	v (mm/s)	h (mm)	t (mm)	E_v (J/mm^3)	Remarks
Set 1	250	800	0.08	0.04	97.7	Maximum density
Set 2	300	1000	0.12	0.04	62.5	Maximum strength

The third coupon pertained to the limiting width of single tracks, which were printed in a single pass under different combinations of scanning speed (ten levels, from 200 mm/s to 2000 mm/s) and laser power (eight levels, from 50 W to 370 W). The tracks were of 3 mm length and were printed in a direction perpendicular to the scanning direction of the layer on which they were printed.

2.2.3 Artifacts for defined texture features

Square pillars (Fig. 2.2a) and rectangular channels (Fig. 2.2b) were built on top of 10 mm x 10 mm base samples. The dimensions of these features (Table 2.2) were based on information obtained from building coupons meant to determine minimum feature size (Sec.2.2.2). Pillars were built using bi-directional scanning with a hatch spacing of 0.1 mm, using a laser power and scanning speed of 300 W and 800 mm/s, respectively, with the coupon edges oriented parallel to the scanning axes. Widening the hatch spacing values (0.2 mm to 0.5 mm), the second pattern was fabricated using the same process parameters, to realize the geometry of the individual channels.

Table 2.2. Dimensions (in mm) for designed texture features on the top surface.

Square pillars	*c*	0.15, 0.20, 0.25
	p	0.10, 0.15
	z	0.04, 0.08, 0.12, 0.16
Rectangular channels	*h*	0.20, 0.25, 0.30, 0.35, 0.40, 0.45, 0.50
	z	0.04, 0.08, 0.12, 0.16, 0.20

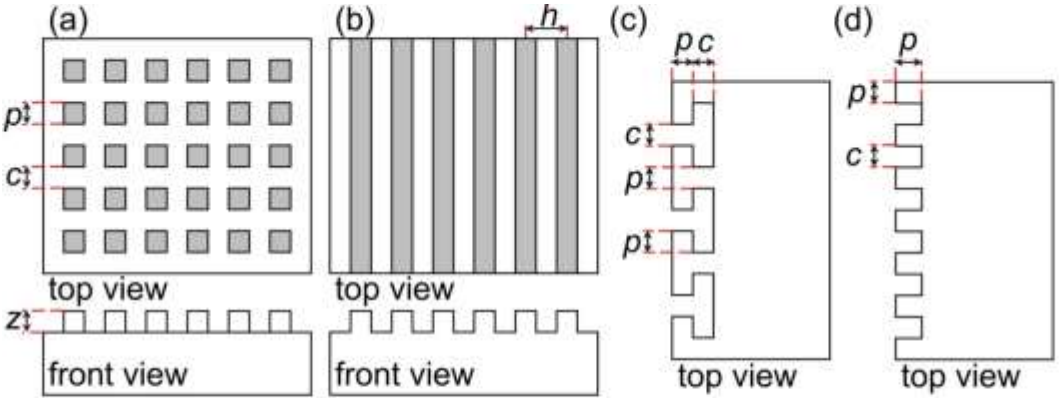

Fig. 2.2. Texturing patterns on top surface: (a) pillars, (b) channels; and on sidewall: (c) re-entrants, and (d) channels.

In addition to textures on the top surface, re-entrant features (Fig. 2.2c) and channels (Fig. 2.2d) were built on the side walls (parallel to the build direction) using the same process parameters as above, on samples of a section of 5 mm x10 mm and a height of 7 mm. The dimensions of these features were the same as that of the top surface cavities and pillars (Table 2.2).

2.2.4 Characterization

Built coupons were examined using optical and scanning electron microscopy. Roughness was measured with a stylus profilometer in terms of the *Ra* parameter, using 5 measurements on each sample. The static CA was measured optically with 5 µL distilled water droplets, using six measurements across different sample locations. Samples were elevated gradually to facilitate water droplets being picked up by the surface from the dosing syringe, rather than drop on the surface and thereby introduce measurement errors [12]. The estimation of CA entailed the Axisymmetric Drop Shape Analysis (ADSA) fitting method [13]. In light of probable temporal evolution of CA [6], measurements were undertaken at least three weeks after printing.

2.3 Results and Discussion

2.3.1 Roughness and contact angle of as-built surfaces

In view of the objective of the present work in exploring the role of additive texturing in controlling the wettability of metallic surfaces, it was imperative to first characterize and benchmark the roughness and CA of as-built surfaces for a range of SLM parameters and examine any correlations between the roughness and CA of such surfaces. To this end, top and side surfaces were investigated for a range of process parameters: power 200–300 W, scanning speed 600–1000 mm/s and hatch spacing 0.08–0.12 mm [11], and their effects were collectively interpreted in terms of the volumetric energy density E_V (Fig. 2.3a).

For about a three-fold change in E_V (41.2–157 J/mm^3) the *Ra* roughness (measured perpendicular to the scanning direction) of top surfaces manifested roughly a five-fold non-linear decrease (14.5–3.1 µm). This trend aligns with that reported in [14] and could be attributed to the combination of high laser power, low scanning speed and low hatch spacing jointly promoting a more uniform spatial distribution of a larger pool of molten material [15].

For such a large variation in *Ra* roughness, the measurement of CA indicated a variation of only 20° (in the range of 80°–100°) with no systematic trends. This is similar to the observation in [6], which dealt with the application of EDM in fabricating hydrophobic surfaces, that the CA varied over a similar range (~20°) for a five-fold increase in the *Ra* roughness. For a given surface, the CA values also exhibited significant variability (mean standard deviation of 5°) signifying the metastable nature of the states that the water droplet can exist in. Fig. 2.3a provides a visual representation of the water droplets on surfaces corresponding to extremes within the range of roughness values investigated, with CA of 90° and 93°.

Given that the equilibrium CA of a polished surface of 316L stainless steel is reportedly 75° [16] the increase in CA (80°–100°) obtained with SLM may be attributed to changes in surface topography in line with Wenzel/Cassie-Baxter models [12], and possible changes to the chemistry of these surfaces over time [17]. The increase in CA for as-built surfaces is rather modest over such a relatively large range of roughness. This implies that a further increase in CA would likely have to be obtained through defined textures that are realized in-process during SLM, which is the fundamental tenet of this paper.

In contrast to the top surfaces that displayed a wide range in roughness and a declining trend with E_V (Fig. 2.3a), the roughness of side surfaces (Fig. 2.3b) was relatively stationary and corresponded to the higher end (10–13 μm *Ra*). An examination of the side surfaces to decipher this behaviour showed a conspicuous presence of bonded metal particles that are either only partially melted or unmelted (Fig. 2.4), the incidence of which appears to have had a dominating influence on the surface roughness. The exposure of powder particles adjacent to the edges to thermal energy insufficient for complete melting combined with short solidification time could result in their formation [18]. Such features did not but influence the CA measurements, with values being on the same order (80°–100°) as those on the top surfaces; for instance, Fig. 2.3b shows droplet geometry for either end of roughness with CA of 85° and 92°. Notwithstanding the fact that the CA of as-built surfaces was not markedly influenced by these globular microstructures, considering their resemblance to hierarchical features (albeit of a larger scale) on biological surfaces such as lotus leaves that significantly promote hydrophobicity [19], their role will be revisited later in this paper in the context of textured surfaces.

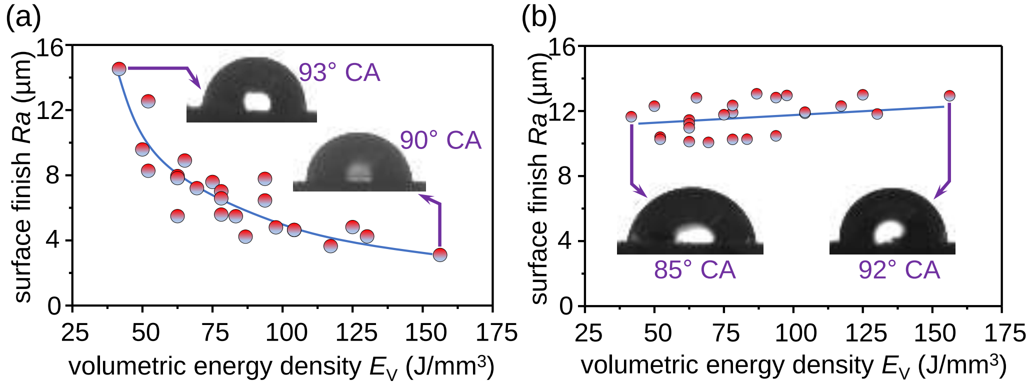

Fig. 2.3. The roughness of: (a) top, and (b) side surfaces; insets show droplet shapes and CA for extreme values.

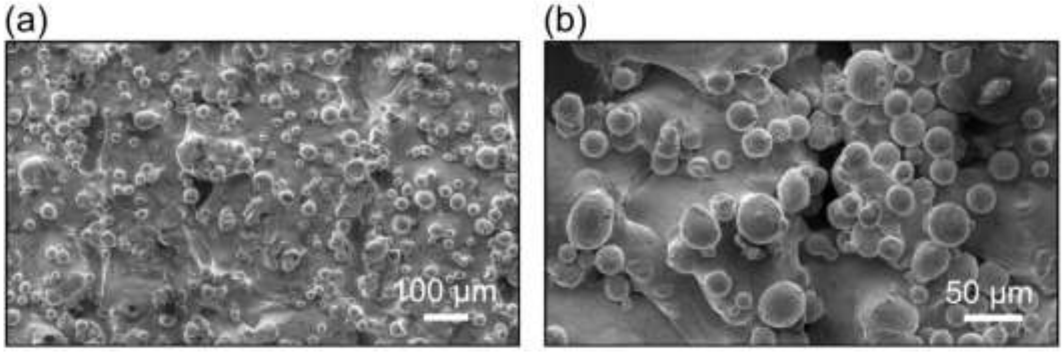

Fig. 2.4. Topography of side surfaces at two length scales.

2.3.2 Assessment of limiting feature geometry

This subsection presents results obtained from printing the four artifacts (Sec.2.2.2) designed to gather information on the limiting feature geometry. The first artifact (Fig. 2.1a) focused on the evaluation of the minimum width for protruding and sunk features by printing trapezoids. The trapezoid sides changed linearly from 0.01 mm to 0.60 mm over a length of 45 mm. Fig. 2.5a depicts a region on this artifact which shows the limiting feature width at two magnifications for protruding features. The trapezoids were not adequately deposited at an approximate distance of 5 mm along the coupon length from the smaller parallel side of the trapezoid (0.01 mm). This corresponds to a minimum width of 0.09 mm by design, however, the width at this location was measured to be 0.13 mm, which may be reconciled in terms of the effective spot size of the laser and the programmed beam offset. Fig. 2.5a further makes it evident that the minimum width is largely independent of the feature height over the range investigated (one to twelve layer thickness of 0.04 mm each).

Relative to the protruding features above, locations at which the sunken trapezoids were not adequately resolved entailed a larger variation (Fig. 2.5b). Well defined open channels could be observed at a distance of ~10 mm from the edge, which corresponds to a width of 0.14 mm as per the design. In line with the protruding features, the actual width at this location was somewhat lower and was measured to be 0.10 mm, on account of the material closing in on the sunk features. Characterization of the first artifact thus indicated the limiting feature widths to be 0.13 mm and 0.10 mm for protruding and sunk features, respectively.

Fig. 2.6a and Fig. 2.6b portray printed versions of the second artifact that was designed (Fig. 2.1b) to assess the minimum spacing between protruding and sunk features. The minimum spacing controls such indices as the feature density and area fraction that have been found to be decisive in tribological [20, 21] and surface wetting [19] applications. For a fixed protruding feature width of 0.4 mm, the minimum achievable spacing was measured to be 0.11 mm, which was lower than the design spacing of 0.15 mm (Fig. 2.6a), as expected. Likewise, the corresponding spacing for sunk features (Fig. 2.6b) was measured to be 0.13 mm, which is higher than the design value (0.09 mm). It is interesting to note that the minimum spacing values (0.13 and 0.09 mm) are similar to the corresponding minimum feature widths (Fig. 2.5).

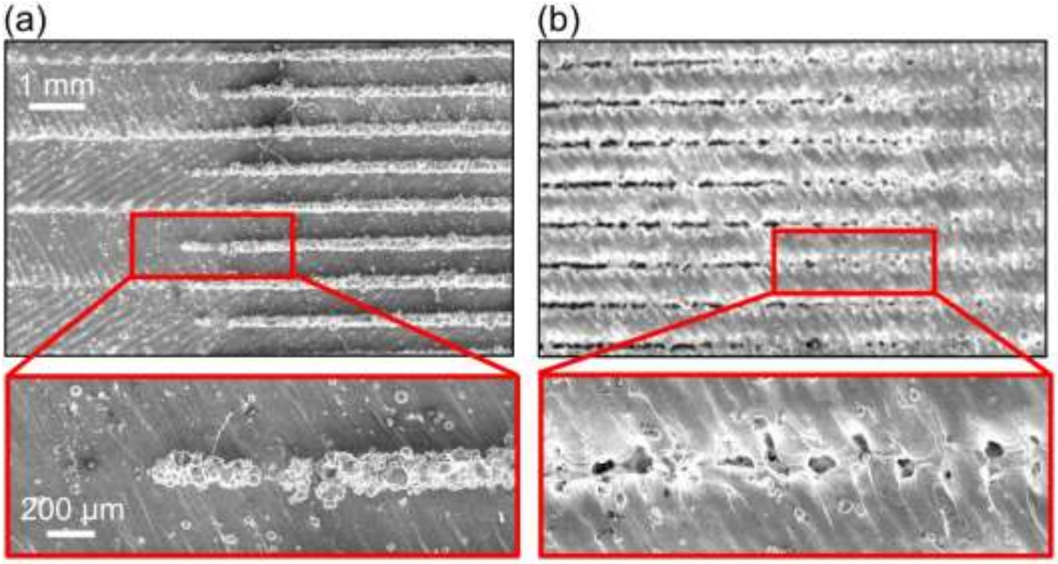

Fig. 2.5. Minimum width for: (a) protruding, and (b) sunk features.

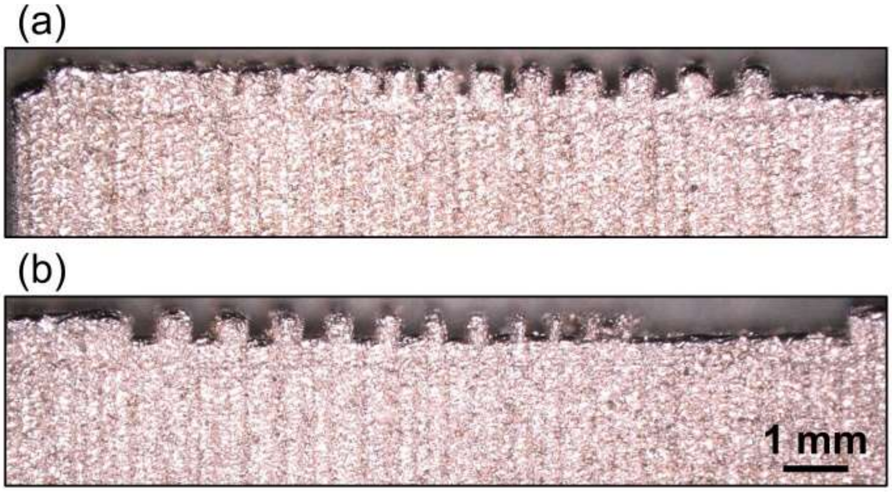

Fig. 2.6. Minimum spacing for: (a) protruding, and (b) sunk features.

For both artifacts discussed above, the measured minimum feature dimensions were independent of the SLM process parameters employed with reference to the maximum strength and density (

Table 2.1). To further expand on the process parameter domain, single tracks were printed over a wide range of laser power (50–370 W) and scanning speeds (200–2000 mm/s), and the width of such tracks was measured at different locations along the track. Fig. 2.7 shows the average track width, with the effects of the laser power and scanning speed consolidated in terms of the linear energy density E_L. The figure shows the track width distribution to be rather skewed between 0.1 mm and 0.15 mm. This is quite in alignment with the findings of feature dimensions obtained from the three artifacts already discussed. Examination of the fabricated tracks indicated noticeable balling at a low energy density (Fig. 2.8a). this phenomenon is but not quite suitable to print robust structured surfaces due to its inherent randomness. Fig. 2.8b and c show tracks that correspond to the lower (0.1 mm) and higher (0.2 mm) ends of track width. Fig. 2.8d underscores the utilization of an appropriate combination of laser power and scanning speed towards obtaining consistent tracks under stable melting, which is an additional consideration along with the minimum width, for robust texturing.

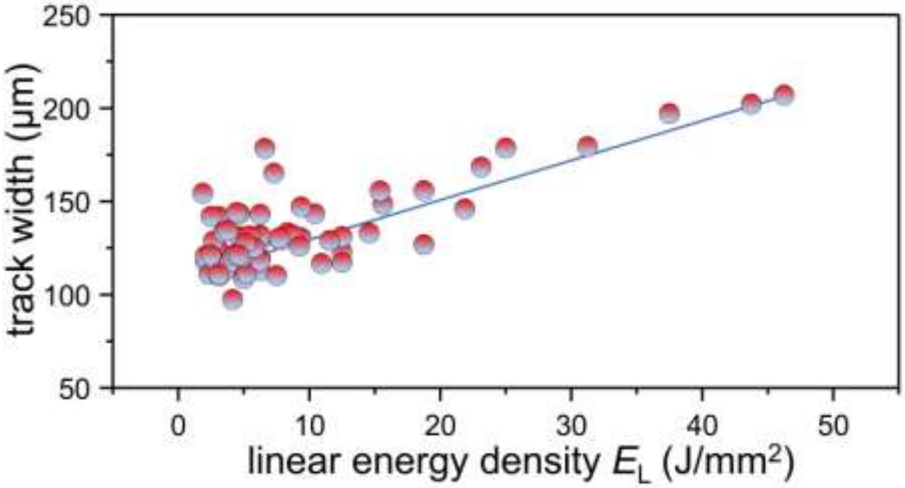

Fig. 2.7. Single track width as a function of linear energy density.

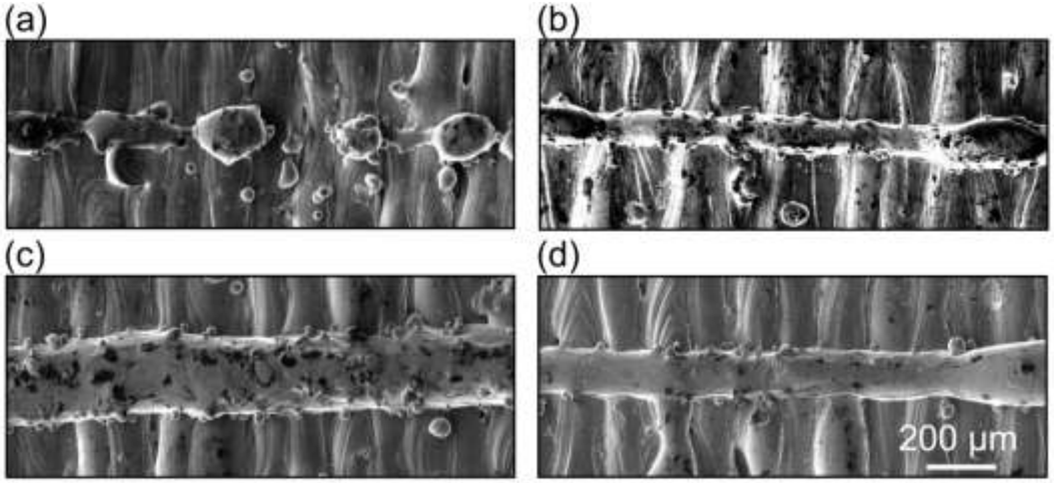

Fig. 2.8. Single tracks obtained under different combinations of laser power and scanning speed: (a) 50 W, 400 mm/s, (b) 200 W, 1200 mm/s, (c) 370 W, 200 mm/s, and (d) 300 W, 800 mm/s.

2.3.3 Contact angle of additively textured surfaces

With a focus on controlling surface wettability, additively textured patterns were investigated on both the top and side surfaces, as indicated in Sec. 2.3.2. The top surface entailed square pillars and rectangular channels, and the side surface involved re-entrant and rectangular channels (Fig. 2.2). The dimensions of these textured features (Table 2.2) were set on the basis of the knowledge obtained from building and characterizing artifacts that were designed to inform limiting feature sizes (Fig. 2.1).

On the top surface, the first pattern referred to an array of square pillars with side lengths of 0.10 mm and 0.15 mm, over a range of spacing (0.15–0.25 mm) and height (0.04–0.16 mm). Fig. 2.9a and 9b show pillars with side lengths of 0.10 mm and 0.15 mm, respectively; they were of the same spacing (0.25 mm) and height (0.12 mm). The pillars can be seen to comprise largely circular sections and rounded tops, rather than the intended square cross-sections and flat tops, owing to surface tension effects. For a pillar side length of 0.1 mm, the pattern array can be observed to be fairly irregular with several evident instances of local build failures (Fig. 2.9a). The occurrence of such could be reduced significantly by increasing the pillar side length to 0.15 mm (Fig. 2.9b). Fig. 2.9 further shows the corresponding droplet shapes that indicate the respective CA to be 137° and 125°, which is a significant increase over that of as-built surfaces that were on the order of 80°–100° (Fig. 2.3). It is further interesting to note that the obtained CA are comparable to those measured on pillar arrays of a similar geometry that were micro-milled from polymethyl methacrylate [22].

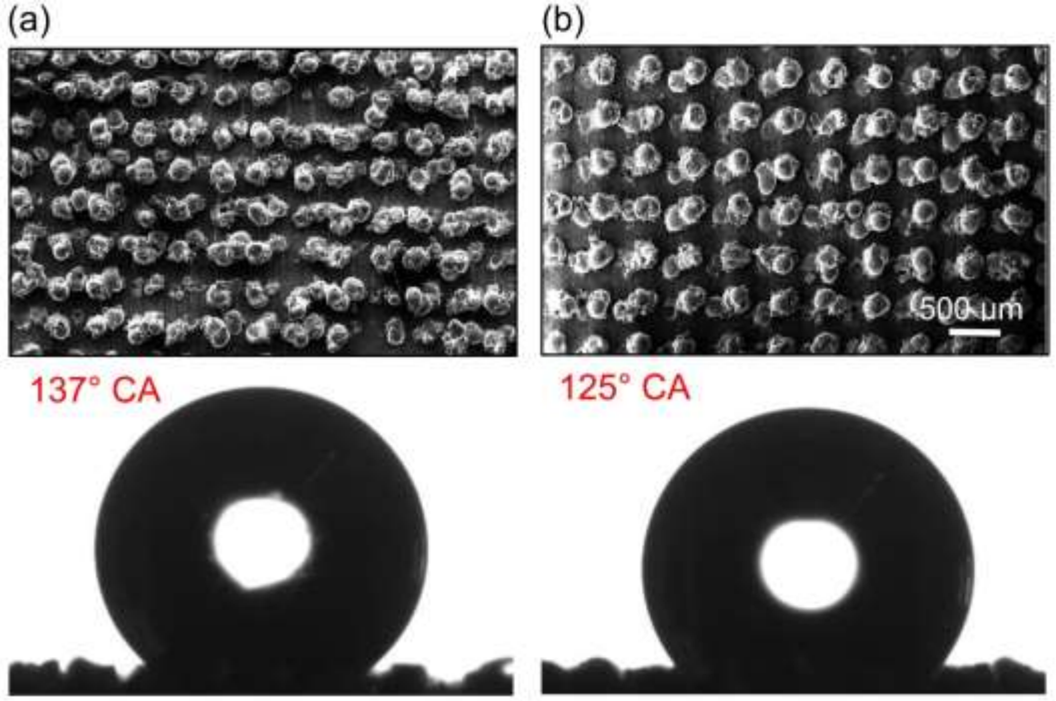

Fig. 2.9. Pillar array surfaces with side lengths of:
(a) 0.1 mm, and (b) 0.15 mm, and the associated droplets.

Wetting of rough surfaces has classically been viewed in terms of models due to Wenzel and Cassie-Baxter [12, 23]. The Wenzel model describes the homogenous wetting regime wherein the fluid intrudes into the surface interstices, with the apparent or static CA of a rough surface Θ_W related to the Young or equilibrium contact angle Θ of an ideal surface as: $\cos \Theta_W = r \cos \Theta$, where the roughness factor r is the ratio of the actual and projected surface areas. The Cassie-Baxter model extends the concept further to partial wetting of heterogeneous surfaces such as feathers and lotus leaves, wherein the surface is deemed to be a composite solid-liquid-air interface, with surface troughs constituting air pockets that support droplets on surface peaks. The corresponding static contact angle Θ_{CB} is obtained as $[f \cos \Theta + (f - 1)]$ where f is the solid area fraction. For a pillar array, f can be calculated [22] as $[p^2/(p+c)^2]$, where the parameters p and c are the pillar side length and spacing, respectively (Fig. 2.2a).

The decrease in CA from 137° to 125° with an increase in pillar side length from 0.10 mm to 0.15 at a constant spacing (Fig. 2.9) is in qualitative agreement with the Cassie-Baxter model above. Likewise, the CA should exhibit an increase with higher spacing parameter c, which was consistent with measurements (Fig. 2.10a). The CA did exhibit a relatively significant change (Fig. 2.10b) with the pillar height over the range investigated (one to four layers: 0.04 to 0.16 mm). The higher CA associated with the pillars of a height spanning three and four layers may be attributed to the transition of the water droplets from the Wenzel to the Cassie-Baxter state. Such a transition occurs when the maximum droop of the water droplet $[2c^2/(8R)]$ between pillars (where R is the water drop radius) is more than the pillar height [24].

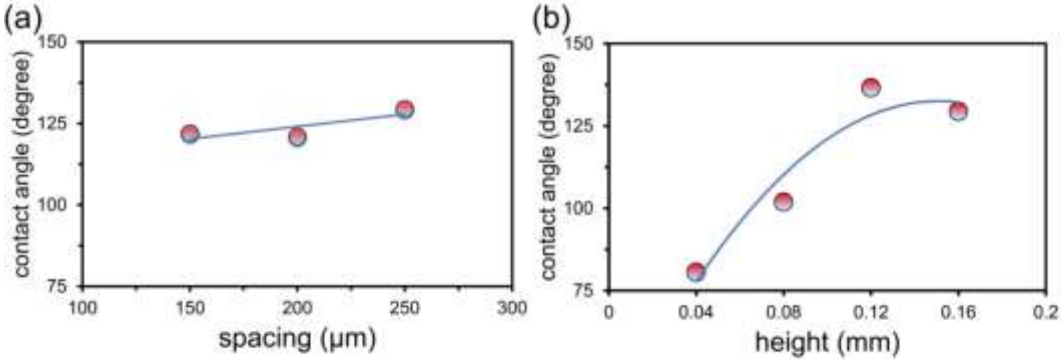

Fig. 2.10. CA for 0.1 mm side length pillars at:
(a) 0.16 mm pillar height, and (b) 0.25 mm pillar spacing.

The second texturing pattern on the top surface referred to rectangular channels spanning a range of pitch (0.2–0.5 mm) and height (0.04–0.20 mm). The channels were built by using higher values for the hatch spacing resulting in separated singletracks, with a variable width associated with the process parameters (Fig. 2.7). Fig. 2.11a and Fig. 2.11b show two channels with a pitch of 0.2 mm and 0.5 mm, and a height of 0.2 mm. The channel features were consistently of better quality, with no local build failures as in the case of micropillars (Fig. 2.9). Fig. 2.11 further shows the corresponding droplet shapes, which indicate the CA to have increased significantly from 97° to 136° for an increase in spacing by a factor of 2.5. Fig. 2.12a presents data showing an increase in CA with hatch spacing, at a fixed height of 0.2 mm. Such an increase is in qualitative agreement with the Cassie-Baxter model, and may be attributed to the change in solid area fraction, which is calculated [22] for channels as [w/h], where w is the track width and h is the hatch spacing. The average track width associated with 800 m/s scanning speed and 300 W power was approximately 0.14 mm (Fig. 2.8d).

Fig. 2.12b shows the CA to also generally increase with channel height (number of layers). Over the investigated range, the pitch can be observed to have a greater impact on the CA compared to the height. CA shown in Fig. 2.12a and b are comparable to those measured on channel arrays of similar geometry, micro-milled from polymethyl methacrylate [22]. Further investigations indicated channel patterns to exhibit wetting anisotropy, with CA values measured parallel to the channel length corresponding to a decrease of 10° to 15° relative to those measured across. This signifies a relative elongation of the droplet along the channel length, similar to that reported in the case of steel microchannels machined using wire EDM [25].

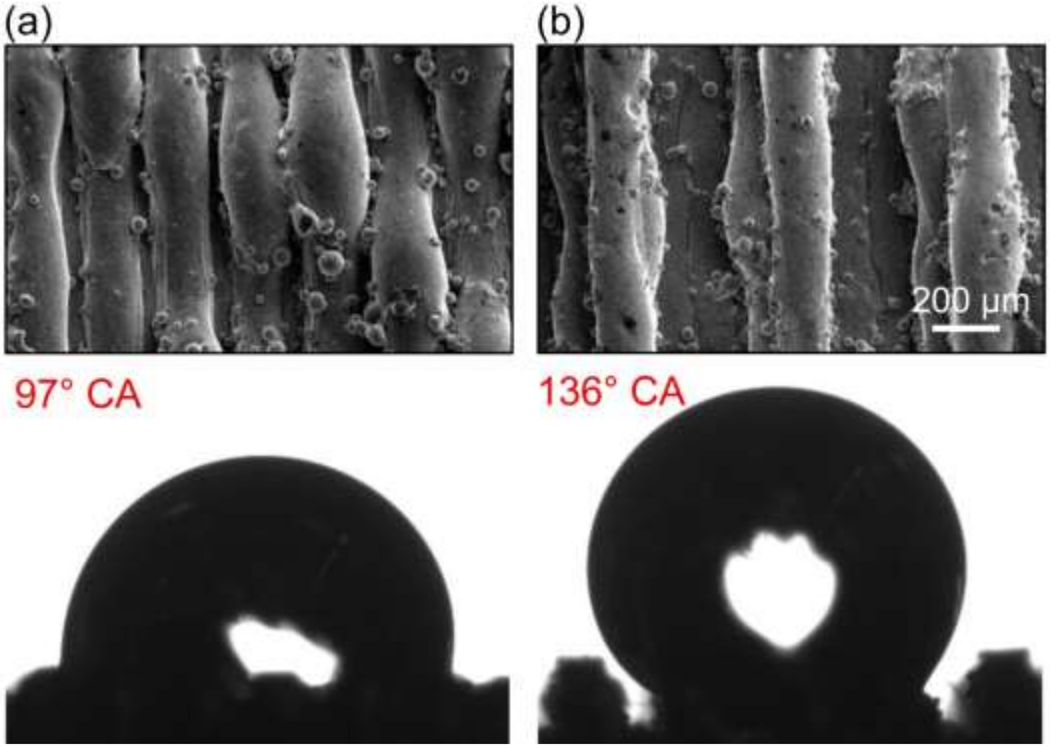

Fig. 2.11. Channels patterns and the associated CA for spacing: (a) h = 0.2 mm (b) h = 0.5 mm.

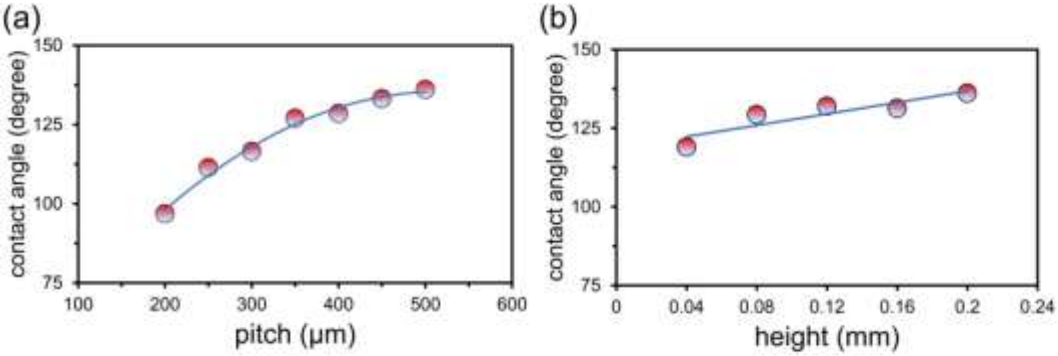

Fig. 2.12. CA for channels array at: (a) 0.2 mm height (b) 0.5 mm pitch.

The mushroom-like geometry of re-entrant channels comprises air pockets that support water droplets in the composite solid-liquid-air state, preventing them from intruding into the relief structures in between. This geometry increases the energy threshold at which the transition from Cassie-Baxter to Wenzel states occurs [26], thereby promoting hydrophobicity even in materials that are inherently hydrophilic [26], and for liquids with a surface tension lower than that of water [27]. Such structures machined using micro-wire EDM have for instance been shown to exhibit superhydrophobicity in [28]. Additive manufacturing of overhanging structures on the top surface (perpendicular to the build direction) in general necessitates gradual inclinations [29] or support structures, the provision of which is but not realistic in the current context that involves re-entrant features on the microscale. This issue was circumvented in the present work by realizing the re-entrant channels on the side surface parallel to the build direction as shown in Fig. 2.2c, in which case there are no overhanging features. Fig. 2.13 presents a proof of concept of this approach. The distortion in the printed structure relative to the intended design (Fig. 2.2c), appears to arise from the large height (7 mm) of the features along the print direction relative to the re-entrant feature dimensions (p = 100 μm and c = 200 μm). This notwithstanding, the corresponding CA was 126° (Fig. 2.13), which is a significant increase over those of as-built side surfaces that exhibited values ranging between 80° and 100° (Fig. 2.3).

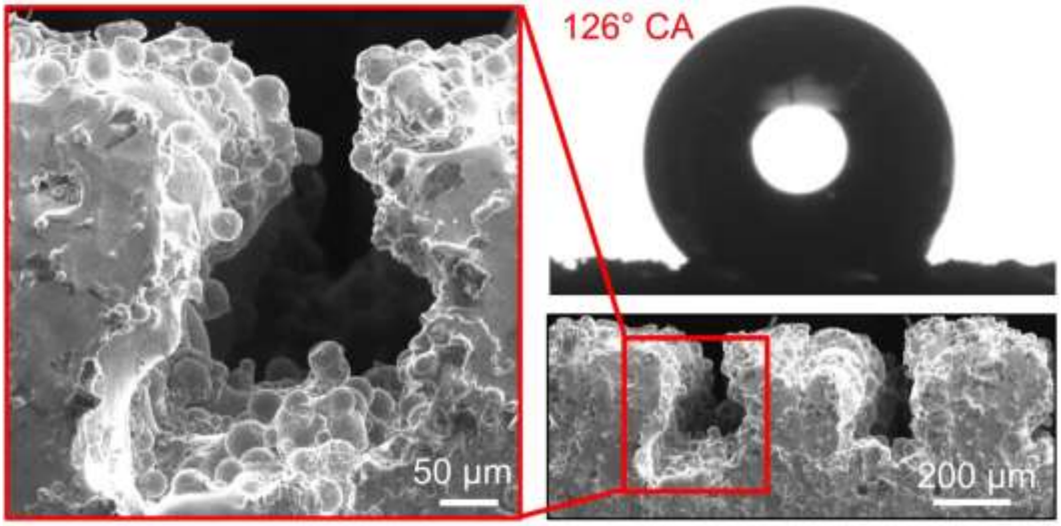

Fig. 2.13. Re-entrant structures on the side surface and the associated droplet shape.

The transition from Cassie-Baxter to Wenzel states is influenced by multiple destabilizing factors such as capillary waves, droplet condensation, surface inhomogeneities and liquid pressure. Given the scale dependency of these factors, a hierarchical texture is beneficial to realize a stable Cassie-Baxter state [19]. Partially melted metal powder particles of an approximate size of 0.03 mm adhering to the sidewalls (Fig. 2.4), which are smaller than the limiting feature dimensions of the texture, could constitute such a desired hierarchical secondary texture on top of the primary channel features and enhance the CA. To test this hypothesis, channels (p = 100 µm and c = 250 µm) were fabricated on the side surface as shown in Fig. 2.2d.

Fig. 2.14 shows the primary channels as well as the secondary texture signifying their hierarchical nature, which resulted in a CA of 141° (Fig. 2.14). It may be noted that the partially melted powder particles on the sidewall channels

(Fig. 2.14) are similar to those on the as-built side surfaces (Fig. 2.4). While the side as-built surfaces comprising partially melted powder corresponded to contact angles of just around 90° (Fig. 2.3b), such a topography when overlaid on a primary texture comprising channels yielded a contact angle of 141° (Fig. 2.15b). This implies that the mechanism behind the enhancement of hydrophobicity is indeed the hierarchical nature of the printed surface. Given the inadequacy of easy-to-measure but too simplistic a roughness parameter as *Ra* to capture the intricacies of a phenomenon as complex as wetting (Fig. 2.3) and the highlighted importance of a hierarchical structure in the context of wettability (Fig. 2.15), it is appropriate and essential to apply multi-scale surface analyses [30] to gain additional insights into the underlying mechanisms.

Fig. 2.15 shows a comparison of the topography of channels with similar dimensions on the top (Fig. 2.15a) and side surfaces (Fig. 2.15b); the increase in CA from 132° to 141° proves the hypothesis that the increase in CA can be attributed to the secondary structure pertaining to the adhered partially molten particles. Should a component necessitate it, hierarchical top surfaces may be printed by spreading metal powder of a size consistent with the application, and then tailoring the laser power intensity to fuse the particles into the built surface as opposed to melting them completely. The highest CA of 141° obtained in this work being significantly higher than that of as-built AM surfaces (80° to 100°), validates the notion of additive texturing proposed in this paper, in the context of controlled surface wetting.

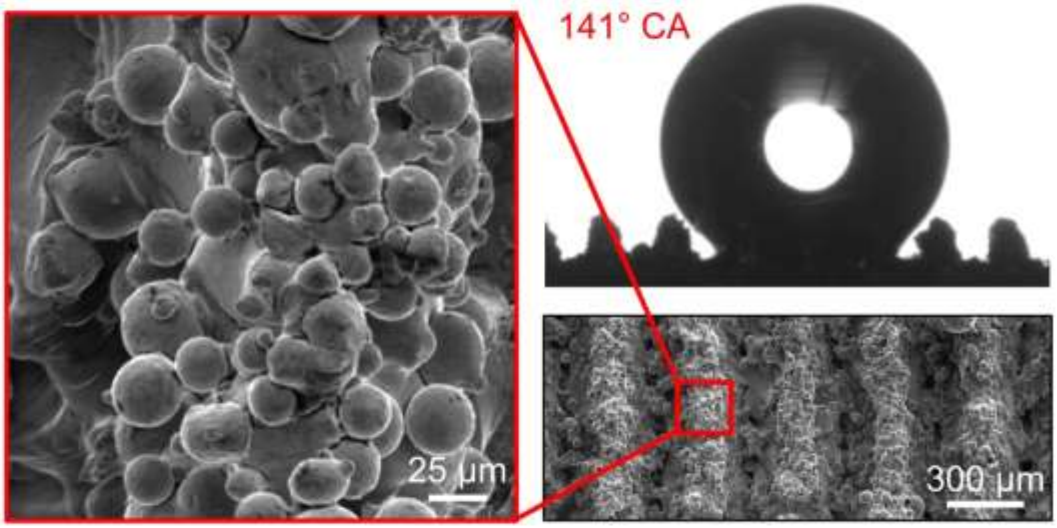

Fig. 2.14. Channels on the side surface and the corresponding droplet shape.

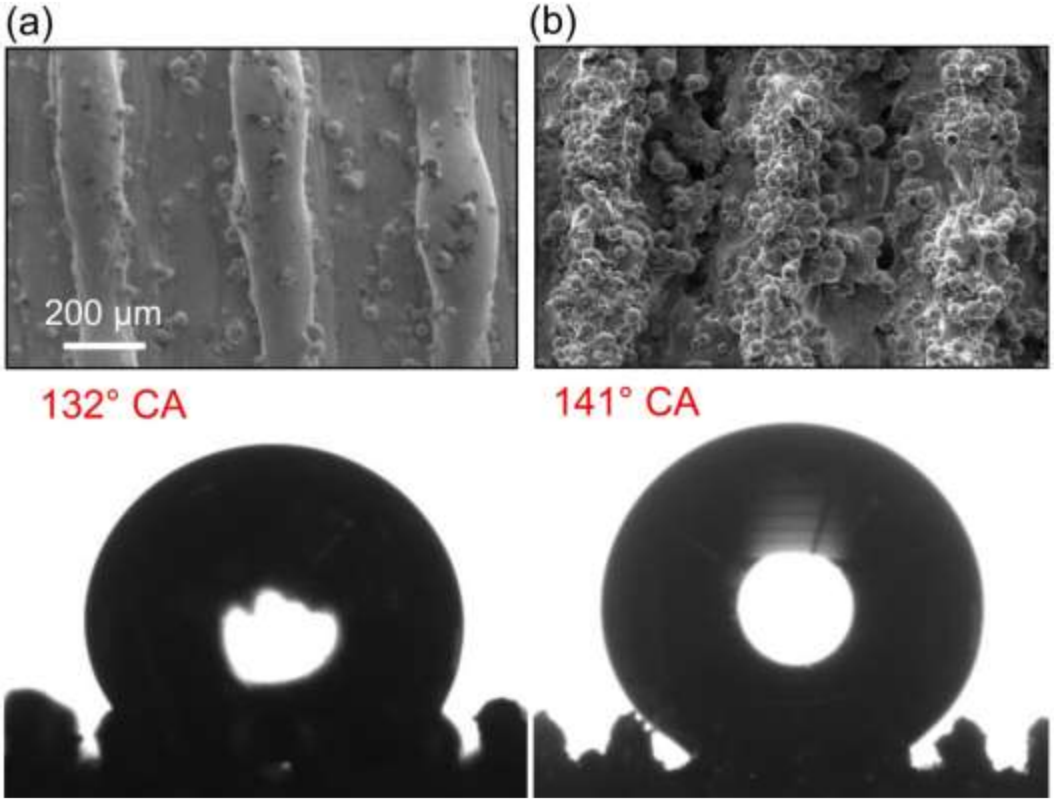

Fig. 2.15. Comparison of channels with equivalent dimensions on:
(a) top, and (b) side surfaces.

2.4 Conclusions

Intending to extend the functionality of AM components, this research presented Additive Texturing as an innovative approach for the in-process fabrication of metallic hydrophobic surfaces, with no need for additional post-processing operations. The work led to the following conclusions:

- The volumetric energy density showed a significant influence on the roughness of top surfaces in SLM. A five-fold change in roughness in terms of the *Ra* parameter but corresponded to only a minimal variation (80°–100°) in the water - CA.
- Due to partially melted powder particles adhering to the side surface, the influence of process parameters on both the surface roughness and wettability was minimal.
- Investigations indicated SLM with a continuous laser to correspond to a minimum feature width of 100–150 µm, which is equivalent to the single track width.
- For texture dimensions consistent with the limiting width, channel arrays were more reproducible and defect-free compared to pillar arrays and re-entrant channel patterns. Printing of the patterns above on the top surface indicated the channel patterns to also correspond to the highest CA of ~136°.

- Realizing channel patterns on the side surface further enhanced the CA by about 10° on account of the hierarchical dual-scale structure arising from the adherence of partially molten metal powder.
- Additively textured surfaces corresponded to a CA of up to 141° which is a significant increase over the range (80°–100°) exhibited by as-built surfaces.

This research focussed on surface wetting as an avenue to introducing the concept of Additive Texturing. The results obtained point to the significant capacity of this novel concept for likewise tailoring AM for printing functional surfaces, towards further enhancing its process capability and application potential.

Acknowledgement

This work was funded in part by the Natural Sciences and Engineering Research Council (NSERC) of Canada.

References

[1] T. DebRoy, H. Wei, J. Zuback, T. Mukherjee, J. Elmer, J. Milewski, A.M. Beese, A. Wilson-Heid, A. De, W. Zhang, Additive manufacturing of metallic components–process, structure and properties, Progress in Materials Science 92 (2018) 112–224. https://doi.org/10.1016/j.pmatsci.2017.10.001

[2] J.Y. Ho, K.K. Wong, K.C. Leong, Saturated pool boiling of FC-72 from enhanced surfaces produced by selective laser melting, International Journal of Heat and Mass Transfer 99 (2016) 107–121. https://doi.org/10.1016/j.ijheatmasstransfer.2016.03.073

[3] A. Townsend, N. Senin, L. Blunt, R. Leach, J. Taylor, Surface texture metrology for metal additive manufacturing: A review, Precision Engineering 46 (2016) 34–47. https://doi.org/10.1016/j.precisioneng.2016.06.001

[4] A.P. Malshe, S. Bapat, K.P. Rajurkar, H. Haitjema, Bio-inspired textures for functional applications, CIRP Annals 67 (2018) 627–650. https://doi.org/10.1016/j.cirp.2018.05.001

[5] Q. Ma, Z. Tong, W. Wang, G. Dong, Fabricating robust and repairable superhydrophobic surface on carbon steel by nanosecond laser texturing for corrosion protection, Applied Surface Science 455 (2018) 748–757. https://doi.org/10.1016/j.apsusc.2018.06.033

[6] C. Guo, P. Koshy, F. Coelho, P.R. Selvaganapathy, Sink electrical discharge machining of hydrophobic surfaces, CIRP Annals 68 (2019) 185–188. https://doi.org/10.1016/j.cirp.2019.04.101

[7] J.A. Wahab, M.J. Ghazali, W.M.W. Yusoff, Z. Sajuri, Enhancing material performance through laser surface texturing: a review, Transactions of the IMF 94 (2016) 193–198. https://doi.org/10.1080/00202967.2016.1191141

[8] L. Rebaioli, I. Fassi, A review on benchmark artifacts for evaluating the geometrical performance of additive manufacturing processes, The International Journal of Advanced Manufacturing Technology 93 (2017) 2571–2598. https://doi.org/10.1007/s00170-017-0570-0

[9] S. Moylan, J. Slotwinski, A. Cooke, K. Jurrens, M.A. Donmez, An additive manufacturing test artifact, Journal of Research of the National Institute of Standards and Technology 119 (2014) 429–459. http://dx.doi.org/10.6028/jres.119.017

[10] M.K. Thompson, M. Mischkot, Design of test parts to characterize micro additive manufacturing processes, Procedia CIRP 34 (2015) 223–228. https://doi.org/10.1016/j.procir.2015.07.065

[11] M. Yakout, M.A. Elbestawi, S.C. Veldhuis, Density and mechanical properties in selective laser melting of Invar 36 and stainless steel 316L, Journal of Materials Processing Technology 266 (2019) 397–420. https://doi.org/10.1016/j.jmatprotec.2018.11.006

[12] K.-Y. Law, H. Zhao, Surface wetting: Characterization, contact angle, and fundamentals, Springer, Switzerland, 2016. https://doi.org/10.1007/978-3-319-25214-8

[13] Z.N. Xu, An algorithm for selecting the most accurate protocol for contact angle measurement by drop shape analysis, Review of Scientific Instruments 85 (2014) 125107. https://doi.org/10.1063/1.4903198

[14] D. Wang, Y. Liu, Y. Yang, D. Xiao, Theoretical and experimental study on surface roughness of 316L stainless steel metal parts obtained through selective laser melting, Rapid Prototyping Journal 22 (2016) 706–716. http://dx.doi.org/10.1108/RPJ-06-2015-0078

[15] S.J. Foster, K. Carver, R.B. Dinwiddie, F. List, K.A. Unocic, A. Chaudhary, S.S. Babu, Process-defect-structure-property correlations during laser powder bed fusion of alloy 718: Role of in situ and ex situ characterizations, Metallurgical and Materials Transactions A 49 (2018) 5775–5798. https://doi.org/10.1007/s11661-018-4870-2

[16] D. Kam, S. Bhattacharya, J. Mazumder, Control of the wetting properties of an AISI 316L stainless steel surface by femtosecond laser-induced surface modification, Journal of micromechanics and microengineering 22 (2012) 105019. http://stacks.iop.org/JMM/22/105019

[17] J. Long, M. Zhong, H. Zhang, P. Fan, Superhydrophilicity to superhydrophobicity transition of picosecond laser microstructured aluminum in ambient air, Journal of Colloid and Interface Science 441 (2015) 1–9. https://doi.org/10.1016/j.jcis.2014.11.015

[18] T. Yang, T. Liu, W. Liao, E. MacDonald, H. Wei, X. Chen, L. Jiang, The influence of process parameters on vertical surface roughness of the AlSi10Mg parts fabricated by selective laser melting, Journal of Materials Processing Technology 266 (2019) 26–36. https://doi.org/10.1016/j.jmatprotec.2018.10.015

[19] B. Bhushan, Y.C. Jung, Natural and biomimetic artificial surfaces for superhydrophobicity, self-cleaning, low adhesion, and drag reduction, Progress in Materials Science 56 (2011) 1–108. https://doi.org/10.1016/j.pmatsci.2010.04.003

[20] T. Ibatan, M.S. Uddin, M.A.K. Chowdhury, Recent development on surface texturing in enhancing tribological performance of bearing sliders, Surface and Coatings Technology 272 (2015) 102–120. https://doi.org/10.1016/j.surfcoat.2015.04.017

[21] A.F.S. Baharin, M.J. Ghazali, J.A. Wahab, Laser surface texturing and its contribution to friction and wear reduction: A brief review, Industrial Lubrication and Tribology (2016) 57–66. http://dx.doi.org/10.1108/ILT-05-2015-0067

[22] Z. Shi, X. Zhang, Contact angle hysteresis analysis on superhydrophobic surface based on the design of channel and pillar models, Materials & Design 131 (2017) 323–333. https://doi.org/10.1016/j.matdes.2017.06.008

[23] M.A. Nilsson, R.J. Daniello, J.P. Rothstein, A novel and inexpensive technique for creating superhydrophobic surfaces using Teflon and sandpaper, Journal of Physics D: Applied Physics 43 (2010) 045301. http://stacks.iop.org/JPhysD/43/045301

[24] Y.C. Jung, B. Bhushan, Wetting transition of water droplets on superhydrophobic patterned surfaces, Scripta Materialia 57 (2007) 1057–1060. https://doi.org/10.1016/j.scriptamat.2007.09.004

[25] W.-G. Bae, D. Kim, K.Y. Song, H.E. Jeong, C.N. Chu, Engineering stainless steel surface via wire electrical discharge machining for controlling the wettability, Surface and Coatings Technology 275 (2015) 316–323. https://doi.org/10.1016/j.surfcoat.2015.04.047

[26] G. Whyman, E. Bormashenko, How to make the Cassie wetting state stable?, Langmuir 27 (2011) 8171–8176. https://doi.org/10.1021/la2011869

[27] R. Dufour, G. Perry, M. Harnois, Y. Coffinier, V. Thomy, V. Senez, R. Boukherroub, From micro to nano reentrant structures: Hysteresis on superomniphobic surfaces, Colloid and Polymer Science 291 (2013) 409–415. https://doi.org/10.1007/s00396-012-2750-7

[28] P.B. Weisensee, E.J. Torrealba, M. Raleigh, A.M. Jacobi, W.P. King, Hydrophobic and oleophobic re-entrant steel microstructures fabricated using micro electrical discharge machining, Journal of Micromechanics and Microengineering 24 (2014) 095020. http://dx.doi.org/10.1088/0960-1317/24/9/095020

[29] D. Wang, S. Mai, D. Xiao, Y. Yang, Surface quality of the curved overhanging structure manufactured from 316-L stainless steel by SLM, The International Journal of Advanced Manufacturing Technology 86 (2016) 781–792. https://doi.org/10.1007/s00170-015-8216-6

[30] C.A. Brown, H.N. Hansen, X.J. Jiang, F. Blateyron, J. Berglund, N. Senin, T. Bartkowiak, B. Dixon, G. Le Goïc, Y. Quinsat, W.J. Stemp, M.K. Thompson, P.S. Ungar, E.H. Zahouani, Multiscale analyses and characterizations of surface topographies, CIRP Annals 67 (2018) 839–862. https://doi.org/10.1016/j.cirp.2018.06.001

Chapter 3

Dry Sliding Performance of Additively Structured Metallic surfaces

Complete Citation:

S. Mekhiel, Philip Koshy, M.A., Elbestawi (2021). Dry sliding performance of additively structured metallic surfaces. Submitted to *Additive Manufacturing*.

Relative Contributions:

S. Mekhiel:	Conceptualization, Methodology, Experimental work, Investigation, Writing – original draft preparation, Writing – review & editing.
Philip Koshy:	Supervision, Conceptualization, Methodology, Investigation, Writing – review & editing.
M. A. Elbestawi:	Supervision, Conceptualization, Methodology, Writing – review & editing.

Abstract

The capabilities of additive manufacturing (AM) technologies to realize a custom component with sophisticated geometry are insufficient to break down the prototyping exclusivity barrier to the realm of functional parts fabrication. Therefore, to enhance AM part functionality, the tribological response in terms of the Coefficient of Friction (CoF) and specific wear rate of the AM surfaces under dry sliding conditions is explored. First, the present work highlights the hardness and tribological response superiority of AM surfaces over the cold-rolled surface. Then, the surface hardness and tribological response independence on the various AM process parameters and successive layer orientations are demonstrated. Next, the concept of surface texturing pertaining to circular dimples and linear grooves is successfully utilized to reduce the textured surfaces' CoF and specific wear rate. Furthermore, various texture modifications are explored, such as groove orientation with respect to sliding direction, X-shaped and V-shaped grooves. Lastly, the concept of tailoring the tribological behavior via texturing is validated by achieving up to 60% and 80% reduction of the CoF and the specific wear rate compared to the non-textured surfaces.

Keywords: Additive Manufacturing, Coefficient of friction, Dry sliding, Selective Laser Melting, Surface Texturing, Tribology, Wear rate.

3.1 Introduction

For decades, intensified research has been conducted to understand and improve the tribological performance of functional surfaces. Surface finish improvement via grinding followed by lapping or superfinishing has been, for a long time, the most plausible approach to enhance the tribological response of a surface. Yet, a substantial body of tribology-related research has highlighted the significance of surface texturing for controlling the Coefficient of Friction (CoF) and wear rate [1]. Furthermore, the creation of specific patterns of micro-features on a surface has exhibited, under dry, boundary, mixed, and full film lubrication conditions, superior tribological performance [2]. Such a concept has been utilized successfully and repeatedly to increase the life of biomedical implants like the prosthetic hip implant [3] or to suit multiple mechanical applications such as cylinder liners, cutting tools, journal bearing, and mechanical seals [4].

Among numerous surface texturing techniques such as lithography, reactive ion etching, electrochemical machining, micro-casting, micro-milling, and micro-EDM [1, 4], laser surface texturing has been predominantly acknowledged for its relative speed and precision [5]. However, for an effective texturing process, a preceding surface finishing step is crucial to reach a surface quality threshold at which the texturing feature size and the roughness value are no longer comparable. Additionally, evaporation of material with the pulsed laser has often induced bulged rims [6] and rough feature bottoms, bidding even more additional steps to smoothen the surface [7]. Other techniques like the deposition of patterned coatings or selective polymeric or ceramic film growth induce texturing patterns via adding materials to the targeted surface. Still, these techniques are restricted by thickness limitations and inferior strength, and are inadequate to withstand the significant stresses generated during the sliding process [2].

Recently, Additive manufacturing (AM) technologies, in which components are built bottom-up by compiling predefined progressive thin layers of the material, have been the focus of engineers and scientists, and represent a potential candidate for fabricating engineered surfaces without any thickness or strength limitations and in a single step. AM techniques have successfully disposed of tooling access and geometry constraints associated with the conventional subtractive manufacturing techniques. By virtue of overturning such limitations, AM has attained the capability to realize parts with intricate features and sophisticated geometries, minimizing the number of constituent parts in an assembly and evolving design perspectives from manufacturability to functionality. Consequently, AM has granted a significant cutback in time and cost correlated with design, tooling, and assembly processes [8].

In the early stage of AM research, there have been a few attempts to optimize the building process parameters, such as linear energy density, to enhance the tribological behavior of AM surfaces [9]. Yet, despite having higher strength, AM parts exhibited inferior tribological response, attributed to high porosity relative to Conventionally Processed (CP) parts [10]. Recent advances in AM have enabled the fabrication of parts with a relative density of over 99.8% of the bulk materials' densities to successfully eliminate the porosity problem [11]. Consequently, CoF and wear rate of AM surfaces have been comparable to those of CP [12] or even lower for some processes like Hot Isostatic Pressing (HIP), forging, hot forming, and casting [13-15]. On the other hand, CoF and wear rate dependency on processing parameters, such as laser power, scanning, and building direction relative to the base plate, have been investigated with no conclusive results [16-19].

There have been other efforts to enhance the tribological response utilizing metal matrix composites: for example, TiB_2 reinforcement particulates improved the wear resistance of Ti_6Al_4V [20]. Notwithstanding, feedstock preparation for such composites usually requires an additional powder mixture process. Additionally, a superior tribological response has been induced by printing additional layers of a material with higher wear resistance, like adding extra layers of Ti_6Al_4V on top of 316L [21]. Using the same concept, adding C enriched layers of TiC on Ti_6Al_4V [22] or WC on MS1 [23] has acted as a solid lubricant reducing the wear rates dramatically. Furthermore, an additional layer of protruding discs and rings array of copper has been deposited on a 304 SS surface, causing a noticeable friction reduction due to the addition of the softer material [24]. Another approach that has been investigated is utilizing an extra step of surface modification such as carburization [15], plasma oxidation [25], and Ultrasonic Nanocrystal Surface Modification (UNSM) [26]. However, the mentioned techniques have been inapplicable to complex geometries, despite their tribological performance improvement.

In-process texturing has offered a potential candidate to improve the surface tribological response, excluding any additional steps regardless of the geometrical complexity. Furthermore, the concept of additive texturing has been proven to improve hydrophobicity [27] and heat transfer behavior [28] of textured surfaces. Yet, to this moment, only one paper has been published on the in-process tribology-related texturing. Such study initially compared two texturing densities then investigated the impact of changing texturing shapes and their combined effect with plasma nitriding in dry and Simulated Body Fluid (SBF) conditions [29]. Importantly, apparent porosity of the tested surfaces was observed, implying lower relative density. Furthermore, the AM process parameters have been excluded as well as the texturing feature dimensions. Noticeably for dry sliding, texturing area density and feature dimensions have been acknowledged as the most prominent texturing design parameters [1, 5].

It is evident that the potential of in-process texturing to enhance the tribological response of the AM metallic parts is yet to be explored. The present study will focus on improving the tribological characteristics of 316L AM surfaces under dry sliding conditions. The first phase of this research will be dedicated to investigating various sets of process parameters and different successive layer orientations for the solid samples. Following, the texturing concept will be explored via two patterns (circular dimples and linear grooves), emphasizing the impact of changing the main texturing parameters such as feature width and texturing areal density. Finally, the effect of some further modifications, such as groove orientation, will be studied. The efficacy of the surface texturing will be demonstrated by a 60% reduction of the CoF and a lower specific wear rate reaching 20% of that of the solid AM parts.

3.2 Experimental

3.2.1 Material and process parameters

Coupons were printed using an EOS M280 Selective Laser Melting (SLM) machine with a 400 W continuous ytterbium fiber laser in a nitrogen environment using gas atomized AISI 316L stainless steel feedstock of 15–45 µm particle size. Cylindrical coupons of 30 mm diameter and 8 mm height were built in a direction normal to the plane of the base plate, maintaining a layer thickness of 0.04 mm. The maximum available stripe width of 100 mm was used, and the samples were positioned so as to avoid stripe overlap. Printing entailed scanning strategies with different successive layer orientations (Fig. 3.1.), which was found in [30] to influence printed components' strength and fatigue resistance. Three sets of process parameters referring to a recommendation from the machine tool manufacturer and those reported [31] to maximize density and strength were considered (Table 3.1.; P, v, h, and E_V are the laser power, scanning speed, hatch spacing, and volumetric energy density respectively). Wire electrical discharge machining (WEDM) was used to separate coupons off the baseplate.

Table 3.1. SLM process parameters.

Process parameters	P (W)	v (mm/s)	h (mm)	E_V (J/mm^3)	Notes
Set 1	285	960	0.11	67.47	From manufacturer
Set 2	250	800	0.08	97.7	Maximum density
Set 3	300	1000	0.12	62.5	Maximum strength

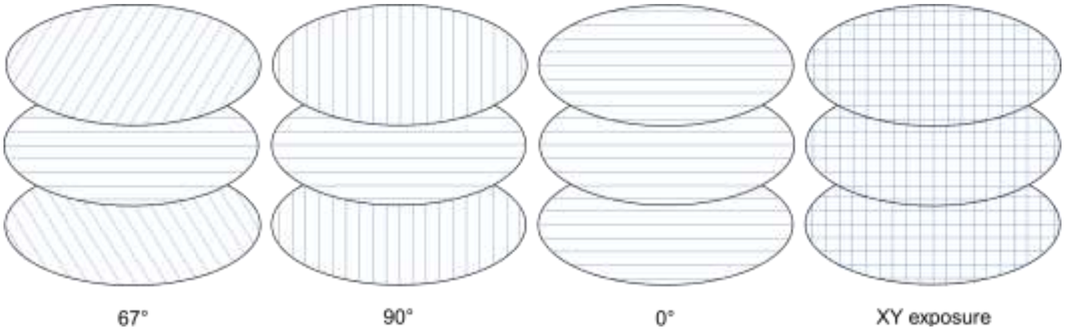

Fig. 3.1. Successive layer orientations.

3.2.2 Texture geometry

Tested textures involved sunk features in the interest of sustaining surface tractions, in contrast to non-load-bearing protruding features that facilitate such attributes as hydrophobicity [27] and boiling heat transfer [28]. Based on guidelines proposed in [32], limiting cavity dimensions were determined using artifacts comprising an array of through holes and grooves with decreasing diameter and width. The effect of feature width and areal density was investigated by fabricating and testing coupons with hole/groove texture. Hole diameter ranged from 750 µm to 150 µm, and rectangular grooves (of 4 mm depth) were of width between 600 µm and 200 µm. The hole and groove features were designed to correspond to areal densities of 5%, 20%, and 44% at the sliding wear test orbit (Fig. 3.2.). For the groove pattern referring to 20% density and 400 µm width, orientations ranging from 15° to 60° relative to the sliding direction were tested; V-shaped and X-shaped groove patterns of 30° orientation were also investigated (Fig. 3.3.).

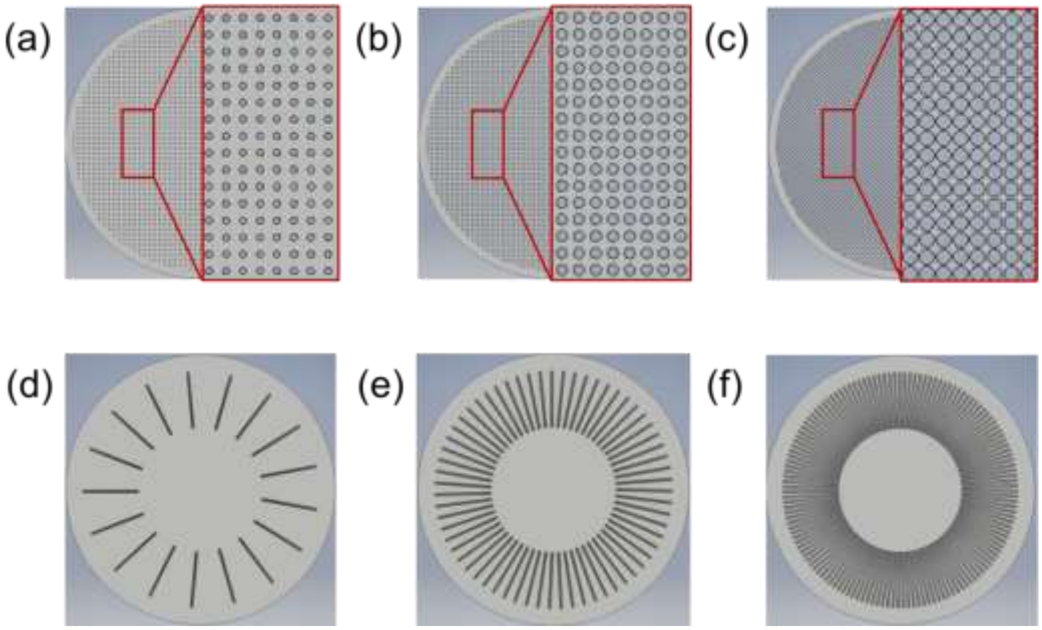

Fig. 3.2. Coupons with hole features with (a) 5% (b) 20% (c) 44% areal density, and grooved samples with (d) 5% (e) 20% (f) 44% density.

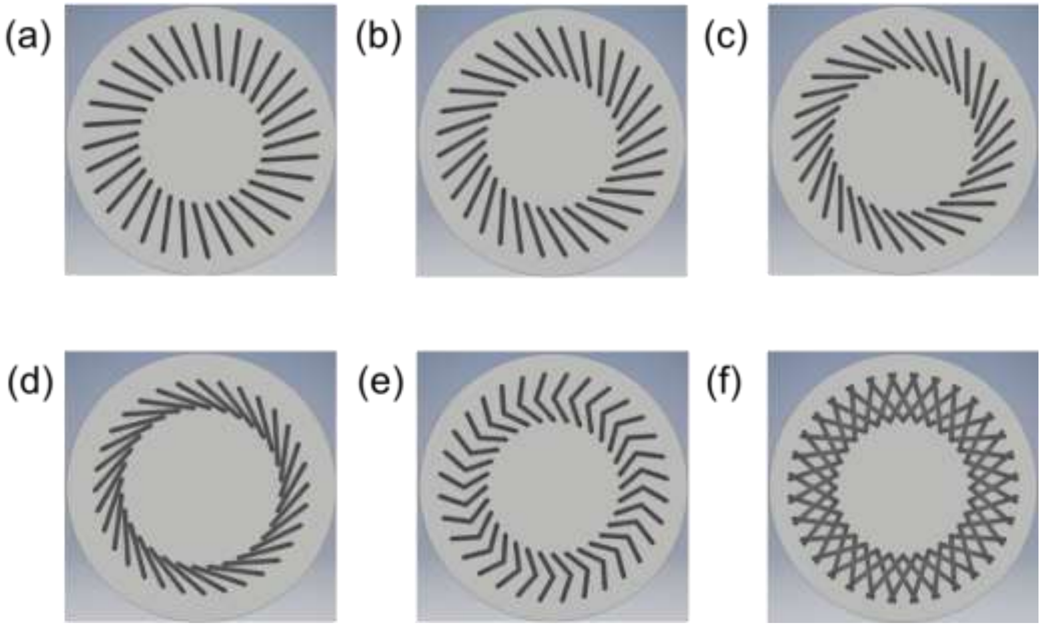

Fig. 3.3. Straight groove patterns with orientations of: (a) 15°, (b) 30°, (c) 45°, (d) 60°, and (e) V-shaped and (f) X-shaped grooves.

3.2.3 Tribological characterization

Coupon density was measured using the Archimedes method [33] to be 98% or higher. Surface roughness was measured using a stylus profilometer, and surface micro-hardness was evaluated on polished surfaces with a 200 g load. A standard tribometer (Anton Paar® TRB^3) was used to perform dry sliding tests using a rotating ball-on-disk configuration (Fig. 3.4.) on printed surfaces that were finish-ground to a *Ra* roughness of less than 0.8 µm, as per the ASTM G99 standard [34]. Sliding tests were conducted on circular sections perpendicular to the build direction that referred to the highest microhardness and the best tribological performance [17]. The counterface was a 6 mm diameter Al_2O_3 ball with a hardness of 1700 HV. Testing involved a 10 N load and a linear sliding speed of

0.1 m/s at diameters of 10, 15, 20, and 25 mm (only 20 mm for groove-based textures), at a temperature of 25 °C and a humidity of 18%. Wear rate was determined by measuring mass difference using a scale with a resolution of 0.1 mg. Scanning electron microscopy was used to examine the built textures and wear scars.

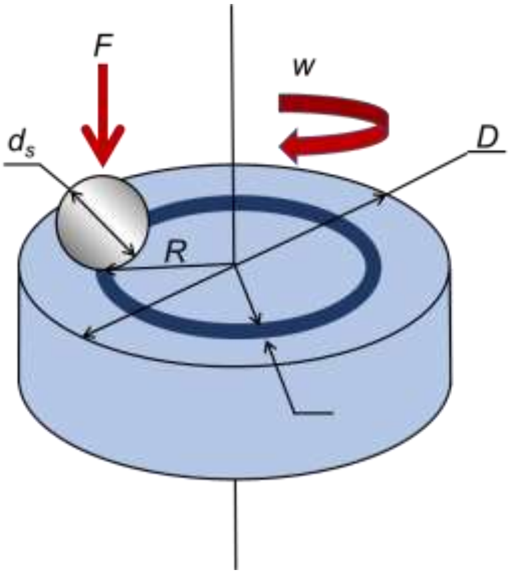

Fig. 3.4. Ball-on-Disk test configuration.

3.3 Results and discussion

3.3.1 Tribological performance of as-built samples

The surface roughness can significantly change the tribological behavior of that surface; therefore, a baseline needed to be established. To that end, the top surface of the sample fabricated with the manufacturer's recommended AM process parameters, in its as-built condition (R_a~4 µm), was tested under dry sliding conditions. Testing of such rough surface exhibited low repeatability of the specific wear rate (0.9–1.7 $\times 10^{-3}$ mm^3/mN) pertaining to a variable run-in distance with respect to CoF (20–35 m). Following, the bottom surface of the same sample (R_a=2.7 µm WEDM-generated) was tested, showing better specific wear rate repeatability (1.2–1.6 $\times 10^{-3}$ mm^3/mN) correlated with a shorter run-in distance (10–15 m). Finally, grinding the surface (R_a=0.6 µm) before testing resulted in the best repeatability of the specific wear rate (1.4–1.5 $\times 10^{-3}$ mm^3/mN) accompanying the shortest run-in distance (~3 m). Such wear rates were within the range reported in the literature on dry sliding testing of the SLM 316L stainless steel surfaces; 0.46 $\times 10^{-3}$ mm^3/mN in [35], 0.75 $\times 10^{-3}$ mm^3/mN in [21], and 3–7 $\times 10^{-3}$ mm^3/mN in [19]. Fig. 3.5. shows the evolution of the CoF with the sliding distance highlighting the decline of the run-in phase distance with the improved roughness of the tested surface. Prior to stabilizing at a steady-state value, the CoF of the ground surface exhibited an initial rise due to Hertzian contact, similar to what was reported in [21]. Also, an equal steady-state CoF of 0.57 was detected for all the three samples with various initial surface roughness: such CoF was within the steady-state CoF range (0.45–0.6) reported for dry sliding of SLM 316L stainless steel in [21, 35, 36]. The test was stopped at a distance of 100 m, after which the CoF stabilized, and the specific wear rate measurements were repeatable to a confidence level of 95% for the ground surface. Thus, to ensure consistent and comparable results, all samples have been ground to a surface roughness R_a ~ 0.6 µm before testing.

.

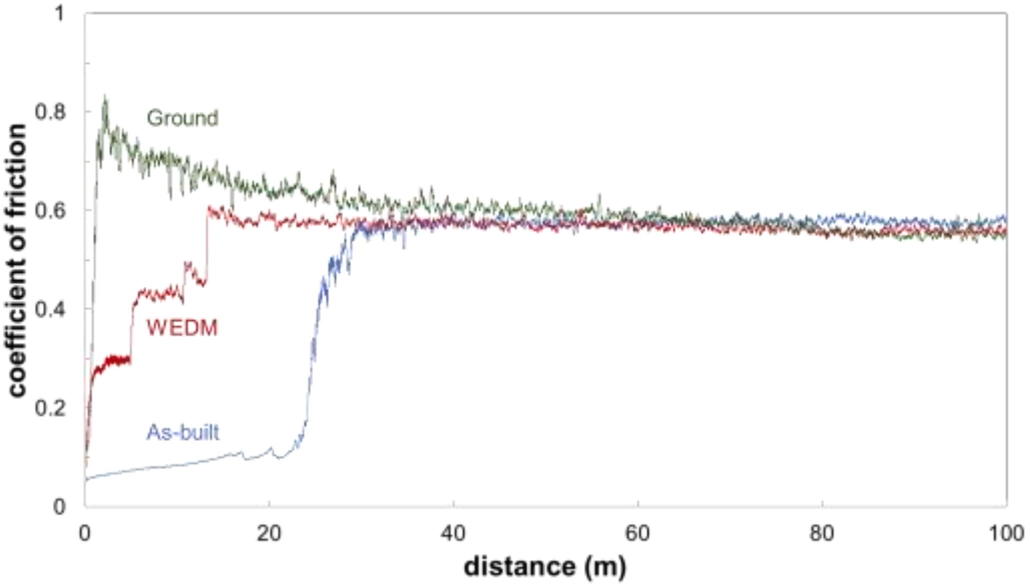

Fig. 3.5. Evolution of CoF for various surface conditions.

The AM part properties such as relative density, strength, fatigue resistance, and hardness were reported to depend on the utilized AM process parameters [31] and the laser scanning orientation between successive layers [30]. The impact of such parameters was investigated by fabricating and testing samples with a selected AM process parameters (Table 3.1.) and subsequent layer orientation (Fig. 3.1.). As shown in Fig. 3.6., despite a notable 50% increase in the volumetric energy density for the high density compared to the high strength sample, the hardness did not show any considerable difference. The undetectable hardness variation does not contradict the minor difference of yield strength (5%) observed in [31] for samples with the same process parameters. Similarly, the various orientations between layers and the double exposure did not significantly impact the sample hardness as opposed to [30], which reported a change in the hardness at a lower power range (100–150 W). Therefore, it is concluded that a considerable change in hardness could not be achieved within the investigated process parameters window.

The comparable hardness for all tested AM surfaces contributed to similar specific wear rates (Fig. 3.6.). Meanwhile, the average hardness of all AM samples (~ 240–250 HV) was higher than the hardness of a cold-rolled sample (200 HV). Such an increase in hardness can be related to the finer microstructure expected with the rapid cooling during the SLM process, as reported in [37]. Expectedly, the lower hardness of the cold-rolled sample induced a higher specific wear rate than the AM samples. Fig. 3.7.b, c, and d represent the wear scars of manufacturer-recommended, high strength, and high density AM samples. The evidence of a strong adhesion of agglomerated wear particles in a plate-shaped form was observed, implying the dominance of the adhesive wear mechanism for the three AM samples. On the other hand, the deeper grooves on the surface of the cold-rolled sample (Fig. 3.7.a) indicate the dominance of the abrasive wear mechanism. Furthermore, the strain hardening effect on the worn surface increased the hardness to (~ 300 HV), while the hardness on accumulated wear particles was (~ 380 HV). Such hardness promotes better wear resistance for the AM parts correlated to their dominant adhesion wear.

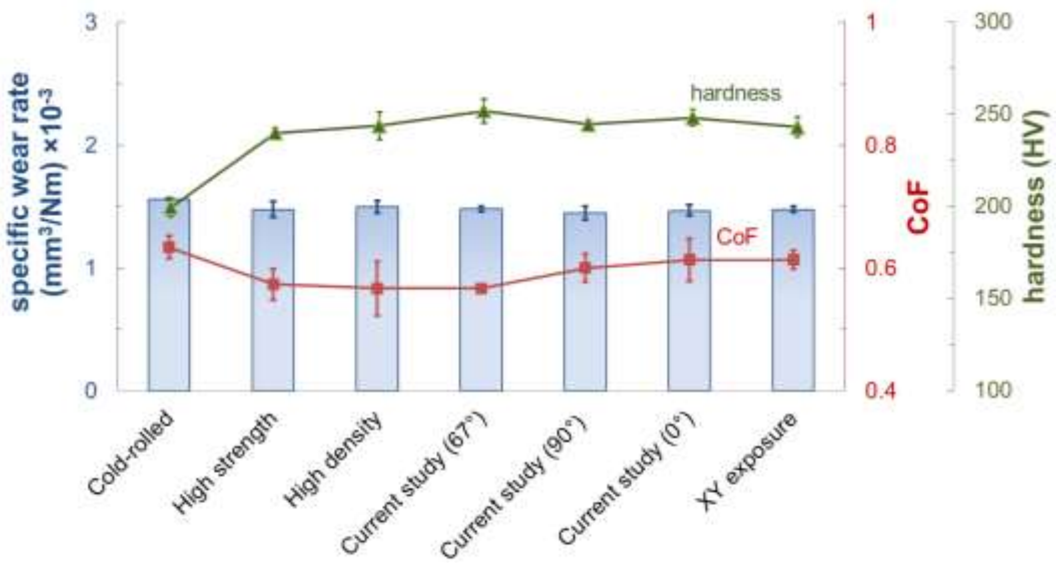

Fig. 3.6. The hardness and tribological response of untextured surfaces.

The CoF depends on the surface asperities deformation, adhesion, plowing, and wear debris particles agglomeration [38]. For the tested AM samples, surface topography and material properties were unchanged, explaining the unaffected wear mechanism and the insignificant variation in the CoF (Fig. 3.6.). The observed independence of the tribological response on the AM process parameters came in line with [16], which concluded that CoF and wear rate are independent of laser power and building direction for the SLM 316L stainless steel. However, with the change of the dominant wear mechanism, a higher CoF was observed for the cold-rolled samples compared to that of the AM samples.

Generally, it can be concluded that AM surfaces are superior to cold-rolled regarding the hardness and the tribological response in terms of wear resistance and CoF. Yet, the difference between the specific wear rate and CoF of AM and cold-rolled surfaces remains limited. Additionally, the variation of both the process parameters and the successive layer orientations were ineffective approaches to enhance the tribological response of AM surfaces. Therefore, the next section will investigate the efficacy of surface texturing as a potential candidate to improve the AM surface tribological behavior.

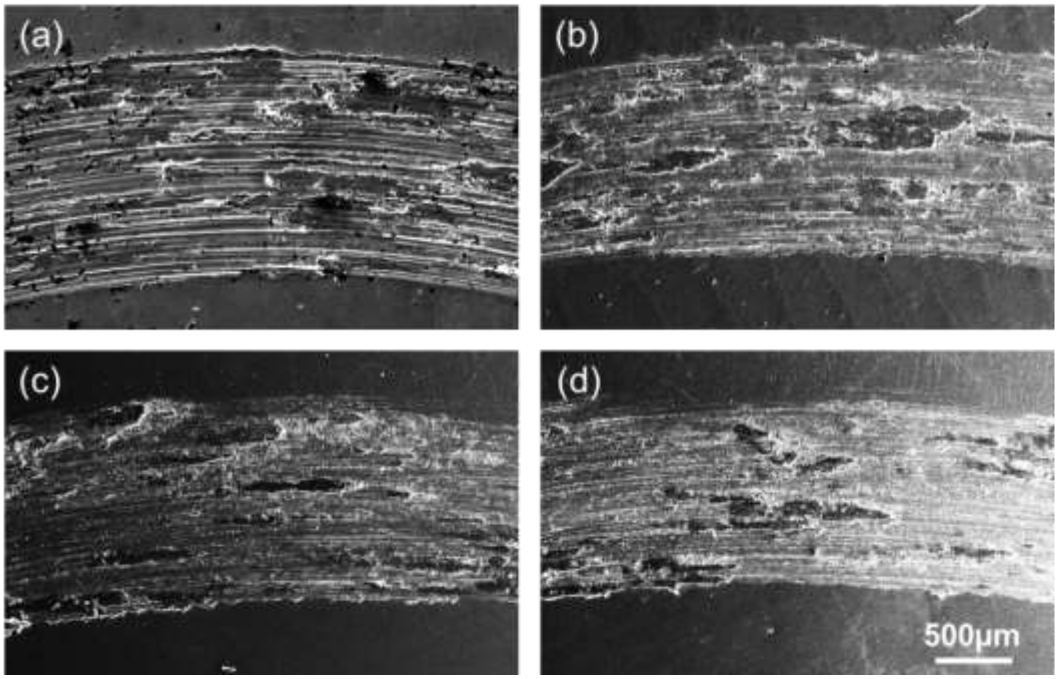

Fig. 3.7. SEM images for wear scars (a) cold-rolled (b) manufacturer recommended (c) high strength (d) high density.

3.3.2 Texturing dimensional limitations

The concept of adding patterns of micro-cavities to a surface to enhance its tribological response has been utilized successfully for conventional fabrication and texturing methods [1]. For AM parts, assessing the manufacturing capabilities and limitations of the used SLM process is crucial to explore the efficacy of such an approach. The lack of reliable literature on these limitations was explored and discussed in [27] with a focus on the protruding features to attain lower wettability. Extending the same concept and following the guidelines presented in [32], an array of cavities with different shapes and descending dimensions was fabricated to evaluate each shape's minimum feasible feature dimension (Fig. 3.8.a). Identical arrays were repeated for the depth range of 40–200 µm resulting in a similar limiting size of 200 µm for all the shapes at any depth. The shapes and depth of the texturing cavities were frequently reported to impact the hydrodynamic pressure and the film thickness in lubricated testing conditions [2]. Since this study investigates the tribological response at dry conditions, the main focus is placed on texturing density and feature dimensions.

As one of the most successful textures to render better tribological performance under dry conditions [5], the circular dimples were further investigated (Fig. 3.8.b). As varying the depth did not impact the limiting dimension, an array was fabricated entailing through holes with a depth of 8 mm equal to the height of the samples. With finer descending steps of the hole diameters, the limiting dimension was found to be 150 µm. The conventional deep hole drilling of a hole with such a high aspect ratio (53:1) is a lengthy, costly, and complicated process. Even with a non-conventional approach like micro-EDM, it took a 30 mm electrode with coated side and 30 minutes to complete a single hole with a comparable aspect ratio [39]. On the other hand, SLM can build parts with integrated high aspect ratio patterns without adding significant time or cost.

Noticeable irregularities and shape deviations were observed (Fig. 3.8.a, b) for the fabricated shapes, potentially affecting their functionality. Contouring the desired geometry of the cavities was tested for the deep circular holes resulting in higher shape accuracy and lower irregularities (Fig. 3.8.c). Despite this geometrical improvement, a minimum diameter of 250 µm was observed for the contoured holes, significantly larger than the 150 µm for the non-contoured ones. The added laser exposure step at the microfeature rims in contouring may have caused the molten metal to flow and fill the cavity of a smaller diameter. Contouring was adopted in [29] to study the efficacy of varying the cavity shape on the surface tribological response via fabricating shallow cavities with a governing dimension over 400 µm.

Texturing with a linear grooves pattern was also used successfully to improve the tribological response in the dry sliding conditions [1]. An array of linear grooves with descending width was fabricated (Fig. 3.8.d) to assess the limiting width of such grooves. For the examined depth range of (40–520 µm), the limiting groove width was found independent of depth and of an approximate value of 200 µm. Additionally, all the fabricated textures were non-contoured to widen the range of the studied dimensions.

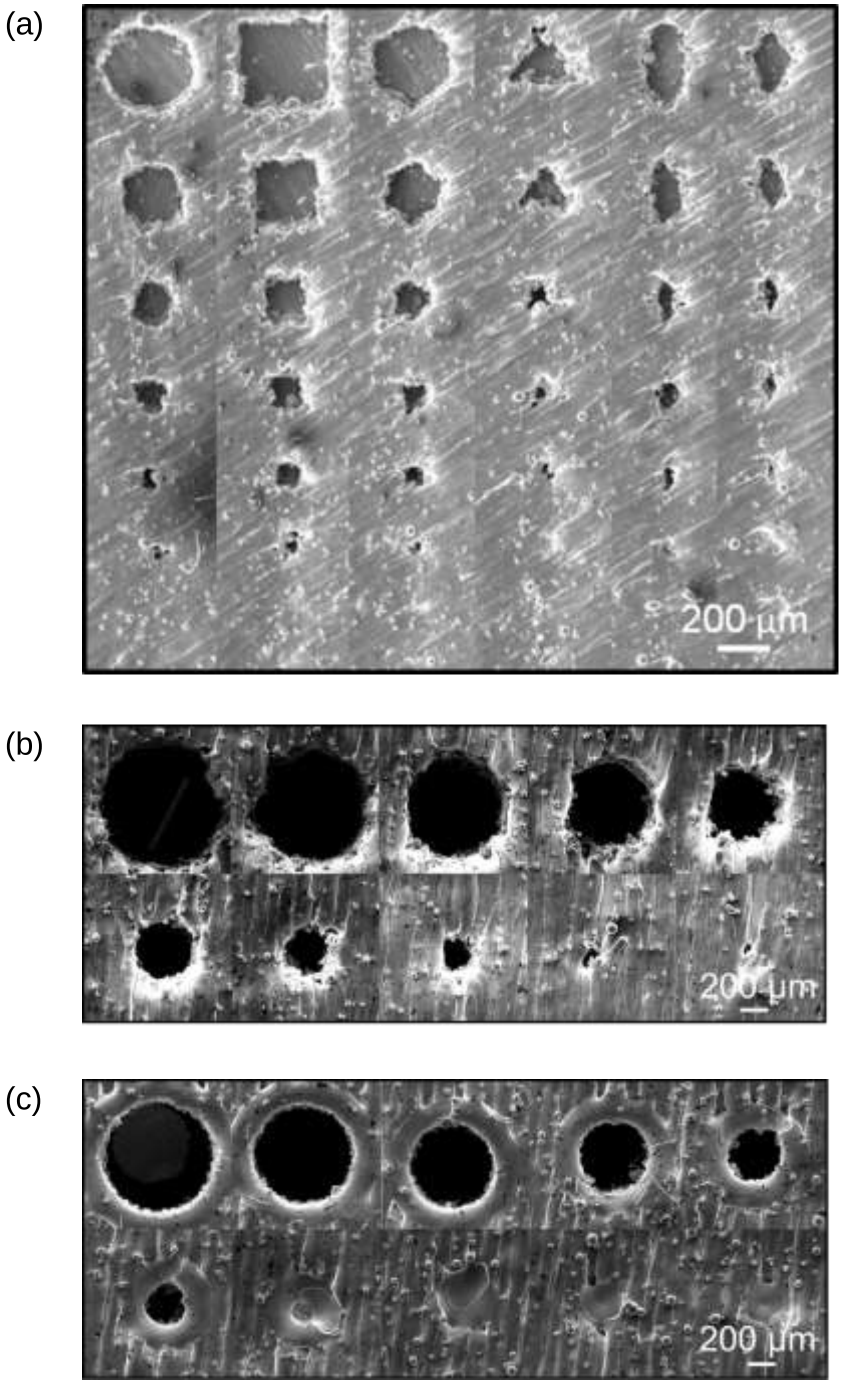
(a)
200 µm
(b)
200 µm
(c)
200 µm

(d)

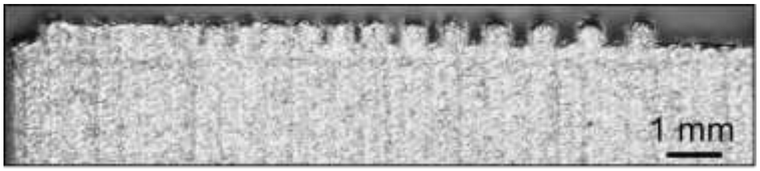

Fig. 3.8. Minimum feature dimension assessment for (a) various shapes. elaboration for deep circular dimples (b) non-contoured (c) contoured, and (d) grooves.

3.3.3 Tribological performance of the textured surfaces

For steels under dry sliding conditions, circular dimples [40] and linear grooves [41] were the most successfully utilized texturing shapes to enhance the tribological response. Texturing areal density, the term referring to the ratio of the sum of texturing feature areas to the total area, has been acknowledged to impact tribological response significantly [1, 5]. Moreover, the width of the utilized texturing features was found to be crucially related to the resulting tribological behavior [2]. To explore the impact of such parameters, dimpled and grooved samples, with three different levels of areal density (5, 20, and 44%) and a range of diameters (150–750 µm), were fabricated and tested. Fig. 3.9.a shows that increasing areal density (5 to 44%) for the dimple-textured samples reduced the specific wear rate (1 to 0.4 mm^3/Nm). While, Fig. 3.9.b presents a reduction of the specific wear rate (1.1 to 0.4 mm^3/Nm) with the increase of the dimple diameter (450 to 750 µm), at a constant areal density of 44%. For the groove textured samples, a similar trend was observed for the specific wear rate, which was reduced (0.7 to 0.45 mm^3/Nm) with the areal density rise (5 to 44%) (Fig. 3.10.a). Also, at a constant 44% areal density, specific wear rates declined (1.45 to 0.45 mm^3/Nm) with the groove width change (200 to 600 µm) (Fig. 3.10.b).

In general, Fig. 3.9. and Fig. 3.10. demonstrate that textured surfaces had lower specific wear rates compared to non-textured surfaces. Under dry sliding conditions, such texturing impact can be contributed to; the texturing features entrapment of the wear debris particles, the reduction of the actual contact area, and the unique stress distribution [2]. Furthermore, with higher texturing areal density, the actual contact area declined, reducing the specific wear rate for dimple/groove-textured surfaces. Such a wear rate reduction came in line with [29], where a mass loss drop (1 to 0.3 g) was observed with the change of areal density (6.6 to 26 %).

Fig. 3.9. and Fig. 3.10. show that the CoF did not reflect the improvement in the wear rate associated with higher areal density or texturing feature width. Such counterintuitive CoF behavior came in agreement with [42], which reported a 26% increase of the micro-scale textured surface CoF compared to that of the untextured one. This behavior can be related to increased stiction forces associated with the dominance of adhesion. The single case where the CoF followed the same trend as the specific wear rate (Fig. 3.9.b) can be related to the spacing between grooves similar to the observations made by [43]. This increased CoF may be beneficial for high-friction applications, as demonstrated by [44]. The CoF may change dramatically with different contact conditions; for example, with a shaft-in-bushing testing condition, a considerable decrease of the CoF reaching values near that of boundary condition lubrication was observed for the textured surfaces [38]. Such CoF difference with various contact conditions

signifies the importance of adjusting the tribological testing conditions to mimic the actual operating conditions of the functional part to obtain more reliable results.

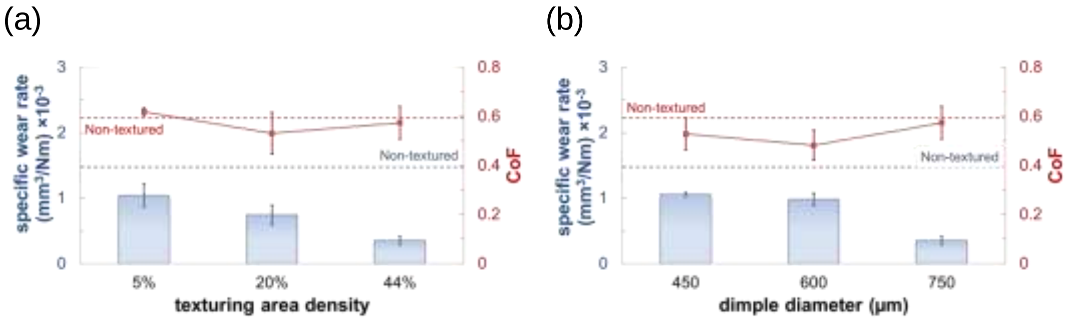

Fig. 3.9. The impact of (a) texturing areal density (b) dimple diameter on the CoF and the specific wear rate of dimple-textured samples.

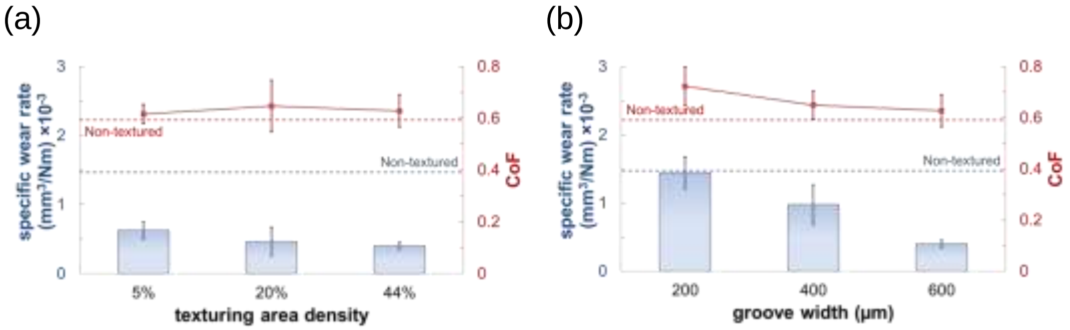

Fig. 3.10. The impact of (a) texturing areal density (b) groove width on the CoF and the specific wear rate of groove-textured samples.

Groove-textured surfaces were observed to have a less specific wear rate than the dimple-textured ones in the case of the lower feature width. Comparing wear scars of both textures at a fixed areal density of 20% and feature diameter/width of 200 µm, dimples suffered a complete blockage due to the adhered wear particle (Fig. 3.11.a) opposing grooves that did not experience the same problem

(Fig. 3.12.). Such a blockage deprived dimples with lower diameters of the ability to entrap wear debris. To further investigate the impact of dimple diameter on the entrapment ability of wear particles, a normalized value for the specific wear rate was proposed using the actual rather than the total sliding distance. By removing the contact area reduction effect, Fig. 3.13. demonstrates a diameter threshold of 400 µm, after which the wear rate decreased below the non-textured value indicating the sole ability of debris trapping of the dimples. Although the normalized wear rate values associated with diameters below the 400 µm threshold were higher than that of the non-textured values, the textured surfaces' actual wear rate values were lower than the non-textured surfaces. Fig. 3.11.b shows an image of the wear scar of a non-blocked dimple-textured surface with a 400 µm. Severe plastic deformation, cracks, and delaminations were observed at dimple rims (Fig. 3.11.b), and groove edges (Fig. 3.12.) as evidence of the higher applied stresses at these locations in line with the findings of [29].

Groove orientation was beneficial for tribological response enhancement, vibration, and noise reduction for compacted railway brake discs [45]. To further explore such an impact of groove orientation on the tribological response, groove-textured surfaces (20% areal density and 400 µm width) were manufactured with different orientations (0°, 15°, 30°, 45°, and 60°) with respect to the sliding direction. Fig. 3.14. shows a declining trend in the specific wear rate, and the CoF with the groove inclination angle increase, similar to what was observed in Fig. 3.10.b. Such trend can be attributed to the increased texturing areal density along the wear track, which can be calculated by dividing the area density by the cosine of the groove inclination angle. Thus, tilting grooves by 60° cause twice the actual texturing areal density compared to the 0° grooves at the sliding track, decreasing the specific wear rate to 50% of the non-tilted grooves and 30% of the non-textured surface. Additionally, the orientation of the grooves allows gradual engagement with the counter body with reduced force resulting in better stress distribution, as discussed in [46].

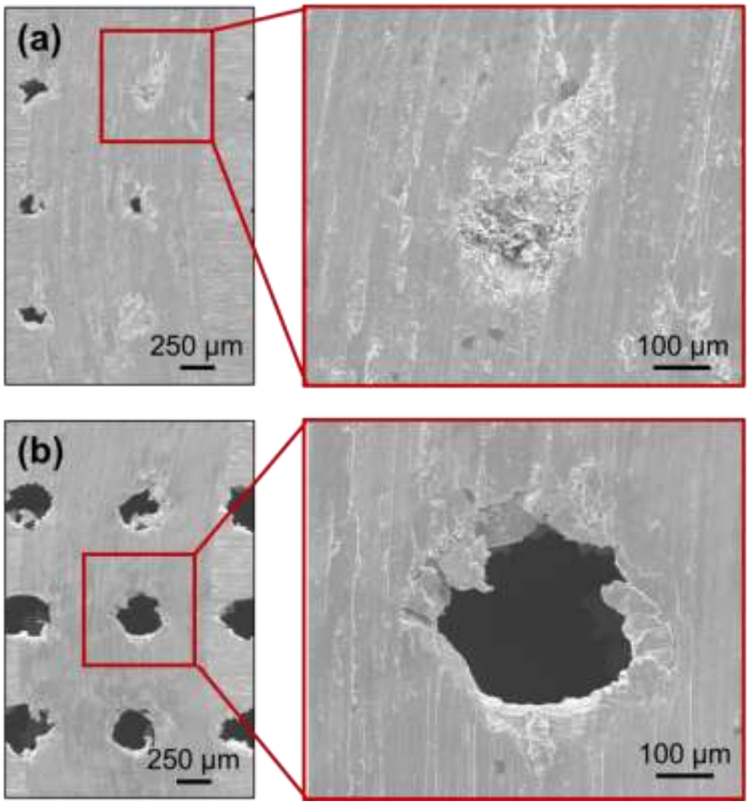

Fig. 3.11. SEM images of wear track for dimple-textured surfaces with diameters of (a) 200 μm. (b) 400 μm.

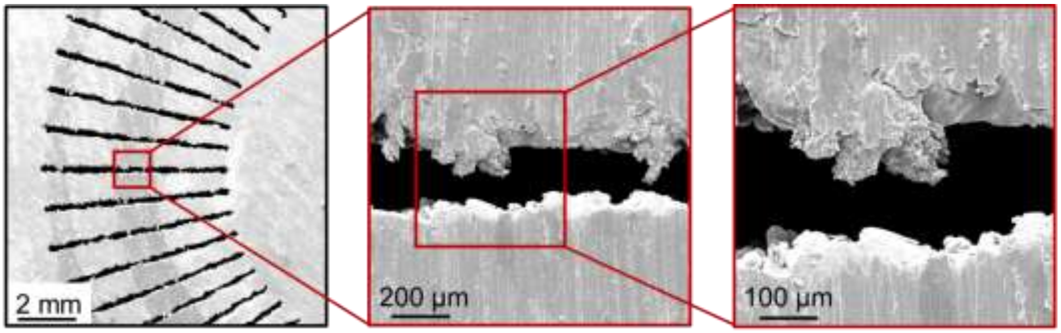

Fig. 3.12. SEM images of wear track of a groove-textured surface 20% density and 200 µm width.

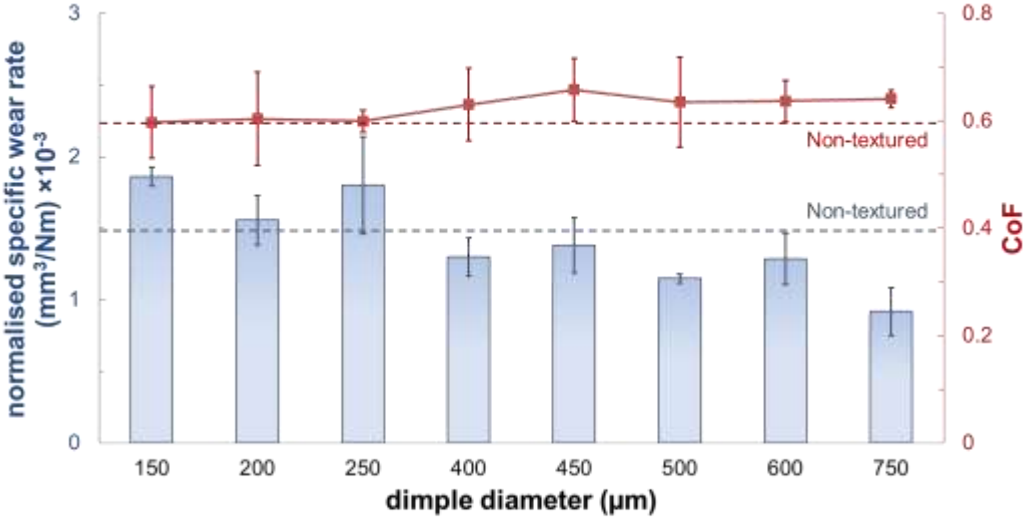

Fig. 3.13. Normalized wear rate and CoF change with various dimple diameters.

Another potential benefit arising from the groove geometry is that it allows the centrifugal force to move the wear debris away from the wear location, preventing any possible seizures as concluded for cast-iron brake discs [47]. Groove orientation enhances the role of centrifugal force to shift the wear particles away from the wear location radially, yet, the rotation direction will affect the results. Fig. 3.15. shows the reduced specific wear rate and CoF associated with the counter-clockwise rotation compared to the clockwise one.

The chevron-shaped grooves were found to be the most effective texturing geometry in numerical optimization for unidirectional lubricated sliding cases [48]. Furthermore, the angle and aspect ratio of crosshatched grooves were studied, demonstrating the ability of such texture to improve the tribological response in lubricated conditions [49]. In the current study, the efficacy of the chevron (V-shaped) and crosshatch (X-shaped) groove texturing was explored under dry sliding conditions. The specific wear rate and the CoF of the 30°, V-grooved, and X-grooved samples were shown in both rotation directions (Fig. 3.15.). For both shapes, the CoF and the specific wear rates were found to be 40% and 20% of that of the non-textured surfaces. The direction of rotation had a similar impact on the V-shaped grooves to the one observed for the 30° grooves, while the X-grooved sample, expectedly, was not sensitive to the rotation direction. Such improvement may be attributed to the applied force reduction, as the radial force components act along counter directions causing more even stress distribution.

The lowest specific wear rate obtained for the proposed textured surfaces was 20% of that of the non-textured surface, with a 60% reduction in the CoF. Such results validate the possibility of utilizing surface texturing to tailor the tribological response of AM surfaces under dry sliding conditions.

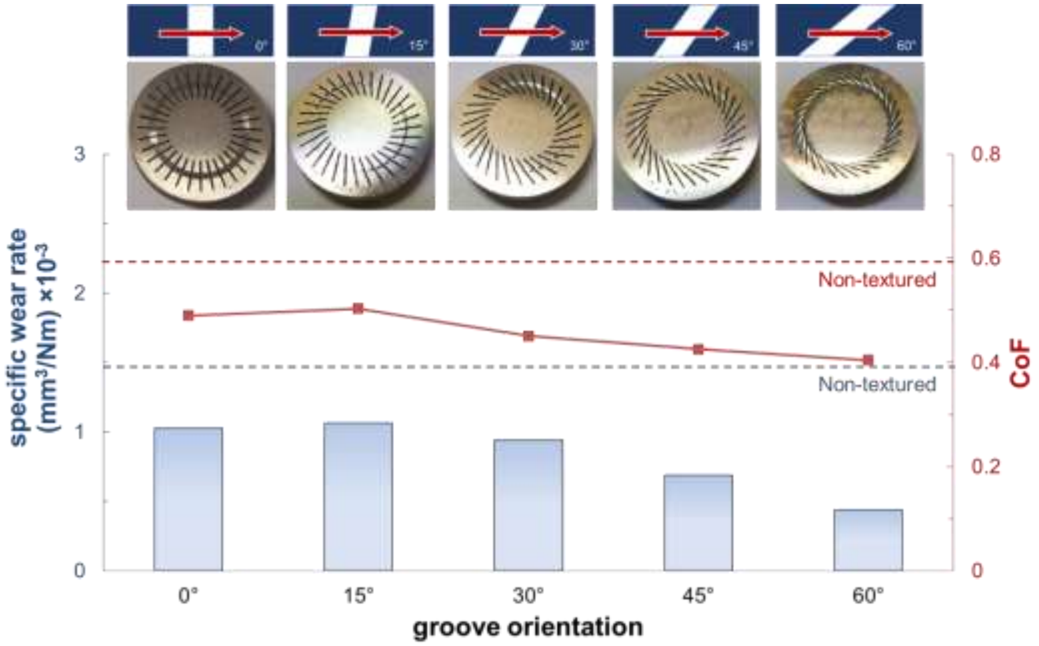

Fig. 3.14. Groove orientation effect on specific wear rate.

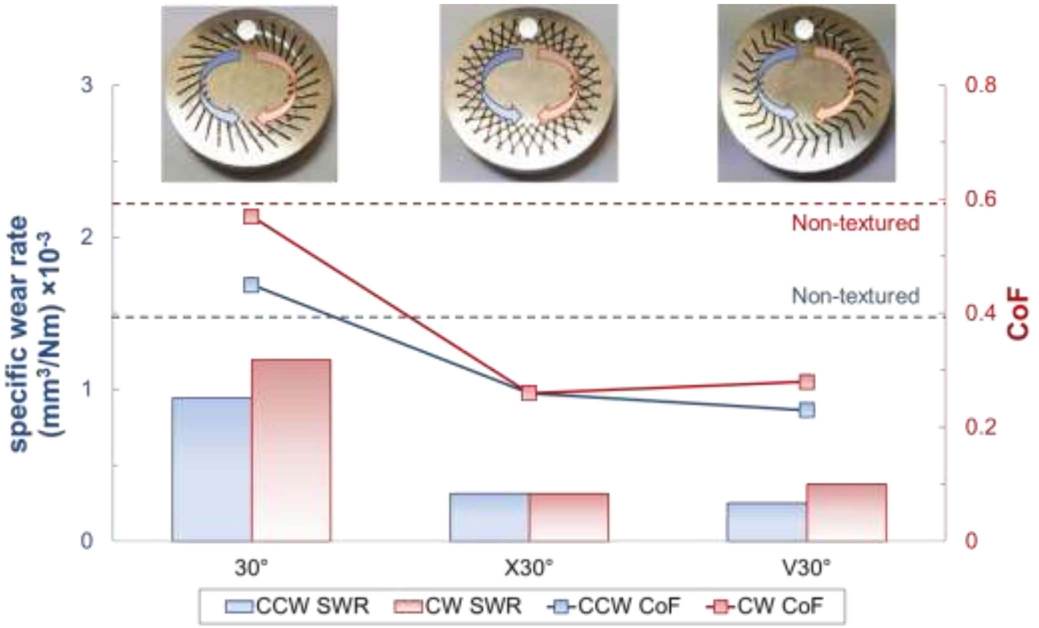

Fig. 3.15. The influence of sliding direction on the specific wear rate.

3.4 Conclusions

Intending to enhance the tribological response of AM surfaces, this study explored the specific wear rate and CoF of the as-built surfaces. Then, various texturing patterns were utilized to control the tribological performance under dry sliding conditions. The conclusions of the presented work can be listed as follows:

- AM samples exhibited a 12% and 7% reduction in CoF and specific wear rates, respectively, compared to the cold-rolled samples attributed to their higher hardness and finer microstructure.
- The tribological behavior of the non-textured AM surfaces was found independent of the process parameters and orientation between successive layers.
- The SLM process limitations were explored, highlighting a minimum hole/groove width of 150–200 µm. Yet, a minimum diameter of 400 µm was evaluated to enable dimples to act as a wear debris trap.
- Increasing texturing areal density and feature width decreased the specific wear rate for the dimple/groove textured surfaces due to the associated reduction in the actual contact area and the entrapment of the wear particles.
- The orientation of the texturing grooves relative to the sliding direction reduces CoF and specific wear rate. Such orientation increases the groove width and areal density at the wear track location and induces gradual engagement and better stress distribution.

- With a 60% reduction in CoF and 80% less specific wear rates, X-shaped and V-shaped grooves exhibited the best tribological response among the proposed textures.

The work at hand explored the potential of utilizing the texturing concept to tailor the AM surface tribological response under dry sliding conditions. The obtained results signified the impact of texturing on the surface tribological behavior. Such an impact emphasized further investigation to acquire various functional surfaces, expanding the AM application envelope.

Acknowledgement

This work was funded in part by the Natural Sciences and Engineering Research Council (NSERC) of Canada.

References

[1] T. Ibatan, M.S. Uddin, M.A.K. Chowdhury, Recent development on surface texturing in enhancing tribological performance of bearing sliders, Surface and Coatings Technology 272 (2015) 102–120. https://doi.org/10.1016/j.surfcoat.2015.04.017

[2] C. Gachot, A. Rosenkranz, S.M. Hsu, H.L. Costa, A critical assessment of surface texturing for friction and wear improvement, Wear 372–373 (2017) 21–41. https://doi.org/10.1016/j.wear.2016.11.020

[3] A. Chyr, M. Qiu, J.W. Speltz, R.L. Jacobsen, A.P. Sanders, B. Raeymaekers, A patterned microtexture to reduce friction and increase longevity of prosthetic hip joints, Wear 315(1–2) (2014) 51–57. https://doi.org/10.1016/j.wear.2014.04.001

[4] P. Lu, R.J.K. Wood, Tribological performance of surface texturing in mechanical applications—a review, Surface Topography: Metrology and Properties 8(4) (2020) 043001. https://doi.org/10.1088/2051-672X/abb6d0

[5] A.F.S. Baharin, M.J. Ghazali, J.A. Wahab, Laser surface texturing and its contribution to friction and wear reduction: a brief review, Industrial Lubrication and Tribology 68(1) (2016) 57–66. https://doi.org/10.1108/ILT-05-2015-0067

[6] A. Amanov, R. Tsuboi, H. Oe, S. Sasaki, The influence of bulges produced by laser surface texturing on the sliding friction and wear behavior, Tribology International 60 (2013) 216–223. https://doi.org/10.1016/j.triboint.2012.10.018

[7] Y. Gao, B. Wu, Y. Zhou, S. Tao, A two-step nanosecond laser surface texturing process with smooth surface finish, Applied Surface Science 257(23) (2011) 9960–9967. https://doi.org/10.1016/j.apsusc.2011.06.115

[8] T. DebRoy, H. Wei, J. Zuback, T. Mukherjee, J. Elmer, J. Milewski, A.M. Beese, A. Wilson-Heid, A. De, W. Zhang, Additive manufacturing of metallic components–process, structure and properties, Progress in Materials Science 92 (2018) 112–224. https://doi.org/10.1016/j.pmatsci.2017.10.001

[9] D. Gu, Y.-C. Hagedorn, W. Meiners, G. Meng, R.J.S. Batista, K. Wissenbach, R. Poprawe, Densification behavior, microstructure evolution, and wear performance of selective laser melting processed commercially pure titanium, Acta Materialia 60(9) (2012) 3849–3860. https://doi.org/10.1016/j.actamat.2012.04.006

[10] Y. Sun, A. Moroz, K. Alrbaey, Sliding Wear Characteristics and Corrosion Behaviour of Selective Laser Melted 316L Stainless Steel, Journal of Materials Engineering and Performance 23(2) (2014) 518–526. https://doi.org/10.1007/s11665-013-0784-8

[11] N. Diaz Vallejo, C. Lucas, N. Ayers, K. Graydon, H. Hyer, Y. Sohn, Process Optimization and Microstructure Analysis to Understand Laser Powder Bed Fusion of 316L Stainless Steel, Metals 11(5) (2021) 832. https://doi.org/10.3390/met11050832

[12] H. Li, M. Ramezani, Z.W. Chen, Dry sliding wear performance and behaviour of powder bed fusion processed Ti–6Al–4V alloy, Wear 440–441 (2019) 203103. https://doi.org/10.1016/j.wear.2019.203103

[13] F. Bartolomeu, M. Buciumeanu, E. Pinto, N. Alves, O. Carvalho, F.S. Silva, G. Miranda, 316L stainless steel mechanical and tribological behavior—A comparison between selective laser melting, hot pressing and conventional

casting, Additive Manufacturing 16 (2017) 81–89. https://doi.org/10.1016/j.addma.2017.05.007

[14] K. Geenen, A. Röttger, F. Feld, W. Theisen, Microstructure, mechanical, and tribological properties of M3:2 high-speed steel processed by selective laser melting, hot-isostatic pressing, and casting, Additive Manufacturing 28 (2019) 585–599. https://doi.org/10.1016/j.addma.2019.05.028

[15] W. Yang, X. He, H. Li, J. Dong, W. Chen, H. Xin, Z. Jin, A tribological investigation of SLM fabricated TC4 titanium alloy with carburization pre-treatment, Ceramics International 46(3) (2020) 3043–3050. https://doi.org/10.1016/j.ceramint.2019.10.004

[16] H. Li, M. Ramezani, M. Li, C. Ma, J. Wang, Effect of process parameters on tribological performance of 316L stainless steel parts fabricated by selective laser melting, Manufacturing Letters 16 (2018) 36–39. https://doi.org/10.1016/j.mfglet.2018.04.003

[17] X. Yan, S. Gao, C. Chang, J. Huang, K. Khanlari, D. Dong, W. Ma, N. Fenineche, H. Liao, M. Liu, Effect of building directions on the surface roughness, microstructure, and tribological properties of selective laser melted Inconel 625, Journal of Materials Processing Technology 288 (2021) 116878. https://doi.org/10.1016/j.jmatprotec.2020.116878

[18] J. Ju, Y. Zhou, K. Wang, Y. Liu, J. Li, M. Kang, J. Wang, Tribological investigation of additive manufacturing medical Ti6Al4V alloys against Al2O3 ceramic balls in artificial saliva, Journal of the Mechanical Behavior of Biomedical Materials 104 (2020) 103602. https://doi.org/10.1016/j.jmbbm.2019.103602

[19] M. Bahshwan, C.W. Myant, T. Reddyhoff, M.-S. Pham, The role of microstructure on wear mechanisms and anisotropy of additively manufactured 316L stainless steel in dry sliding, Materials & Design 196 (2020) 109076. https://doi.org/10.1016/j.matdes.2020.109076

[20] C. Cai, C. Radoslaw, J. Zhang, Q. Yan, S. Wen, B. Song, Y. Shi, In-situ preparation and formation of TiB/Ti-6Al-4V nanocomposite via laser additive manufacturing: Microstructure evolution and tribological behavior, Powder Technology 342 (2019) 73–84. https://doi.org/10.1016/j.powtec.2018.09.088

[21] K. Turalıoğlu, M. Taftalı, H. Tekdir, O. Çomaklı, M. Yazıcı, T. Yetim, A.F. Yetim, The tribological and corrosion properties of anodized Ti6Al4V/316L bimetallic structures manufactured by additive manufacturing, Surface and

Coatings Technology 405 (2021) 126635. https://doi.org/10.1016/j.surfcoat.2020.126635

[22] M. Tang, L. Zhang, N. Zhang, Microstructural evolution, mechanical and tribological properties of TiC/Ti6Al4V composites with unique microstructure prepared by SLM, Materials Science and Engineering: A 814 (2021) 141187. https://doi.org/10.1016/j.msea.2021.141187

[23] N. Kang, W. Ma, F. Li, H. Liao, M. Liu, C. Coddet, Microstructure and wear properties of selective laser melted WC reinforced 18Ni–300 steel matrix composite, Vacuum 154 (2018) 69–74. https://doi.org/10.1016/j.vacuum.2018.04.044

[24] X. Wang, J. Liu, Y. Wang, Y. Fu, Fabrication of friction-reducing texture surface by selective laser melting of ink-printed (SLM-IP) copper (Cu) nanoparticles(NPs), Applied Surface Science 396 (2017) 659–664. https://doi.org/10.1016/j.apsusc.2016.11.003

[25] H. Tekdir, A.F. Yetim, Additive manufacturing of multiple layered materials (Ti6Al4V/316L) and improving their tribological properties with glow discharge surface modification, Vacuum 184 (2021) 109893. https://doi.org/10.1016/j.vacuum.2020.109893

[26] A. Amanov, Advancement of tribological properties of Ti–6Al–4V alloy fabricated by selective laser melting, Tribology International, 155 (2021) 106806. https://doi.org/10.1016/j.triboint.2020.106806

[27] S. Mekhiel, P. Koshy, M.A. Elbestawi, Additive texturing of metallic surfaces for wetting control, Additive Manufacturing 37 (2021) 101631. https://doi.org/10.1016/j.addma.2020.101631

[28] J.Y. Ho, K.K. Wong, K.C. Leong, Saturated pool boiling of FC-72 from enhanced surfaces produced by selective laser melting, International Journal of Heat and Mass Transfer 99 (2016) 107–121. https://doi.org/10.1016/j.ijheatmasstransfer.2016.03.073

[29] H. Kovacı, Y. Seçer, Improved tribological performance of AISI 316L stainless steel by a combined surface treatment: Surface texturing by selective laser melting and plasma nitriding, Surface and Coatings Technology 400 (2020) 126178. https://doi.org/10.1016/j.surfcoat.2020.126178

[30] E. Liverani, S. Toschi, L. Ceschini, A. Fortunato, Effect of selective laser melting (SLM) process parameters on microstructure and mechanical properties

of 316L austenitic stainless steel, Journal of Materials Processing Technology 249 (2017) 255–263. https://doi.org/10.1016/j.jmatprotec.2017.05.042

[31] M. Yakout, M.A. Elbestawi, S.C. Veldhuis, Density and mechanical properties in selective laser melting of Invar 36 and stainless steel 316L, Journal of Materials Processing Technology 266 (2019) 397–420. https://doi.org/10.1016/j.jmatprotec.2018.11.006

[32] L. Rebaioli, I. Fassi, A review on benchmark artifacts for evaluating the geometrical performance of additive manufacturing processes, The International Journal of Advanced Manufacturing Technology 93(5–8) (2017) 2571–2598. https://doi.org/10.1007/s00170-017-0570-0

[33] A.B. Spierings, G. Levy, Comparison of density of stainless steel 316L parts produced with selective laser melting using different powder grades, Proceedings of the Annual International Solid Freeform Fabrication Symposium, Austin, TX, (2009) 342–353.

[34] ASTM International, ASTM G99-17, Standard test method for wear testing with a pin-on-disk apparatus, ASTM International, West Conshohocken, PA, (2017) 1–5. https://doi.org/10.1520/G0099-17

[35] S. Alvi, K. Saeidi, F. Akhtar, High temperature tribology and wear of selective laser melted (SLM) 316L stainless steel, Wear 448–449 (2020) 203228. https://doi.org/10.1016/j.wear.2020.203228

[36] H. Li, M. Ramezani, M. Li, C. Ma, J. Wang, Tribological performance of selective laser melted 316L stainless steel, Tribology International 128 (2018) 121–129. https://doi.org/10.1016/j.triboint.2018.07.021

[37] R.I. Revilla, M. Van Calster, M. Raes, G. Arroud, F. Andreatta, L. Pyl, P. Guillaume, I. De Graeve, Microstructure and corrosion behavior of 316L stainless steel prepared using different additive manufacturing methods: A comparative study bringing insights into the impact of microstructure on their passivity, Corrosion Science 176 (2020) 108914. https://doi.org/10.1016/j.corsci.2020.108914

[38] N.P. Suh, M. Mosleh, P.S. Howard, Control of friction, Wear 175(1) (1994) 151–158. https://doi.org/10.1016/0043-1648(94)90178-3

[39] E. Ferraris, V. Castiglioni, F. Ceyssens, M. Annoni, B. Lauwers, D. Reynaerts, EDM drilling of ultra-high aspect ratio micro holes with insulated tools, CIRP Annals 62(1) (2013) 191–194. https://doi.org/10.1016/j.cirp.2013.03.115

[40] L. Rapoport, A. Moshkovich, V. Perfilyev, I. Lapsker, G. Halperin, Y. Itovich, I. Etsion, Friction and wear of MoS2 films on laser textured steel surfaces, Surface and Coatings Technology 202(14) (2008) 3332–3340. https://doi.org/10.1016/j.surfcoat.2007.12.009

[41] A. Rosenkranz, L. Reinert, C. Gachot, F. Mücklich, Alignment and wear debris effects between laser-patterned steel surfaces under dry sliding conditions, Wear 318(1) (2014) 49–61. https://doi.org/10.1016/j.wear.2014.06.016

[42] M. Kang, Y.M. Park, B.H. Kim, Y.H. Seo, Micro- and nanoscale surface texturing effects on surface friction, Applied Surface Science 345 (2015) 344–348. https://doi.org/10.1016/j.apsusc.2015.03.194

[43] Z. Wang, Q. Zhao, C. Wang, Y. Zhang, Modulation of dry tribological property of stainless steel by femtosecond laser surface texturing, Applied Physics A 119(3) (2015) 1155–1163. https://doi.org/10.1007/s00339-015-9085-4

[44] A. Dunn, K.L. Wlodarczyk, J.V. Carstensen, E.B. Hansen, J. Gabzdyl, P.M. Harrison, J.D. Shephard, D.P. Hand, Laser surface texturing for high friction contacts, Applied Surface Science 357 (2015) 2313–2319. https://doi.org/10.1016/j.apsusc.2015.09.233

[45] D.W. Wang, J.L. Mo, M.Q. Liu, J.X. Li, H. Ouyang, M.H. Zhu, Z.R. Zhou, Improving tribological behaviours and noise performance of railway disc brake by grooved surface texturing, Wear 376–377 (2017) 1586–1600. https://doi.org/10.1016/j.wear.2017.01.022

[46] Y. Xing, J. Deng, X. Feng, S. Yu, Effect of laser surface texturing on Si3N4/TiC ceramic sliding against steel under dry friction, Materials & Design 52 (2013) 234–245. https://doi.org/10.1016/j.matdes.2013.05.077

[47] M. Mosleh, B.A. Khemet, A Surface Texturing Approach for Cleaner Disc Brakes, Tribology Transactions 49(2) (2006) 279–283. https://doi.org/10.1080/05698190600639913

[48] C. Shen, M.M. Khonsari, Numerical optimization of texture shape for parallel surfaces under unidirectional and bidirectional sliding, Tribology International 82 (2015) 1–11. https://doi.org/10.1016/j.triboint.2014.09.022

[49] M.-s. Suh, Y.-h. Chae, S.-s. Kim, T. Hinoki, A. Kohyama, Effect of geometrical parameters in micro-grooved crosshatch pattern under lubricated sliding friction, Tribology International 43(8) (2010) 1508–1517. https://doi.org/10.1016/j.triboint.2010.02.012

Chapter 4

Optimization of Laser Peening Parameters for Additively Manufactured Metallic Parts

Complete Citation:

S. Mekhiel, M. A. Balbaa, M.A., Elbestawi, Philip Koshy, Lloyd Hackel (2021). Optimization of Laser Peening Parameters for Additive Manufactured Metallic Parts. *In-progress*.

Relative Contributions:

S. Mekhiel:	Conceptualization, Methodology, Experimental work, Investigation, Writing -original draft preparation, Writing -review & editing.
M.A. Balbaa:	Experimental work, Writing -review & editing.
M. A. Elbestawi:	Supervision, Conceptualization, Writing -review & editing.
Philip Koshy:	Supervision, Conceptualization, Writing -review & editing.
Lloyd Hackel:	Experimental work, Writing -review & editing.

Abstract

Additive Manufacturing (AM) technologies have attained an influential role in the manufacturing realm by offering unprecedented design freedom. However, undesirable tensile Residual Stress (RS) formation has manifested a major inherent challenge to expand the application envelope of the AM parts. This research explored the efficacy of Laser Peening (LP) as a post-processing approach to mitigate the tensile RS and further induce compressive RS in the AM peened components. The impact of each LP parameter on the resulted RS, surface roughness, hardness, wear resistance, and contact angle was statistically analyzed. In addition, various power density levels were investigated, and the role of the ablative layer was examined. By utilizing the LP on an AM metallic surface, compressive RS up to 470 Mpa, 40% increase in hardness and 50% wear volume reduction were achieved.

Keywords: Additive Manufacturing, Hardness, Laser Peening, Residual Stresses, Selective Laser Melting. Square Spot Laser Peening, Surface Roughness, Wear.

4.1 Introduction

Over the past decade, Additive Manufacturing (AM) technologies have gained an increasing attention of scientists and engineers on account of their unprecedented flexibility. AM has eliminated the tooling constraints associated with the conventional manufacturing processes by consolidating the desired geometry layer by layer bottom-up. This approach has enabled the realization of highly customizable components with the most complex geometries once impossible to manufacture conventionally. Such capabilities have reduced the number of constituent parts eliminating the time and cost associated with the assembly process in addition to the tooling and machine set-up. Accordingly, AM has reshaped the design for manufacturability concept into a broader functionality-based design [1]. A significant extent of AM research has focused on the process–structure–property paradigm improving the functionality of the AM products via controlling the process and the output structure [2]. Despite the efficacy of such an approach to achieve rapid development in AM technology, process control has not always been sufficient to enhance specific properties such as the Residual Stresses (RS).

The RS, in General, can be attributed to the spatial temperature gradient, the phase transformation effect, stress-inducing plastic deformation [3]. Since the steep temperature gradient is an inherent consequence of the deposition of molten metal on a relatively cooler substrate or prior deposited layers, temperature gradient has been considered the major contributor to the formation of tensile RS in AM components [4]. Such tensile RS is attributed to high thermal gradient, occasionally accompanied by phase transformation, leading to part distortion, delamination, the deterioration of the geometric tolerance, fatigue performance, micro and macro cracks formation, warping, and fracture resistance of the fabricated part [4-7]. With these problems, a better understanding of the evolution of thermal stresses during AM is essential to control and mitigate such issues and produce functional components. To this end, various RS measurement techniques have been reviewed, identifying each technique's spatial resolution, measurement depth, and estimated cost in [8]. Additionally, the RS has been assessed qualitatively for the AM processes by measuring the resulting deformation utilizing several artifacts, such as bridge [9] and cantilever structures [10].

Recently, researchers have attempted to adjust the resulted RS via regulating the AM process parameters. Some studies, such as a study on IN718, have found scattered RS data that could not be related directly to power, scanning speed, or hatch spacing. While other studies, such as one done on 316L, suggested a significant sensitivity of the RS to the used laser power [9]. Other studies have reported that increasing the baseplate thickness reduces the resulting RS in the fabricated part while the tensile RS increases with the part's height increase [4, 11]. Also, the RS has shown a drastic reduction after the removal of the parts off the baseplate. Additionally, higher yield strength materials have exhibited higher tensile RS in the same study [4].

Other parameters, such as dwell time between layers, have been investigated, which caused distortion and was found disadvantageous for the RS [12, 13]. Moreover, pre-heating the base plates has decreased the resulting tensile RS due to the lower temperature gradient [14]. Additionally, sector scanning with a shorter scanning track length has been reported to have the most significant impact on inducing lower tensile RS [9, 11].

While ideas like control the dwell time between layers, pre-heating the baseplate or increasing its thickness may present a potential solution for the RS challenge, their impact deteriorates quickly with increasing the fabricated part height. Such deterioration cannot be avoided given the lack of control over the part height rendering these ideas largely inapplicable for functional part manufacturing. Other approaches like thermal post-processing have been investigated to enhance the microstructure and relieve the RS [15, 16]. Such techniques have been adequate to eliminate the tensile RS globally. Still, they cannot directly treat any particular location of interest or induce a desirable compressive RS to the fabricated part. Shot Peening (SP) [17, 18] and Laser Peening (LP) [19] have shown the ability to induce a tremendous amount of compressive RS and to treat the more critical areas locally. The superiority of LP over SP in generating compressive RS into higher depth and to further enhance the treated part's fatigue resistance [20-22].

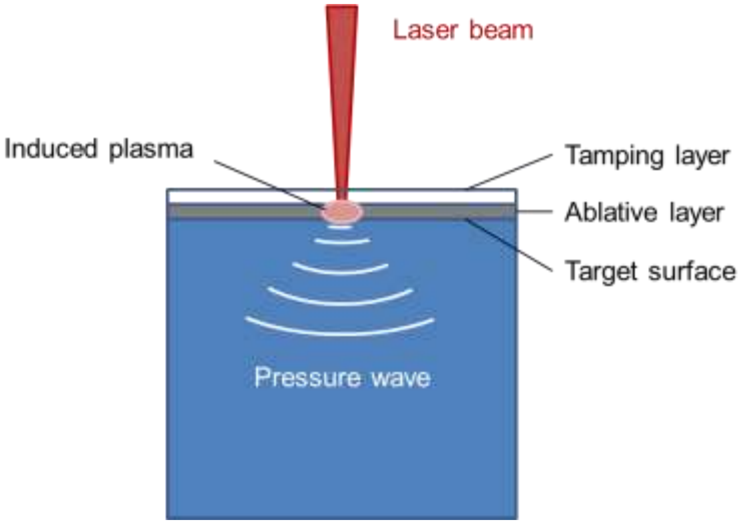

Fig. 4.1. Schematic of LP process in confined mode.

The LP technique is an innovative approach for surface treatment of metallic materials inducing desirable compressive RS and remarkably increasing the fatigue strength. In the LP process, the treated surface is shot by a very short-pulse laser, in order of nanoseconds, inducing vaporization of the excessively heated zone forming plasma by ionisation. After absorbing the rest of the pulse energy, the pressure generated by the plasma is transmitted to the material through pressure wave; this LP mode is known as "direct ablation mode". Treated surfaces are coated with a layer of opaque material, omitting the thermal effect of the laser to increase the pressure amplitude. Such layer is called an ablative layer in which black paint, Al tape or paint are used. To further increase the pressure directed to the treated surface, another transparent layer like distilled water or glass, named the tamping layer, is used to confine the resulted pressure wave propagation towards the targeted part [19]. Fig. 4.1 demonstrates a "confined mode" schematic in which both ablative and tamping layers are applied.

A limited number of studies have investigated the LP effect to improve the AM part properties. The LP has been reported to efficiently eliminate the surface and sub-surface porosity, increasing the overall strength of the printed AlSi10Mg samples [23]. Yet, the untreated deep pores still pose a threat as crack nucleation sites, diminishing fatigue strength. Tensile strength has shown a remarkable increase after peening, as demonstrated by [24, 25]. Moreover, the utilization of LP as a forming tool has been explored in another study [20]. Also, its impact on fatigue has been studied in [20, 26]. With the exceptions of wear [27] and crystallography [28] investigations, all other studies have focused on surface RS [24, 27, 29] or in-depth RS [30-33]. To the authors' knowledge, none of the aforementioned studies has investigated the impact of varying the power density level nor have attempted to optimise the utilized LP parameters. Therefore, the present work will use a statistical model to analyse the impact of each parameter, furthermore, it will explore the effect of varying the power density over a wide range on the resulted properties. In addition to investigating RS, the current study will extend the examination to envolve other properties such as surface roughness, hardness, wear resistance and Contact Angle (CA). Eventually, the influence of the utilization of the ablative layer will be studied.

4.2 Experimental

4.2.1 Material and process parameters

Samples were manufactured using an EOS M280 SLM machine equipped with a continuous ytterbium fibre laser with 400 W maximum power. The printing was executed in a nitrogen environment with a controlled oxygen level below 0.13% to minimize the oxidation possibility. An AISI 316L stainless steel gas atomized powder with a particle size of 15–45 μm was used as a feedstock. Manufacturer recommended process parameters of 285 W laser power, 960 mm/s scanning speed, 0.04 mm layer thickness and 0.11 mm hatch spacing were used. The maximum stripe width of 100 mm was maintained, placing the samples to avoid the stripe overlap location. Samples had a rectangular shape with dimensions of 50×10 mm and a building height of 10 mm. To evaluate the impact of scanning track length on the resulted residual stresses, scanning was kept parallel to the long edge of 50 mm (sample L) and the short edge of 10 mm (sample S) and compared to baseline (sample B) as shown in Fig. 4.2. An orientation of 67° between successive layers was adopted for all printed samples except for S and L samples, where no orientation was applied. All samples were cut off the baseplate using wire electrical discharge machining (WEDM).

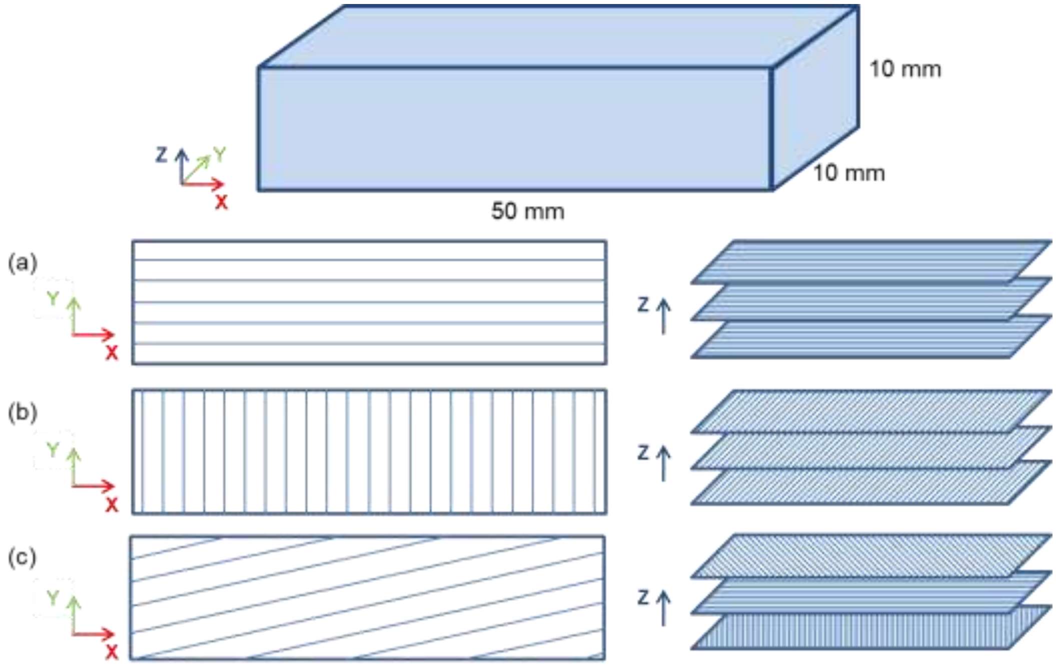

Fig. 4.2. Laser scanning with 0° orientation between successive layer (a) L sample (b) S sample and (c) B sample with 67° orientation.

4.2.2 Laser Peening

To assess the impact of LP parameters on the resulted RS, three parameters were investigated: the spot size, pulse energy, and the number of peening layers. A full factorial design of experiment (DOE) would require 27 sets of parameters to explore three levels of each parameter. However, using Taguchi DOE, the sample number needed to study three parameters with three levels was reduced to 9 runs shown in Table 4.1. Given that the pulse length was kept constant at 23 ns, the power density can be calculated using the following formula (*Power density = Pulse energy / (Pulse length×Spot Area)*). The DOE resulted in a wide range of irradiances ranging between 0.4 to 10.5 GW/cm^2 (Table 4.1). Square laser spots were used for peening the samples, and the edge length represented the spot size. An offset of 50% in both *x* and *y* directions was applied between successive LP layers. The overlap between spots was maintained at 3% on each layer. A thin layer (typically 1 mm in thickness) of deionized water was used as a tamping layer. A 350 µm thick Aluminum tape 3M-427 was applied to the target surfaces as an ablative layer before each peening layer. These targeted surfaces were finished to approximately 1 µm *R*a prior to peening for the ablative tape to hold up and ensure complete contact between the tape and the target surface. An additional sample (sample 10) was LPed without applying the ablative layer with parameter set (sample 3) associated with the highest power density.

Table 4.1. L9 Orthogonal array for LP parameters.

Sample No.	Spot size (mm)	Pulse energy (J)	No. of Layers	Power Density (GW/cm^2)
1	2.5	5	1	3.5
2	2.5	10	2	6.9
3	2.5	15	3	10.4
4	5	5	2	0.9
5	5	10	3	1.7
6	5	15	1	2.6
7	7.5	5	3	0.4
8	7.5	10	1	0.8
9	7.5	15	2	1.2

4.2.3 Characterization

A non-destructive Archimedes method was used to measure the density of samples [34]. Samples masses were measured at least three times in the air (m_{air}) and submerged in distilled water (m_{fluid}) with a digital balance with a resolution of 0.1 mg. The reported density was calculated using $\rho_r=(m_{air}/(m_{air}–m_{fluid})).(\rho_{fl}/\rho_{bulk})$ and it is relative to the density of 316L stainless steel (ρ_{bulk} = 7970 kg/m^3). RS were measured non-destructively on the treated *xy* plane using X-Ray Diffraction (XRD) measurements. The reported results were the principle stresses measured at the centre of each coupon of the (311) diffractive plane using 11 beta tilts (total measurements) from the collimator. The Bragg angle is 152 degrees using an Mn irradiation tube for the Ni alloy. The error is calculated using both left/right detectors on the XRD tool to fit the 11 beta tilt measurements onto a Gaussian curve. Surface roughness was measured in terms of the *R*a parameter based on at least six measurements with a stylus profilometer.

Micro-hardness was measured via an automatic Clemex CMT microhardness tester in *z* directions. An average of five indentations with 200 gf load for each surface were reported. The exact number of indentations was used in *xy* plane, and the average Rockwell hardness was reported using 100 kgf load on a 1/16" Tungsten carbide ball following ASTM E18 standard [35]. The static CA for 5 µL Milli-Q water droplets was measured optically on at least five different locations on the top surface. The Axisymmetric Drop Shape Analysis (ADSA) fitting method was used to acquire the CA value [36]. The measurements were undertaken at least three weeks after the probable temporal evolution of CA associated with printing or treatment [37].

A standard tribometer (Anton Paar® TRB3) was used to perform dry sliding tests in a linearly reciprocating ball-on-flat configuration, following the procedure of ASTM G133 standard [38]. The counterface was a 6 mm diameter Al_2O_3 ball with a microhardness exceeding 1700 HV. Before tribological testing, all surfaces were cleaned thoroughly using ethanol and air-dried. The stroke length, load, frequency, and testing distance were 10 mm, 10 N, 5 Hz, and 100 m, respectively. The testing was executed at a temperature of 23 ± 2 °C with a humidity of 25 ± 5 %. The volume loss was calculated based on wear scar analysis, and alternatively, the mass loss was determined by measuring weight difference using a scale with a resolution of 0.1 mg. Samples were cleaned in an ultrasonic ethanol bath for at least 30 min and then air-dried before weighing. Built coupons and wear tracks were examined using optical and scanning electron microscopy.

4.3 Results and Discussion

4.3.1 Scanning length impact on AM parts

Multiple parameters may contribute to the SLM process's tensile RS formation, such as baseplate thickness, pre-heating, part height, laser power, speed, scanning strategy, and scanning track length. As discussed in (sec 4.1), changing some of these parameters may have a limited impact or not be a viable option. Three samples, S, L, and B, were printed to assess how changing the scanning track length affects the RS formation. B sample had 67° orientation between successive layers, thus track length and direction changed layer to layer. In contrast, S and L samples were built with zero orientation between layers keeping the track length constant at 10 and 50 mm in S and L, respectively. Fig. 4.3a, d shows the deteriorated topography of the top surfaces of S and L samples. Warping at the edges at the end of the tracking scans was observed. Fig. 4.3b demonstrates the bulge at the side edge of the S sample, while Fig. 4.3e shows the absence of warping parallel to the scanning track. A lower edge warping was observed in sample B at all edges in line with [7]. At the same time, the location of warping at the end of scan tracks was also reported in [11].

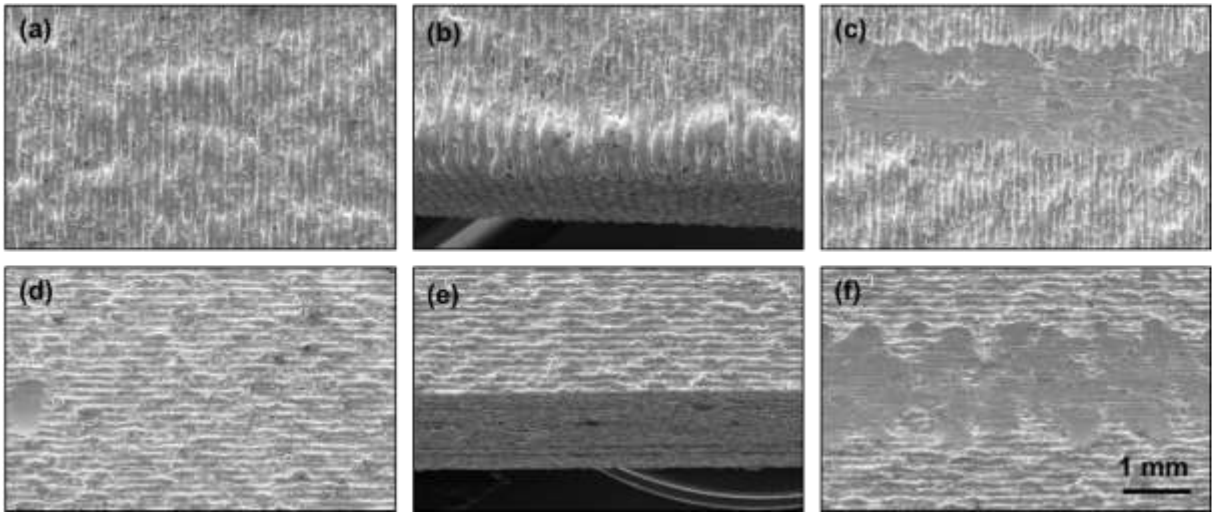

Fig. 4.3. Top surface, side edge, and wear scar for (a,b,c) S (d,e,f) L samples.

Aside from the apparent shape deformity, the relative density for the B sample was approximately 99%, but it dropped dramatically to 86% and 91%for S and L. By investigating the cross-section of the samples, it was evident that parts without successive layer orientations suffered from higher porosity (Fig. 4.4). Additionally, the hardness of the B, S, and L samples was 91.3, 79.6, and 85.3 HRBW, respectively. The wear volume of the three samples was explored; S had the highest wear volume of 9.5 $\times 10^{-4}$ mm^3 while L and B were 7.4 and 6.6 $\times 10^{-4}$ mm^3. For the part printed with shorter tracks, despite the potential tensile RS decrease, the part suffered from higher warping, porosity and lower hardness and wear resistance. The deterioration of properties occurs in both cases of short and long tracks. Therefore, such decline in properties may not be solely attributed to the scanning track length but the lack of orientation between successive layers.

Consequently, it can be concluded that controlling the scanning track length will not be beneficial to eliminate the tensile RS of the AM parts. Thus, the next section will discuss post-processing by LP to eliminate tensile and induce compressive RS to the treated parts. The sample fabricated with manufacturer recommended process parameters and 67° orientation between layers (sample B) will be used as a baseline for the upcoming LP analyses.

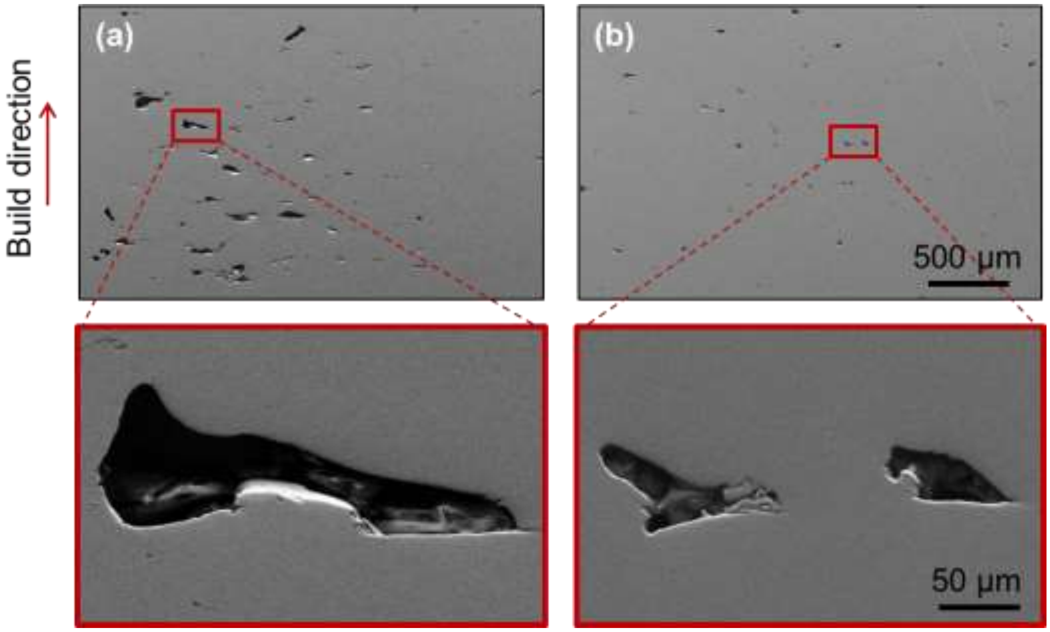

Fig. 4.4. SEM image showing the porosity in (a) S (b) L samples.

4.3.2 LP parameters analysis

With the exception of [20], All the LP research mentioned in the literature (sec 4.1) have used circular laser spots. The square-spot laser has the ability to achieve better area coverage without overlap compared to a circular one. The impact of changing the spot overlapping and the scanning path were investigated for square-spot LP of AISI 316L stainless steel blades [39]. However, these will be beyond the scope of this study as the overlap will be kept constant at 3%, and the scanning strategy will not be changed. The Square-spot LPed surfaces have exhibited a more homogeneous RS field than those peened using circular spots [40]. Such homogeneity is highly expected in our treated samples as the utilized laser has a high spatial intensity uniformity. However, the RS values are only indicative, and they represent the principal RS at a single mid-point on the top surface of the samples. All the acquired results for various responses along with control parameters are listed in Table 4.2.

Table 4.2. Measured properties for the LP samples.

Sample No.		1	2	3	4	5	6	7	8	9	10
Spot size	(mm)	2.5	2.5	2.5	5	5	5	7.5	7.5	7.5	2.5
Pulse energy	(J)	5	10	15	5	10	15	5	10	15	15
No. of Layers		1	2	3	2	3	1	3	1	2	3
Power Density	(GW/cm^2)	3.5	6.9	10.4	0.9	1.7	2.6	0.4	0.8	1.2	10.4
RS	(MPa)	-252	-473	-367	46	-341	-195	118	50	-60	621
Error	(MPa)	14.1	13.9	15.4	12.7	12.5	16.0	14.8	12.3	15.6	24.4
*R*a	(µm)	1.35	1.48	1.83	0.94	1.38	1.38	1.11	1.38	1.34	2.41
σ	(µm)	0.10	0.23	0.13	0.06	0.19	0.16	0.13	0.20	0.09	0.08
Hardness (HRBW)		99.3	102	105	93	98.9	98.9	94.5	95.3	95.8	100
σ	(HRBW)	1.11	1.12	1.55	1.82	0.63	0.25	1.03	0.55	1.99	4.93
Wear volume	(mm^3×10^{-4})	5.01	3.96	2.69	5.51	5.26	5.01	6.02	5.76	5.51	5.76
σ	(mm^3×10^{-4})	0.67	0.33	0.43	0.27	0.9	0.17	0.3	0.63	0.17	0.33
CA	(°)	70	86	84	81	56	80	68	79	91	102
σ	(°)	1.9	13	4.2	3.1	5.3	6.7	9.3	9.1	5.2	1

The surface roughness generated by the LP is heavily dominated by the spot shape and the phase condition of the laser beam. Unlike the commonly used single lens LP system, the used LP system utilizes a laser with a highly controlled phase and relay images of the beam onto the target. While if the peening system does not image relay the beam to the target, the beam intensity on the surface being peened becomes the Fourier transform of the phase profile of the laser output or the wavefront. Also, this may depend on whether the laser pulses were applied while the laser gain media was cold or hot. And the quality of the optics in the laser and in relaying the beam to the target. Therefore, the surface roughness results reported in this work are indicative of the outputs of the investigated laser and optics and cannot be generalized to other LP systems outcomes. Generally, the intensity distribution of the LP at the targeted surfaces will highly determine the generated surface roughness. The superior spatial intensity uniformity of the used system laser spot and the high level of laser phase control ensured the lower possible impact on the surface roughness. While the surface roughness exhibited moderate variations and the CA data was scattered, the RS, hardness and wear resistance show a remarkable increase after the LP.

Fig. 4.5 presents the main effects plot of means for the various measured properties. The spot size demonstrates the highest impact on the means of RS, hardness, and wear volume. Decreasing the spot size increased the hardness, wear resistance and the induced compressive residual stresses drastically. The pulse energy exhibited a more significant influence on the surface roughness, yet as explained, the roughness did not show substantial changes. Table 4.3 represents the Analysis of Variance (ANOVA) and the complete regression data for the RS, Ra, hardness, wear volume, and CA. Additionally, the least sensitivity of all responses means was associated with the number of layers.

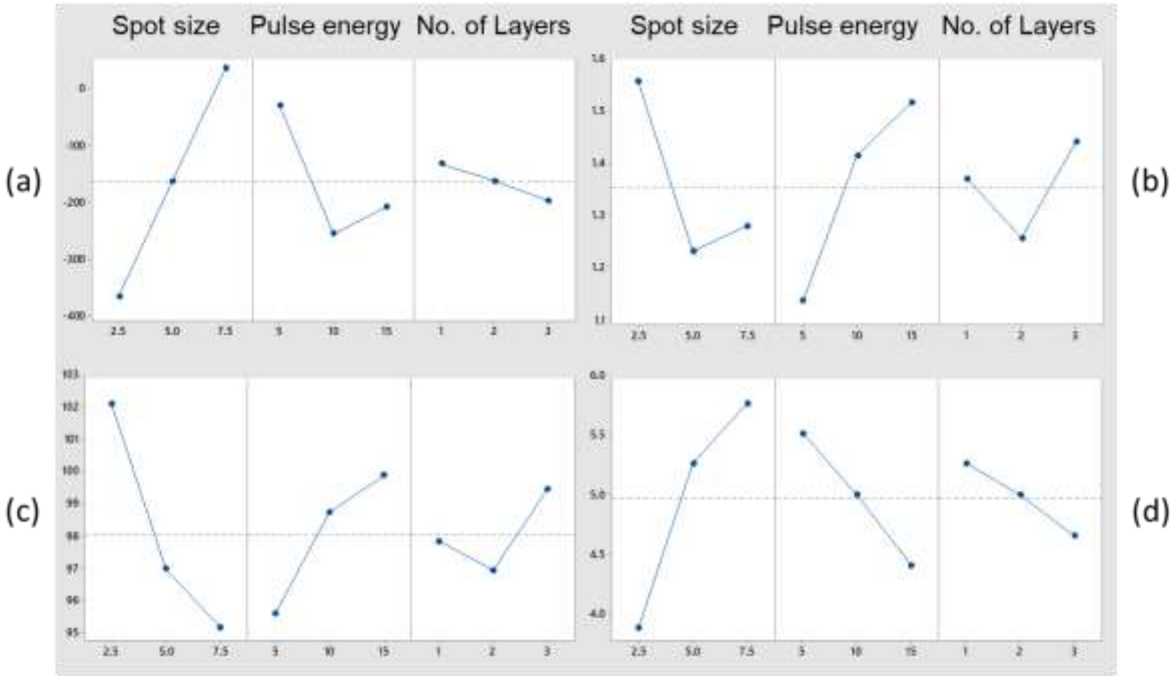

Fig. 4.5. Main effects plots for means for (a) RS (b) *R*a (c) hardness and (d) wear volume.

Table 4.3. ANOVA and regression analysis for individual LP parameters.

Source	Degrees of freedom	Sum of squares	Mean of sum of squares	F-Value	P-Value
			RS		
Regression	3	293734	97911	7.74	0.025
Spot Size	1	240000	240000	18.98	0.007
Pulse Energy	1	47526	47526	3.76	0.110
No. of Layers	1	6208	6208	0.49	0.515
Error	5	63225	12645		
Total	8	356960			

Regression equation:

RS = – 321 + 80 Spot size – 17.8 Pulse energy – 32.2 No. of layers

S = 112.45 R^2 = 82.29 % Adjusted R^2 = 71.66 % Predicted R^2 = 46.42 %

***R*a**

Regression	3	0.335866	0.111955	4.21	0.078
Spot Size	1	0.113438	0.113438	4.27	0.094
Pulse Energy	1	0.215020	0.215020	8.08	0.036
No. of Layers	1	0.007408	0.007408	0.28	0.620
Error	5	0.132982	0.026596		
Total	8	0.468848			

Regression equation:

*R*a = 1.182 – 0.055 Spot size + 0.0379 Pulse energy + 0.0351 No. of layers

S = 0.163084 R^2 = 71.64 % Adjusted R^2 = 54.62 % Predicted R^2 = 6.76 %

Hardness

Regression	3	103.042	34.347	12.19	0.010
Spot Size	1	71.645	71.645	25.43	0.004
Pulse Energy	1	27.449	27.449	9.74	0.026
No. of Layers	1	3.947	3.947	1.40	0.290
Error	5	14.087	2.817		
Total	8	117.128			

Regression equation:

Hardness = 99.09 – 1.382 Spot size + 0.428 Pulse energy + 0.811 No. of layers

S = 1.6785 R^2 = 87.97 % Adjusted R^2 = 80.76 % Predicted R^2 = 64.73 %

Wear volume

Regression	3	7.6842	2.5614	13.55	0.008
Spot Size	1	5.2848	5.2848	27.96	0.003
Pulse Energy	1	1.8452	1.8452	9.76	0.026
No. of Layers	1	0.5542	0.5542	2.93	0.147
Error	5	0.9449	0.1890		
Total	8	8.6292			

Regression equation:

Wear volume = 4.812 + 0.3754 Spot size – 0.1109 Pulse energy – 0.304 No. of layers

S = 0.43473 R^2 = 89.05 % Adjusted R^2 = 82.48 % Predicted R^2 = 59.37 %

CA

Regression	3	295.815	98.605	0.80	0.546
Spot Size	1	1.105	1.105	0.01	0.928
Pulse Energy	1	213.308	213.308	1.72	0.246
No. of Layers	1	81.402	81.402	0.66	0.454
Error	5	619.173	123.835		
Total	8	914.988			

Regression equation:

CA = 73.4 – 0.17 Spot size + 1.192 Pulse energy – 3.68 No. of layers

S = 11.1281 R^2 = 32.33 % Adjusted R^2 = 0 % Predicted R^2 = 0 %

4.3.3 The impact of power density

Since Fig. 4.5 indicated that the number of peening layers had the most negligible impact on the investigated properties. Thus, the effect of the power density, the term combining laser spot size and energy, is further explored in Fig. 4.6. The induced compressive RS increased dramatically with the increase of the power density (Fig. 4.6a). Expectedly, with the rise of energy applied to the surface, the higher pressure wave is transmitted to the surface, increasing the compressive RS. A similar trend was observed for hardness and wear resistance in Fig. 4.6c, d, as the increased pressure causes enhancement of the microstructure advancing the hardness and consequently the wear resistance. While in Fig. 4.6b, surface roughness increased yet with much less sensitivity what may be attributed to the laser uniformity mentioned above. The linear regression equations for the trendlines used in Fig. 4.6 are indicated in Table 4.4. On the other hand, the CA has not shown a significant variation with the power density change. As the CA is mainly affected by the surface's topography and chemical composition, the samples did not undergo any changes to the surface chemical composition. Such scattered CA variation may be related to the insignificance of the topography variation.

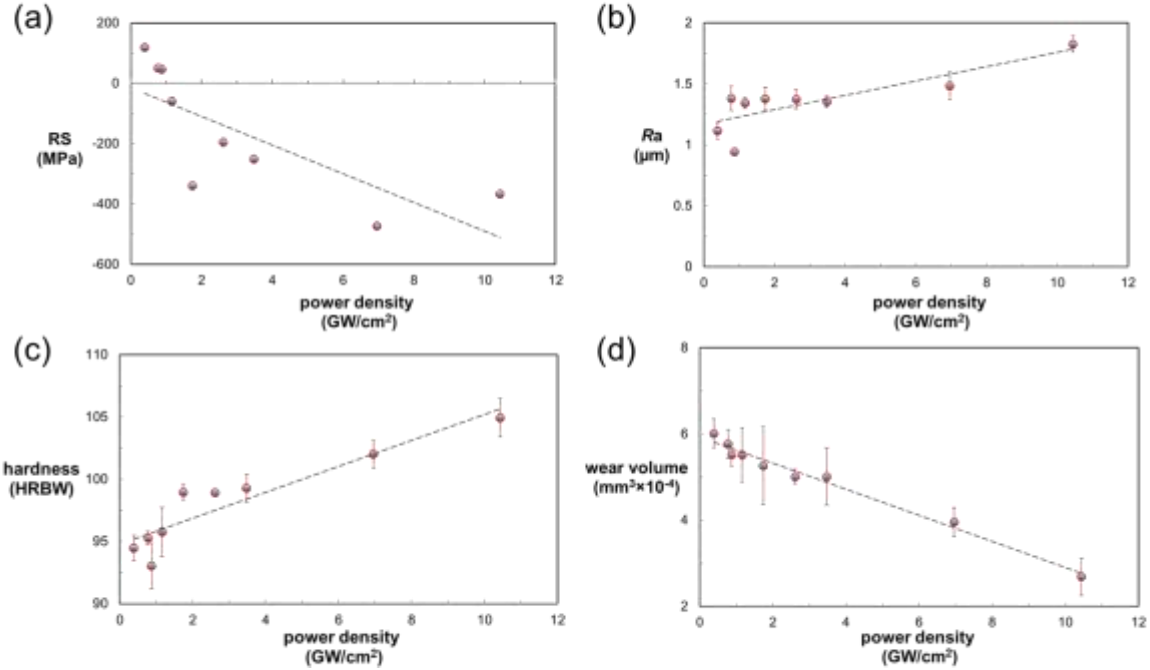

Fig. 4.6. The evolution of (a) RS (b) *R*a (c) hardness (d) wear volume with power density in confined mode LP.

Table 4.4. Linear regression for power density and various responses.

Linear regression equation	R^2
RS = – 47.557 × power density – 13.732	0.5851
*R*a = 0.059 × power density + 1.1693	0.6854
hardness = 1.0424 × power density + 94.784	0.8573
wear volume = – 0.3029 × power density + 5.9276	0.9822

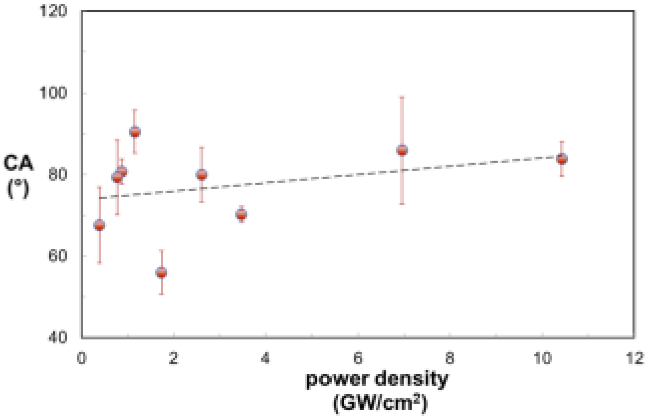

Fig. 4.7. The evolution of CA with power density in confined mode LP.

4.3.4 Impact of ablative layer

The efficacy of the ablative layer was investigated by LP using the highest level of power density with and without applying the Al tape. Expectedly, removing the ablative layer exposed the treated surface to the peening process's thermal effect. As a result, a thin recast layer formed on the surface, as shown in Fig. 4.8. The surface RS of the LPed surface without ablative coating was remarkably high tensile RS of 621 Mpa. Such measurements are expected as the XRD penetration depth does not exceed the recast layer thickness. Similarly, the wear volume was twice (5.7×10^{-4} mm^3) the value for the surface peened with an ablative coating (2.7×10^{-4} mm^3) which can be related to the presence of porous and low strength recast layer. However, as an indication of the impact of the peening in-depth, a hardness profile was measured on the cross-section starting 50 microns from the treated surface (Fig. 4.9). The in-depth micro-hardness value indicates that the pressure wave is higher using the ablative layer as it gained higher hardness than the peened surface without the ablative coating.

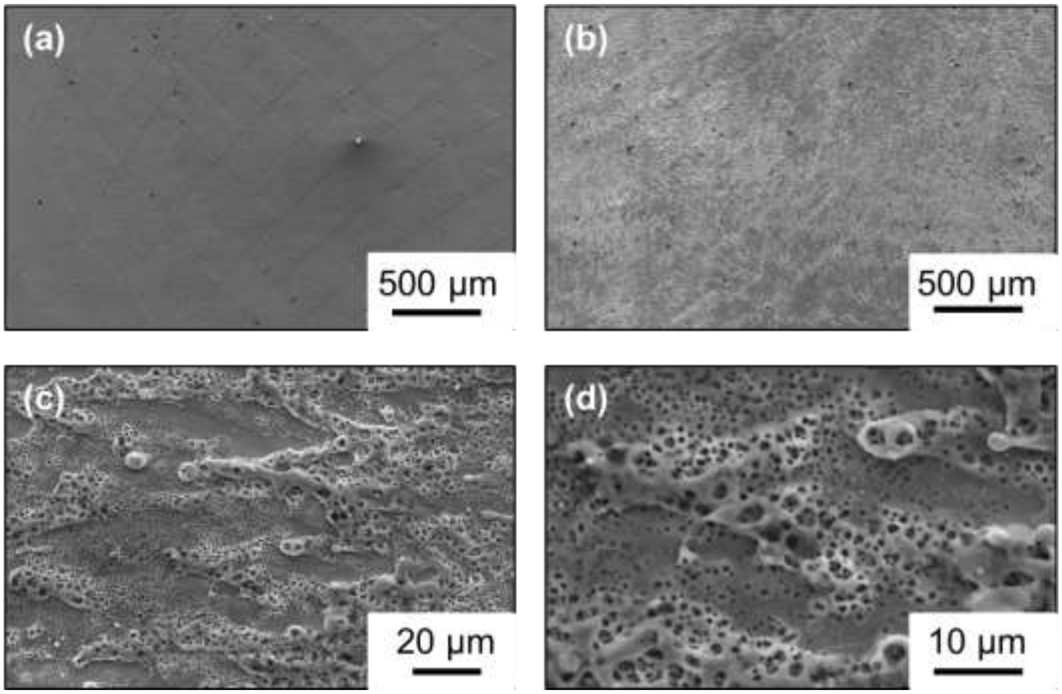

Fig. 4.8. Peened surface (a) with ablative layer (b, c, d) without ablative layer.

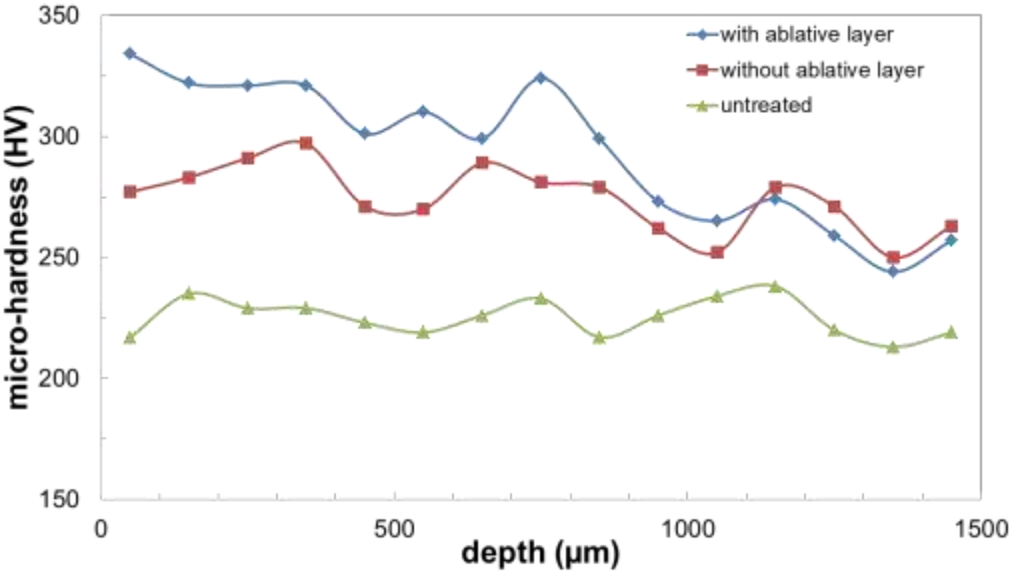

Fig. 4.9. Micro-hardness depth profile for the unpeened and peened surfaces with and without ablative layer.

The sample peened without applying the ablative coating exhibited a significant increase in CA to reach 102° compared to the average CA of 80° for the samples LPed with ablative coating. Such CA increase may be attributed to the topography change indicated in Fig. 4.8c, d, along with the potential chemical composition variation due to the ablation process. Therefore, it can be concluded that the surface properties are better in the LP with an ablative layer. Yet, LP was successful in enhancing the hardness inside the material. Although the recast layer is usually removed before rendering the part functional, the ablative coating induced more superior properties in the treated surface.

4.4 Conclusions

With a view to mitigating the tensile RS challenge for the AM parts, the present work explored LP as a post-processing candidate leading to the following conclusions:

- Controlling the scanning track length did not lead to significant changes in RS, yet, other challenges arise, such as higher porosity and apparent warping.
- The utilization of LP with higher power density successfully reduced the tensile RS and induced compressive RS up to 471 Mpa. Also, hardness was increased by 40 %, and the wear volume was decreased by 50 %.
- Surface roughness is highly affected by the spatial uniformity of the used laser.
- The laser spot size greatly influenced the investigated responses, while the peening layers number had the slightest significance.
- The power density was the critical factor to control the desired outcome.
- The removal of the ablative layer lessens the impact of the LP on the target surface.
- A high tensile RS recast layer occurs when performing LP without an ablative coating, increase the CA for its porous topography.

The LP demonstrated exceptional potential to boost all the investigated properties promoting it as a viable tool to post-process AM components into functional parts.

Acknowledgement

This work was funded in part by the Natural Sciences and Engineering Research Council (NSERC) of Canada.

References

[1] T. DebRoy, H. Wei, J. Zuback, T. Mukherjee, J. Elmer, J. Milewski, *et al.*, "Additive manufacturing of metallic components–process, structure and properties," *Progress in Materials Science,* vol. 92, pp. 112-224, 2018.

[2] M. Yakout, M. A. Elbestawi, and S. C. Veldhuis, "Density and mechanical properties in selective laser melting of Invar 36 and stainless steel 316L," *Journal of Materials Processing Technology,* vol. 266, pp. 397-420, 2019/04/01/ 2019.

[3] T. DebRoy, H. L. Wei, J. S. Zuback, T. Mukherjee, J. W. Elmer, J. O. Milewski, *et al.*, "Additive manufacturing of metallic components – Process, structure and properties," *Progress in Materials Science,* vol. 92, pp. 112-224, 2018/03/01/ 2018.

[4] P. Mercelis and J.-P. Kruth, "Residual stresses in selective laser sintering and selective laser melting," *Rapid prototyping journal,* vol. 12, pp. 254-265, 2006.

[5] K. Kempen, L. Thijs, B. Vrancken, S. Buls, J. Van Humbeeck, and J. Kruth, "Producing crack-free, high density M2 Hss parts by selective laser melting: pre-heating the baseplate," in *Proc. 24th Int. Solid Free. Fabr. Symp*, 2013, pp. 131-139.

[6] G. K. Lewis and E. Schlienger, "Practical considerations and capabilities for laser assisted direct metal deposition," *Materials & Design,* vol. 21, pp. 417-423, 2000.

[7] M. Balbaa, S. Mekhiel, M. Elbestawi, and J. McIsaac, "On selective laser melting of Inconel 718: Densification, surface roughness, and residual stresses," *Materials & Design,* vol. 193, p. 108818, 2020/08/01/ 2020.

[8] G. S. Schajer and C. O. Ruud, "Overview of residual stresses and their measurement," *Practical residual stress measurement methods. 1st Edition. Hoboken: John Wiley & Sons,* pp. 1-27, 2013.

[9] J. Hajnys, M. Pagáč, J. Měsíček, J. Petru, and M. Król, "Influence of Scanning Strategy Parameters on Residual Stress in the SLM Process According to the Bridge Curvature Method for AISI 316L Stainless Steel," *Materials,* vol. 13, p. 1659, 2020.

[10] L. Papadakis, A. Loizou, J. Risse, S. Bremen, and J. Schrage, "A computational reduction model for appraising structural effects in selective laser melting manufacturing," *Virtual and Physical Prototyping,* vol. 9, pp. 17-25, 2014/01/02 2014.

[11] Y. Liu, Y. Yang, and D. Wang, "A study on the residual stress during selective laser melting (SLM) of metallic powder," *The International Journal of Advanced Manufacturing Technology,* vol. 87, pp. 647-656, 2016.

[12] E. R. Denlinger, J. C. Heigel, P. Michaleris, and T. Palmer, "Effect of inter-layer dwell time on distortion and residual stress in additive manufacturing of titanium and nickel alloys," *Journal of Materials Processing Technology,* vol. 215, pp. 123-131, 2015.

[13] S. Y. Ivanov, A. Vildanov, P. A. Golovin, A. Artinov, and I. Karpov, "Effect of Inter-Layer Dwell Time on Distortion and Residual Stresses of Laser Metal Deposited Wall," in *Key Engineering Materials,* 2019, pp. 445-451.

[14] C. Li, Z. Liu, X. Fang, and Y. Guo, "Residual stress in metal additive manufacturing," *Procedia CIRP,* vol. 71, pp. 348-353, 2018.

[15] A. H. Maamoun, M. Elbestawi, G. K. Dosbaeva, and S. C. Veldhuis, "Thermal post-processing of AlSi10Mg parts produced by Selective Laser Melting using recycled powder," *Additive Manufacturing,* vol. 21, pp. 234-247, 2018/05/01/ 2018.

[16] M. Wang, B. Song, Q. Wei, Y. Zhang, and Y. Shi, "Effects of annealing on the microstructure and mechanical properties of selective laser melted AlSi7Mg alloy," *Materials Science and Engineering: A,* vol. 739, pp. 463-472, 2019/01/02/ 2019.

[17] B. AlMangour and J.-M. Yang, "Improving the surface quality and mechanical properties by shot-peening of 17-4 stainless steel fabricated by additive manufacturing," *Materials & Design,* vol. 110, pp. 914-924, 2016/11/15/ 2016.

[18] B. AlMangour and J.-M. Yang, "Integration of Heat Treatment with Shot Peening of 17-4 Stainless Steel Fabricated by Direct Metal Laser Sintering," *JOM,* vol. 69, pp. 2309-2313, 2017/11/01 2017.

[19] K. Ding and L. Ye, *Laser shock peening: performance and process simulation*: Woodhead Publishing, 2006.

[20] L. Hackel, J. R. Rankin, A. Rubenchik, W. E. King, and M. Matthews, "Laser peening: A tool for additive manufacturing post-processing," *Additive Manufacturing,* vol. 24, pp. 67-75, 2018.

[21] P. P. Shukla, P. T. Swanson, and C. J. Page, "Laser shock peening and mechanical shot peening processes applicable for the surface treatment of technical grade ceramics: A review," *Proceedings of the Institution of Mechanical Engineers, Part B: Journal of Engineering Manufacture,* vol. 228, pp. 639-652, 2014/05/01 2013.

[22] C. A. Rodopoulos, J. S. Romero, S. A. Curtis, E. R. de los Rios, and P. Peyre, "Effect of controlled shot peening and laser shock peening on the fatigue performance of 2024-T351 aluminum alloy," *Journal of Materials Engineering and Performance,* vol. 12, pp. 414-419, 2003/08/01 2003.

[23] A. Du Plessis, D. Glaser, H. Moller, N. Mathe, L. Tshabalala, B. Mfusi*, et al.*, "Pore closure effect of laser shock peening of additively manufactured AlSi10Mg," *3D Printing and Additive Manufacturing,* vol. 6, pp. 245-252, 2019.

[24] J. Lu, H. Lu, X. Xu, J. Yao, J. Cai, and K. Luo, "High-performance integrated additive manufacturing with laser shock peening–induced microstructural evolution and improvement in mechanical properties of Ti6Al4V alloy components," *International Journal of Machine Tools and Manufacture,* vol. 148, p. 103475, 2020.

[25] W. Guo, R. Sun, B. Song, Y. Zhu, F. Li, Z. Che, *et al.*, "Laser shock peening of laser additive manufactured Ti6Al4V titanium alloy," *Surface and Coatings Technology,* vol. 349, pp. 503-510, 2018/09/15/ 2018.

[26] S. Luo, W. He, K. Chen, X. Nie, L. Zhou, and Y. Li, "Regain the fatigue strength of laser additive manufactured Ti alloy via laser shock peening," *Journal of Alloys and Compounds,* vol. 750, pp. 626-635, 2018.

[27] A. N. Jinoop, S. K. Subbu, C. P. Paul, and I. A. Palani, "Post-processing of Laser Additive Manufactured Inconel 718 Using Laser Shock Peening," *International Journal of Precision Engineering and Manufacturing,* vol. 20, pp. 1621-1628, 2019/09/01 2019.

[28] N. Kalentics, K. Huang, M. O. V. de Seijas, A. Burn, V. Romano, and R. E. Logé, "Laser shock peening: a promising tool for tailoring metallic microstructures in selective laser melting," *Journal of Materials Processing Technology,* vol. 266, pp. 612-618, 2019.

[29] N. N. Kumar, A. C. Yadav, K. Raja, S. Prabhakaran, C. D. Naiju, and S. Kalainathan, "Study on Effect of Laser Peening on Inconel 718 Produced by DMLS Technique," SAE Technical Paper 0148-7191, 2019.

[30] N. Kalentics, E. Boillat, P. Peyre, S. Ćirić-Kostić, N. Bogojević, and R. E. Logé, "Tailoring residual stress profile of Selective Laser Melted parts by Laser Shock Peening," *Additive Manufacturing,* vol. 16, pp. 90-97, 2017/08/01/ 2017.

[31] N. Kalentics, A. Burn, M. Cloots, and R. E. Logé, "3D laser shock peening as a way to improve geometrical accuracy in selective laser melting," *The International Journal of Advanced Manufacturing Technology,* vol. 101, pp. 1247-1254, 2019/04/01 2019.

[32] N. Kalentics, E. Boillat, P. Peyre, C. Gorny, C. Kenel, C. Leinenbach*, et al.*, "3D Laser Shock Peening – A new method for the 3D control of residual stresses in Selective Laser Melting," *Materials & Design,* vol. 130, pp. 350-356, 2017/09/15/ 2017.

[33] R. Sun, L. Li, Y. Zhu, W. Guo, P. Peng, B. Cong, *et al.*, "Microstructure, residual stress and tensile properties control of wire-arc additive manufactured 2319 aluminum alloy with laser shock peening," *Journal of Alloys and Compounds,* vol. 747, pp. 255-265, 2018.

[34] A. B. Spierings and G. Levy, "Comparison of density of stainless steel 316L parts produced with selective laser melting using different powder grades," in *Proceedings of the Annual International Solid Freeform Fabrication Symposium*, 2009, pp. 342-353.

[35] A. International, "ASTM E18-20, Standard Test Methods for Rockwell Hardness of Metallic Materials," ed. West Conshohocken, PA: ASTM international, 2020.

[36] Z. N. Xu, "An algorithm for selecting the most accurate protocol for contact angle measurement by drop shape analysis," *Review of Scientific Instruments,* vol. 85, p. 125107, 2014.

[37] C. Guo, P. Koshy, F. Coelho, and P. R. Selvaganapathy, "Sink electrical discharge machining of hydrophobic surfaces," *CIRP Annals,* vol. 68, pp. 185-188, 2019.

[38] A. International, "ASTM G133-05, Standard Test Method for Linearly Reciprocating Ball-on-Flat Sliding Wear," ed. West Conshohocken, PA: ASTM international, 2016.

[39] G. Xu, K. Luo, F. Dai, and J. Lu, "Effects of scanning path and overlapping rate on residual stress of 316L stainless steel blade subjected to massive laser shock peening treatment with square spots," *Applied Surface Science,* vol. 481, pp. 1053-1063, 2019.

[40] Y. Hu, C. Gong, Z. Yao, and J. Hu, "Investigation on the non-homogeneity of residual stress field induced by laser shock peening," *Surface and Coatings Technology,* vol. 203, pp. 3503-3508, 2009/08/25/ 2009.

Chapter 5

Conclusions and Future Work

By virtue of having advantages such as design freedom, process flexibility, customization, constituent part reduction, reduction of lead time associated with tooling and assembly, Additive Manufacturing (AM) technologies have been presented as the face of the future of the advanced manufacturing realm. However, some challenges have been identified, compromising the functionality of the AM components. The present work focused on two major inherent challenges of the AM: the inferior surface quality and the tensile Residual Stresses (RS). The first phase has worked around the surface quality challenge by introducing the novel concept of Additive Texturing (AT) to enhance certain functionalities. On the other hand, the second phase investigated the Laser Peening (LP) to mitigate the tensile RS problem and further induce compressive RS in the targeted AM component.

5.1 Conclusions

The SLM process limitations were investigated to realize intricate micro-features and how the process parameters may affect these limitations. Also, the impact of the relatively higher surface roughness on the fabricated textures was examined. Additionally, properties like hydrophobicity and tribological response, especially under dry sliding conditions, were adequately explored. However, conclusions can be drawn from **the first phase of research** as follows:

- The volumetric energy density highly impacted the roughness of the top surface. Yet, Contact Angle (CA) exhibited minimal variation (80°–100°) for the five-fold change in roughness in terms of the *Ra* parameter.
- The wettability and surface roughness of the side walls were less sensitive to the process parameters variations due to the adhering partially melted powder particles.
- A minimum protruding feature width of 100–150 μm, equivalent to the single track width, was indicated for a continuous laser SLM.
- For consistent texture dimensions with the SLM dimensional limitations, channel arrays showed more reproducibility and fewer defects than pillar arrays and re-entrant channel patterns.
- The highest CA of ~136° was associated with the channel patterns for the top surface textures.
- Due to the hierarchical dual-scale structure arising from the adherence of partially molten metal powder, the channel patterns on the side surface further enhanced the CA by about 10°.
- AT surfaces achieved a CA of up to 141°, significantly increased over the as-built surfaces` (80°–100°) CA range.

- AM samples exhibited higher hardness and finer microstructure compared to the cold-rolled samples leading to a 12% and 7% reduction in Coefficient of Friction (CoF) and specific wear rates, respectively.
- The non-textured AM surfaces tribological response was found insensitive to the variation of the process parameters or the orientation of the successive scanning layers.
- The sunk feature dimensional limitation was 150–200 µm for the SLM process with a contentious laser.
- A minimum diameter of 400 µm was evaluated to enable dimples to act as a wear debris trap.
- Higher texturing areal density reduced the specific wear rate for the dimple/groove textured surfaces due to the associated reduction in the actual contact area.
- Increased texturing feature width enabled the entrapment of the wear particles decreasing the specific wear rate and the CoF.
- The orientation of the texturing grooves relative to the sliding direction caused width and texturing areal density increase at the sliding location, further reducing the CoF and specific wear rate.
- Groove orientation induced gradual engagement and better stress distribution, enhancing the textured surface tribological response.
- X-shaped and V-shaped grooves demonstrated the best tribological response with a 60% reduction in CoF and 80% less specific wear rates.

Intending to eliminate the tensile RS challenge for the AM parts, the potential of tailoring the RS in-process was evaluated by controlling the scan track length. Then, the effectiveness of the LP as a post-processing tool to induce compressive RS in AM metallic parts was assessed. Furthermore, the impact of LP parameters to tailor RS, surface roughness, hardness, and wear resistance was investigated. As a result, the following conclusions can be established for **the second phase of this research**:

- RS showed insignificant changes with the variation of the scanning track length.
- Controlling the track length caused higher porosity and apparent warping, especially not applying orientation between successive scanning layers.
- The utilization of LP with higher power density successfully reduced the tensile RS and induced compressive RS up to 471 Mpa.
- A 40 % increase in hardness and 50% reduction of the wear volume were achieved by high power density LP.
- The spatial uniformity of the laser spot had a significant impact on the resulted surface roughness.
- The laser spot size had the highest impact on RS, hardness, and wear resistance.
- The number of peening layers demonstrated the slightest significance against all the measured responses.

- The power density was the critical control factor to induce the desired RS, *R*a, hardness, and wear resistance.
- The LP impact on the target surface was reduced by removing the ablative layer.
- A recast layer with high tensile RS occurs when performing LP without an ablative coating.
- The CA increase for the peened surfaces without an ablative layer due to its porous topography.

5.2 Future work

The present work demonstrated the notion of AT through enhancing the hydrophobicity and tribological response of the textured surfaces. The results obtained point to the significant capacity of this novel concept for tailoring AM for printing functional surfaces towards further enhancing its process capability and application potential. Other properties may be targeted in future work:

- Investigate the potential of the AT to tailor thermal properties like critical heat flux and heat transfer coefficient of the targeted surfaces.
- Explore the capacity of the AT to enhance the corrosion resistance of the textured surfaces.
- Expand the tribological behaviour study to include other lubrication regimes where AT impacts through different mechanisms.
- Examine the efficacy of AT to tailor the aerodynamic characteristics of the textured surfaces.

The LP investigation demonstrated exceptional potential to boost all the investigated properties promoting it as a viable tool to post-process AM components into functional parts. However, future studies may proceed as follows:

- Investigate the potential of using LP as a texturing technique by using wider spacing between the peening spots.
- Explore the potential of using a femtosecond laser to perform LP benefiting from the exceptionally smaller footprint.
- Assess LP with excessively higher power densities exceeding the threshold of the confinement layer.
- Expand the LP study to locally treat critical areas of interest in a functional component and evaluate the impact of the treatment on its fatigue life.